Investigation Of Electronic Transport In Topological And Correlated Materials

A thesis

Submitted For the degree of

Doctor of Philosophy (Science)

in

Physics (Experimental)

by

Rafiqul Alam

Department of Physics

University of Calcutta

2024

Dedicated to

my family

Acknowledgement

It will not be enough to express my gratitude in words to all those who helped me on this journey; I would like to extend my many, many thanks to all of them. Above all, I wish to express my sincere thanks to Atin da, whose role transcended that of a mere supervisor during my Ph.D. tenure. I am profoundly grateful for his steadfast support and invaluable direction, both of which have been essential to my journey. Moreover, I appreciate his receptiveness to discussions at any hour and his unwavering encouragement during moments of experimental setbacks.

I would like to extend my gratitude to Prof. Achintya Singha at Bose Institute for his enriching scientific discussions and for granting me the opportunity to conduct Raman spectroscopy in his laboratory. Additionally, I appreciate Prof. Priya Mahadevan at S.N.B.N.C.B.S. for her theoretical calculations and for writing the manuscript. I am very grateful to have a collaborator like Prof. Prabhat Mondal from SINP. He helped me understand the mechanisms behind the experimental observations through fruitful scientific discussions and provided guidance regarding writing the reviewers' responses. I also want to express my gratitude to Amit Agarwal sir from IIT Kanpur for his theoretical support. I also want to give my gratitude to Prasun (S.N.B.N.C.B.S.) and Debasis (IIT Kanpur) for their theoretical help.

I express my gratitude to my colleagues in the laboratory, including Biswajit, Shubhadip, Shubhrasish, Riju, Taniya, Soumili, Tausif, Buddhadeb da, Shatabda da, Shubhankar, Dhriti, Gaurab, Sujoy da, Bikash da, Obai da, Dayal, and Sayanika di, affiliated with the "Quantum Transport and Device Lab." Special thanks to all of them for maintaining a positive lab atmosphere and a conducive research environment. It was a wonderful experience to build the lab from scratch with my first four lab members: Biswajit, Shubhadip, Shubhrasish, and Riju. Working with them was fun and enjoyable, creating a special bond between us. I would like to extend a heartfelt thanks to Shubhadip Moulick for his invaluable assistance with mechanical instrument-related challenges. His expertise and willingness to offer guidance have been instrumental in navigating various technical hurdles. I am deeply grateful for his contributions. Thank you, Shubhadip, for your unwavering support and exceptional help during difficult times. I am deeply grateful to Shakti da, Amit da, Joy da, Urmi di, Dipanyan da, Debarghya da, Sourav da (Centre facility labs), and Amit da, Subabrata da (mechanical workshop) for their

invaluable technical assistance during my research at SNBNCBS. I also extend my heartfelt thanks to all the SNB staff in various departments for their support.

I would like to extend special thanks to the SNB cricket group members. I appreciate my cricket and table tennis partner, Amrit. I want to give a special thanks to the cooking team who prepared delicious meals for me. Nur, Debayan, Saniur, and Shubhadip, you are exceptional cooks, and I am grateful for the wonderful food you made. I cannot adequately express my thanks to my family, who have stood by me through every situation. I owe who I am today to their boundless love, sacrifices, care, guidance, support, and encouragement. In summary, their immense sacrifices have been essential to my achievements. My parents, brothers, sister-in-law, and niece are my strength and inspiration.

Last but not the least, I owe a debt of gratitude to the Almighty for sailing me through the journey of my life and making this possible by being with me through all the ups and downs.

Rafiqul Alam

List of publications:

List of publications related to thesis work:

1. Detection of Nontrivial Topology Driven by Charge Density Wave in a Semi-Dirac Metal

Rafiqul Alam, Prasun Boyal, Shubhankar Roy, Ratnadwip Singha, Buddhadeb Pal, Riju Pal, Prabhat Mandal, Priya Mahadevan, and Atindra Nath Pal

Adv. Funct. Mater. 2023, 2306751.

2. Signature of Commensurate charge density wave driven non-trivial electronic band in Van der Waal 1T-TaS_2.

Rafiqul Alam, Debasis Dutta, Amit Agarwal, and Atindra Nath Pal

(Manuscript ready to be submitted**)**

3.Anisotropic transport properties and high-mobility of charge carriers of antiferromagnetic $GdAgSb_2$.

Shubhankar Roy, Ratnadwip Singha, **Rafiqul Alam** and Prabhat Mandal

J. Phys.: Condens. Matter 35 (2023) 425701.

Other Publication not covered in the thesis:

1. "Sensing remote bulk defects through resistance noise in a large area graphene field effect transistor"

Shubhadip Moulick, **Rafiqul Alam** and Atindra Nath Pal

ACS Appl. Mater. Interfaces 2022, 14, 45, 51105–51112

2. "Flicker Noise in an Electrolyte Gated Large Area Gr-FET"

Rafiqul Alam, Shubhadip Moulick, Atindra Nath Pal

AIP Conf. Proc. 3067, 020003 (2024)

Abstract:

The ground-breaking discovery of topological insulators in 2005 enhances the importance of band topology in condensed matter physics, with implications extending to superconductors, semimetals, and other pivotal domains. Discoveries of topological phases in strongly correlated systems, such as heavy-fermion compounds like SmB_6 and YbB_{12}, have further fuelled interest in this area. The interplay between electron correlation and topology is particularly intriguing due to its potential to induce nontrivial properties, shaping contemporary condensed matter physics. To address the thesis objective of examining "correlation and topology," we investigated two correlated phenomena alongside topological properties: charge density waves (CDWs) and antiferromagnetic (AF) spin ordering. Initially, our focus was on $LaAgSb_2$ and 1T-TaS_2, each exhibiting unique CDW modulation characteristics. Further exploration led us to the topological square net system $GdAgSb_2$, displaying antiferromagnetic spin ordering along c-axis at very low temperatures (T=14 K).

In $LaAgSb_2$, featuring a square net crystal structure, multiple CDW transitions occur as temperature decreases. Large planar Hall (PHE) signals are found in the CDW phase, indicative of a chiral metallic phase discovered through optimization via first-principles calculations. The anisotropic nature of the Dirac cone gives the PHE signal at high temp. This study provides insights into correlation-driven topological transitions via electron transport measurements and ab-initio electronic structure calculations. In the case of 1T-TaS_2, which hosts chiral CDW, we investigated Berry curvature-driven properties. Different degrees of CDW ordering are observed depending on temperature, with the Berry curvature-driven PHE signal and Non-linear Hall effect (NLHE) appearing only inside the commensurate CDW phase. The breakdown of inversion symmetry in the commensurate CDW phase leads to persistent Berry curvature, determined through a developed model Hamiltonian based on electronic band structure.

Finally, in the investigation into magnetism and topology, we examined the antiferromagnetic topological system $GdAgSb_2$. The system exhibits significant non-saturating magnetoresistance and a positive PHE signal, reminiscent of other topological systems. Anomalies in the PHE signal and distinct exponents in its magnetic field dependence above and below the Neel temperature (T_N) were noted. Our experimental technique offers a pathway to explore the influence of magnetism on topological properties.

সারাংশ

2005 সালে টপোলজিক্যাল ইনসুলেটরগুলির গ্রাউন্ড ব্রেকিং আবিষ্কার কনডেন্সড ম্যাটার ফিজিক্সে ব্যান্ড টপোলজির গুরুত্বকে বাড়িয়ে তোলে, যার প্রভাব সুপারকন্ডাক্টর, সেমিমেটাল এবং অন্যান্য মূল ডোমেনে প্রসারিত হয়। SmB_6 এবং YbB_{12}-এর মতো ভারী-ফার্মিয়ন যৌগগুলির মতো দৃঢ়ভাবে সম্পর্কযুক্ত সিস্টেমে টপোলজিকাল পর্যায়গুলির আবিষ্কারগুলি এই ক্ষেত্রে আরও আগ্রহ বাড়িয়েছে। ইলেক্ট্রন পারস্পরিক সম্পর্ক এবং টপোলজির মধ্যে আন্তঃপ্রক্রিয়া বিশেষভাবে চমকপ্রদ কারণ এটির গুরুত্বপূর্ণ বৈশিষ্ট্যগুলিকে প্ররোচিত করার সম্ভাবনা, সমসাময়িক ঘনীভূত পদার্থের পদার্থবিদ্যাকে আকার দেয়। থিসিস-এর উদ্দেশ্য 'সম্পর্ক এবং টপোলজি' তদন্ত করার জন্য, আমরা টপোলজিকাল বৈশিষ্ট্যগুলির পাশাপাশি দুটি ইলেকট্রনিক সম্পর্ক যুক্ত ঘটনা তদন্ত করেছি: আধান-এর ঘনত্ব তরঙ্গ (CDW) এবং অ্যান্টিফেরোম্যাগনেটিক (AFM) স্পিন অর্ডারিং। প্রাথমিকভাবে, আমাদের কেন্দ্রবিন্দু ছিল $LaAgSb_2$ এবং $1T\text{-}TaS_2$, প্রতিটি অনন্য CDW মডুলেশন বৈশিষ্ট্য প্রদর্শন করে। আরও অন্বেষণ আমাদেরকে টপোলজিকাল স্কয়ার নেট সিস্টেম $GdAgSb_2$-এ নিয়ে যায়, খুব কম তাপমাত্রায় (T=14 K), C-অক্ষ বরাবর অ্যান্টিফেরোম্যাগনেটিক স্পিন ক্রম প্রদর্শন করে।

LaAgSb2-এ, একটি বর্গাকার নেট স্ফটিক কাঠামোর বৈশিষ্ট্যযুক্ত, তাপমাত্রা হ্রাসের সাথে সাথে একাধিক CDW রূপান্তর ঘটে। CDW পর্বে বড় প্ল্যানার হল (PHE) সংকেত পাওয়া যায়, যা প্রথম-নীতি গণনার মাধ্যমে অপ্টিমাইজেশনের মাধ্যমে আবিষ্কৃত একটি চিরাল(chiral) ধাতব পর্যায়ের নির্দেশক। ডিরাক শঙ্কুর অ্যানিসোট্রপিক প্রকৃতি উচ্চ তাপমাত্রায় PHE সংকেত দেয়। এই অধ্যয়নটি ইলেক্ট্রন পরিবহন পরিমাপ এবং অ্যাব-ইনটিও ইলেকট্রনিক কাঠামো গণনার মাধ্যমে পারস্পরিক সম্পর্ক-চালিত টপোলজিকাল ট্রানজিশনের অন্তর্দৃষ্টি প্রদান করে। 1T-TaS2 এর ক্ষেত্রে, যা chiral CDW হোস্ট করে, আমরা Berry curvature চালিত বৈশিষ্ট্যগুলি তদন্ত করেছি। Berry curvature -চালিত PHE সংকেত এবং নন-লিনিয়ার হল ইফেক্ট (NLHE) শুধুমাত্র কাইরাল CDW পর্বের ভিতরে উপস্থিত হওয়ার সাথে তাপমাত্রার উপর নির্ভর করে CDW অর্ডারের বিভিন্ন ডিগ্রী পরিলক্ষিত হয়। Commensurate CDW দ্বারা বিপরীত প্রতিসাম্যের ভাঙ্গন সিস্টেমে Berry curvature নিয়ে আসে, যা ইলেকট্রনিক ব্যান্ড কাঠামোর উপর ভিত্তি করে একটি মডেল হ্যামিলটোনিয়ান দ্বারা "নির্ধারণ করা হয়|

অবশেষে, চুম্বকত্ব এবং টপোলজির তদন্তে, আমরা অ্যান্টিফেরোম্যাগনেটিক টপোলজিকাল সিস্টেম $GdAgSb_2$ পরীক্ষা করেছি। সিস্টেমটি উল্লেখযোগ্য নন-স্যাচুরেটিং ম্যাগনেটোরেসিস্ট্যান্স এবং একটি ধনাত্মক PHE সংকেত প্রদর্শন করে, যা অন্যান্য টপোলজিকাল সিস্টেমের স্মরণ করিয়ে দেয়। PHE এর মানের অসামঞ্জস্য নীল তাপমাত্রা এর নিকট এবং নীল তাপমাত্রা (T_N) এর উপরে এবং নীচে এর চৌম্বক ক্ষেত্রের নির্ভরতার স্বতন্ত্র সূচকগুলি উল্লেখ করা হয়েছিল। আমাদের প্রয়োগশীল পদ্ধতি টপোলজিকাল বৈশিষ্ট্যগুলির উপর চুম্বকত্বের প্রভাব তদন্ত করার একটি পথ উপস্থাপন করে।

Contents:

Chapter 1

Introduction:

Solid materials with ordered atomic structures, known as crystalline states, are fundamental in modern technology. These materials, such as ferromagnetic substances used in electric devices and semiconductors driving computational advancements, underpin various technological applications. Condensed matter physics extensively investigates these systems, particularly focusing on electronic states and their correlations, which give rise to phenomena like superconductivity and charge density waves.

In simpler scenarios where electron interactions are weak, a system can be described by the influence of an average periodic potential. This leads to independent wave-like states, each either occupied or unoccupied depending on energy levels, yielding complex phenomena. The integer quantum Hall effect (QHE), observed in 1980[1], exemplifies this complexity, where strong magnetic fields induce chiral edge states, showcasing topological aspects. Topological matter explores electronic states's topological structure, revealing deep connections between bulk properties and conducting edge states. Additionally, crystalline systems exhibit low-energy excitations akin to elementary particles, like electron vacancies termed quasiparticles. Describing solids in terms of quasiparticles often simplifies understanding, especially in conjunction with topological considerations in materials like topological semimetals

Topology, a comprehensive concept with applications extending beyond condensed matter physics, involves the examination of enduring spatial characteristics amidst continuous transformations. In the context of condensed matter physics, this spatial domain is commonly identified as the reciprocal k-space, elucidated by a (topological) band theory[2–5].

In **Section 1.1**, We commence by providing a concise overview of illustrative instances demonstrating topological concepts in everyday situations. **Section 1.2** Wraps up by summarizing the domains in physics where topology holds significance, elucidating its presence in condensed matter physics.

1.1 Examples of topology from Everyday Life:

The objective of this section is to provide an intuitive grasp of topological classification without necessitating mathematical expertise. The guiding principle is as follows: If two entities can

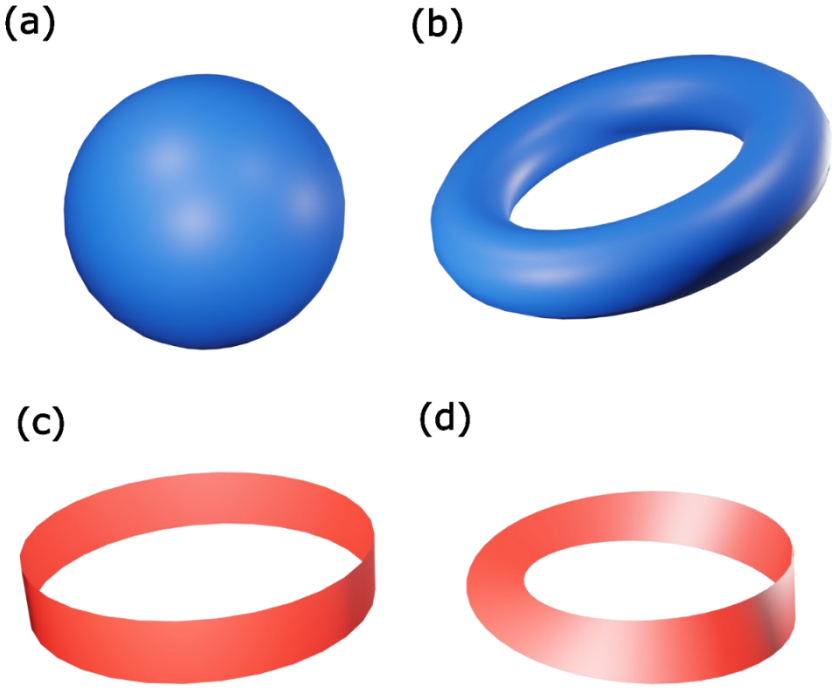

Figure 1.1 (a) *Sphere* ***(b)*** *Doughnut or Torus* ***(c)*** *Annulus strip* ***(d)*** *Mobius strip*

undergo a smooth transformation into each other, they are deemed topologically equivalent. While this assertion may initially seem somewhat vague, it is unequivocal that actions such as cutting and glueing do not qualify as smooth transformations. In the process of a smooth deformation, an object's defining characteristics remain unchanged, rendering it an equivalent entity. Typically, an invariant, persisting unchanged throughout the transformation, serves to characterize such a resilient attribute.

1.1.1 Sphere and Torus:

Initially, take a small quantity of modelling clay and mould it into a sphere, as illustrated in **Figure 1.1a** Subsequently, the sphere can be smoothly transformed into a disk or a bowl. However, to achieve a doughnut resembling the one depicted in **Figure 1.1b**, the introduction of a hole is necessary. Creating a hole involves puncturing through the middle of the sphere, a type of deformation not considered smooth. Consequently, an object's hole count serves as an invariant, remaining constant through smooth deformations. In mathematics, the genus "g" is

defined as the number of holes and is associated with the Euler characteristic. It can be computed using the Gauss-Bonnet theorem for surfaces without boundaries[6].

$$g=1-\frac{1}{2}\frac{1}{2\pi}\int_S dA \qquad \ldots\ldots 1.1$$

over the Gaussian curvature K, as an integral.

1.1.2 Annulus and Möbius Strip:

Let's contemplate a simple analogy: the act of attaching the ends of a paper strip. Post-adhesion, the resulting arrangement should mirror the illustrated entities in **Figure 1.1c, and d**. An intrinsic property in this scenario is the count of twists embedded in the strip, underscoring the fact that this distinctive feature remains unalterable unless the strip is cut afresh. Smooth deformations possess the capacity to redistribute the twists along the loop but are incapable of modifying their numerical count.

1.2 Physics Overview of topology:

The categorization of matter according to its organized phases constitutes a significant and impactful paradigm in condensed matter physics. The breaking of local, spontaneous symmetries is a defining characteristic of certain phases within this framework. The exploration of topology in condensed matter physics has garnered notable attention in recent times. Our goal is to provide a brief overview of the motivations for investigating the topological properties of a system, the primary effects that can be observed, and the factors restricting these effects to systems composed of condensed matter[7]. This chapter is based upon the Ref [7]

In such scenarios, a local order parameter is defined, exhibiting a zero value outside of the ordered phase and a finite value within it. A well-known example is the finite magnetization in the ferromagnetic phase. To analyse the transition, one can employ the Landau theory of phase transitions, expanding the order parameter, which is expected to be small around the transition point[8,9]. Various types of phase transitions are then characterized by different orders in the parameter. In contrast, other phases do not involve broken symmetries, adding subtlety to their nature. For instance, consider the IQH effect[10], where the quantized conductance remains unaffected by both smooth and local fluctuations in material parameters.

The conductivity can only be modified by closing the gap. A compelling feature of topological effects, making them attractive for applications in physics, is their robustness. As topology is an attribute of the underlying space of wave functions, it offers a universal characterization of

systems. This resilience distinguishes topological effects from microscopic theories, which depend on an array of material parameters.

As expounded in Section 2.2, the realm of topological band theory emerges as a potent instrument for the categorization of crystals. Within each band resides a geometric phase, the Berry phase[11], harbouring latent topological information. This implies that the essence of a crystal's topology is intricately woven into its eigenstates rather than solely manifesting in its energy spectrum. The Berry phase encapsulates invariants like Z_2 and Chern numbers, symbolized as integrals, thereby facilitating the classification of insulators based on preserved symmetries. The benchmark in this context is the trivial insulator, characterized as an insulator that seamlessly transitions into the atomic limit under the gradual cessation of hopping. Topological effects exhibit resilience against localized disturbances, endowing them with significance for experimental exploration. Two notable practical applications of topology include error-protected quantum computing, reliant on nonlocal qubits, and the establishment of a unit system grounded in a perfectly quantized conductance. Although the majority of topological insulators (TIs) maintain insulating properties, their significance lies in the presence of gapless surface states, rendering them compelling subjects for further scrutiny. A noteworthy and experimentally verified instance exemplifying the existence of edge states is the Quantum Hall effect (IQH effect)[1,12]. In a strong magnetic field, a two-dimensional electron gas (2DEG) generates Landau Levels (LLs) with quantized energies given by $(n + 1/2)\ \hbar\omega_c$, $\omega_c = eB/m$ where 'm' represents the particle mass. The edge conductance is directly proportional to the number of LLs or the filling factor at the edge, where the local potential guides the LLs past the Fermi energy. Similarly, the Quantum Spin Hall (QSH) effect, as discussed in Section 1.2.1.2, can be comprehended. In this scenario, the system features robust spin-orbit coupling (SOC) instead of a magnetic field. One potential outcome of this setup is the emergence of a finite spin Hall conductance.

1.2.1 Band Theory:

Our focus now turns to the topological classification of matter, aligning with the concept discussed in Section 2.1.3 which involves classifying matter based on its phase. This undertaking poses a significant challenge. To simplify this classification, this section narrows its scope to matter describable by band theory. In the context of a band insulator, the ground state is represented by a Slater determinant, and its description relies on the independent electron approximation. If the Hamiltonians of two insulators can be interchanged while the system remains in the ground state, these insulators are deemed topologically equivalent. Given

that an insulator possesses a band gap, changes can be made gradually enough to avoid exciting the system, a process known as adiabatic. Topological transitions during this transformation necessitate a band closing. Within the constraints of band theory, this constitutes the sole method for altering a system's topological characteristics. Furthermore, the presence of a band gap ensures that weak interaction effects do not alter the topological classification. Consequently, the topology of interacting states and noninteracting electrons that can be adiabatically connected remains the same. In the subsequent discussion, we initiate with a concise overview of band theory. The utilization of the Berry phase is introduced in Section 1.2.1.1 to elucidate topological aspects. As detailed in Section 1.2.1.2, the presence of time-reversal (T) symmetry reinforces the topological classification. The emergence of gapless edge states at the boundaries of topological systems directly stems from a topological change at interfaces.

1.2.1.1 Bloch theory:

We expeditiously revisit the Bloch theorem, serving as the cornerstone of band theory. The initial assumption is made that the physical material under examination is both crystalline and functionally noninteracting. This assumption, grounded in translational symmetry, allows for the labelling of single-particle states by crystal momentum 'k'.

$$|\psi_{n,k}(r) \geq e^{i\mathrm{k}\cdot\mathrm{r}}|u_{n,k}(r) > \qquad \ldots\ldots.1.2$$

$|u_{n,k}(r) >$ is Bloch Hamiltonian H (k) = $e^{-i\mathrm{k}\cdot\mathrm{r}} H$ (r) $e^{i\mathrm{k}\cdot\mathrm{r}}$,

$$H\,(\mathrm{k})\ |u_{n,k}(r) > = E_{n,k}\ |u_{n,k}(r) >. \ldots\ldots\ldots.1.3$$

The band structure is characterized by the eigenvalues $E_{n,k}$ and the corresponding eigenvector $|u_{n,k}(r) >$. Occupancy of these bands progresses from the lowest energy levels upward, guided by the Pauli exclusion principle, which stipulates that each state can only be occupied once. In the context of insulators, a discernible energy gap at the Fermi energy separates the lowest unoccupied band, identified as the conduction band, from the highest occupied band, recognized as the valence band.

Considering the reciprocal lattice vector G, translational symmetry implies H (k + G) = H (k). Within the periodic Brillouin Zone (BZ), crystal momentum is defined modulo translations by a multiple of G. This equivalence corresponds to the topology of a torus T_d in d dimensions. The band structure can be comprehended as a mapping between the space of Bloch Hamiltonians with an energy gap and the toroidal space of the Brillouin Zone.

In practical terms, obtaining the band structure of a crystal is achieved through tight-binding calculations, which offer a powerful and effective method.

Within a lattice, electrons are predominantly localized around individual atoms. Their ability to transition from one atom to the next arises due to the overlap of outer electron orbits. Utilizing delocalized bands allows for the description of overlapping orbitals. Often, the focus is on the physics near a specific point in the Brillouin Zone (BZ). In such cases, employing the k·p theory becomes meaningful to derive an effective continuum model through an expansion in k-space. If the band structure exhibits a gap, rendering it effectively inert across the rest of the Brillouin Zone (BZ), these continuum models aptly encapsulate the essential low-energy physics.

We can now pinpoint the juncture where topological considerations become relevant in band theory. This is achieved by closely scrutinizing the phase factors acquired by an electron in a Bloch band during its time evolution. We introduce the concept of the Berry phase and discuss its quantization through Chern invariants. In quantum mechanics, a wave function is defined up to a phase, such that the substitution

$$|u_{n,k}(r)> \rightarrow e^{i\varphi(k)}|u_{n,k}(r)> \qquad \text{.....1.4}$$

the eigen-energies remain invariant with the phase $\sim\varphi(k)$. As a result, the eigen-energies are independent of the gauge, in accordance with the expectation for observables.

Let's analyze the temporal evolution of the system. Consider a Hamiltonian dependent on a single parameter, denoted as R(t), which undergoes a slow cyclic evolution from t = 0 to t = T, where R (0) = R(T), and T represents the period. This evolution traces a closed path C in parameter space. The definition of the instantaneous eigenstate basis of H (R(t)) is then given by:

$$H(\mathrm{R}(t))\,|u_n(\mathrm{R}(t))> = E_n\,(\mathrm{R}(t))|u_n(\mathrm{R}(t))> \qquad \text{.....1.5}$$

The phase of the eigenstate may be contingent on R(t) and is not predetermined at this point. Throughout the path, the phase function is expected to be single-valued and smooth. If achieving global feasibility proves challenging, it becomes necessary to define the phase function across multiple overlapping patches.

The complete temporal evolution of the quantum state is determined by

$$i\hbar\partial_t|\psi(t) \geq H\big(\mathrm{R}(t)\big)|\psi(t)> \qquad \text{.....1.6}$$

The system remains in the instantaneous eigenstate in the adiabatic limit. Consequently, eigenstate and quantum state can be related by

$$|\psi(t) \geq e^{i\gamma_c(\mathrm{t})}\exp(-\frac{i}{\hbar}\int_0^t dt' E_n(R(t'))) \, |u_n(\mathrm{R}(t)) > \quad \ldots\ldots 1.7$$

where the Berry phase, or geometric phase $\gamma_c(\mathrm{t})$, is defined by

$$\partial_t \gamma_c(\mathrm{t}) = \; i < u_n(t) \partial_t | u_n(t) > \quad \ldots\ldots 1.8$$

It stems from the fact that the instantaneous eigen-basis and the eigenenergies both alter during time evolution. This can be rewritten as a k-space path integral such that

$$\gamma_c = \oint \boldsymbol{A_n}.\boldsymbol{dk} = \oiint \boldsymbol{\mathcal{F}_n}.\, \mathrm{d}\boldsymbol{S} \quad \ldots\ldots 1.9$$

A_n represents the vector potential which is known as Berry connection.

$$A_n = i < u_{n,k} | \Delta_k | u_{n,k} >. \quad \ldots\ldots\ldots 1.10$$

the surface $\boldsymbol{S}$ and $\mathcal{F}_n$=$\Delta_k \times A_n$ represents the Berry curvature

Though A_n undergoes alterations by gauge transformation, the Berry phase remains a gauge invariant quantity, formally equivalent to a magnetic flux.

$$i < u_{n,k} | \Delta_k | u_{n,k} >. \quad \ldots\ldots\ldots 1.11$$

The Berry curvature is analogous to the magnetic field and it can be expressed in gauge-invariant form

$$\mathcal{F}_n = i \sum_{m \neq n} \frac{<u_{n,k}|\Delta_k H(k)|u_{m,k}> \times <u_{m,k}|\Delta_k H(k)|u_{n,k}>}{(E_n - E_m)^2} \quad \ldots\ldots\ldots 1.12$$

For degenerate bands, as per Eq. (1.12), the denominator approaches zero, implying the presence of a monopole in the Berry curvature. The physical effects of the Berry phase depend on the dimensions and whether the system is an insulator or a metal. The Berry phase, particularly relevant to insulators in 1D and the Fermi surfaces of 2D metals, can be mathematically expressed as an integral over a closed curve.

1.2.1.2 Topology in Bloch state:

The topological invariant "Chern number" is defined as the integration of the Berry curvature over the entire Brillouin zone.

$$C_n = \frac{1}{2\pi} \int d^2 k \mathcal{F}_n \quad \ldots\ldots 1.13$$

So, to apprehend the topological aspect of the electronic band, one must witness the phenomenon propelled by the Berry curvature. The Chern number is mainly associated with topological invariant under broken time reversal symmetry (TRS).

Given that the Hall conductivity (and consequently the Chern invariant) displays an asymmetrical response to time reversal, the presence of topologically significant states detailed in the earlier discourse arises solely through the disruption of time reversal symmetry. This

disruption can manifest via external magnetic fields or through the imposition of magnetic order. Nonetheless, the spin-orbit interaction introduces an alternative topological category of insulating band arrangements even in the absence of time-reversal symmetry breaking. In topological materials, certain electronic properties are determined by the global topology of the material's bulk electronic structure. These topological features can manifest as robust surface states or edge states, which are protected against local perturbations. The bulk-boundary correspondence principle states that there is a direct relationship between the topological properties of the bulk and the existence and characteristics of these boundary states.

For example, in a topological insulator, the bulk of the material behaves as an insulator, while its surface hosts metallic states that are topologically protected. These surface states arise due to the nontrivial topology of the bulk electronic band structure. Similarly, in a topological semimetal, the bulk may have band crossings known as Dirac points or Weyl points, leading to exotic surface Fermi arcs or other boundary states. Understanding the bulk-boundary correspondence is crucial for characterizing and harnessing the unique electronic properties of topological materials. It provides insights into how bulk topology dictates the behaviour of surface or boundary states, which is essential for designing novel devices and exploiting topological effects in various applications, such as spintronics, quantum computing, and energy-efficient electronics.

Quantum Hall Effect:

Initially, energy bands possessing a nonzero Chern number were identified in Landau levels resulting from the quantization of a two-dimensional electronic gas influenced by a magnetic

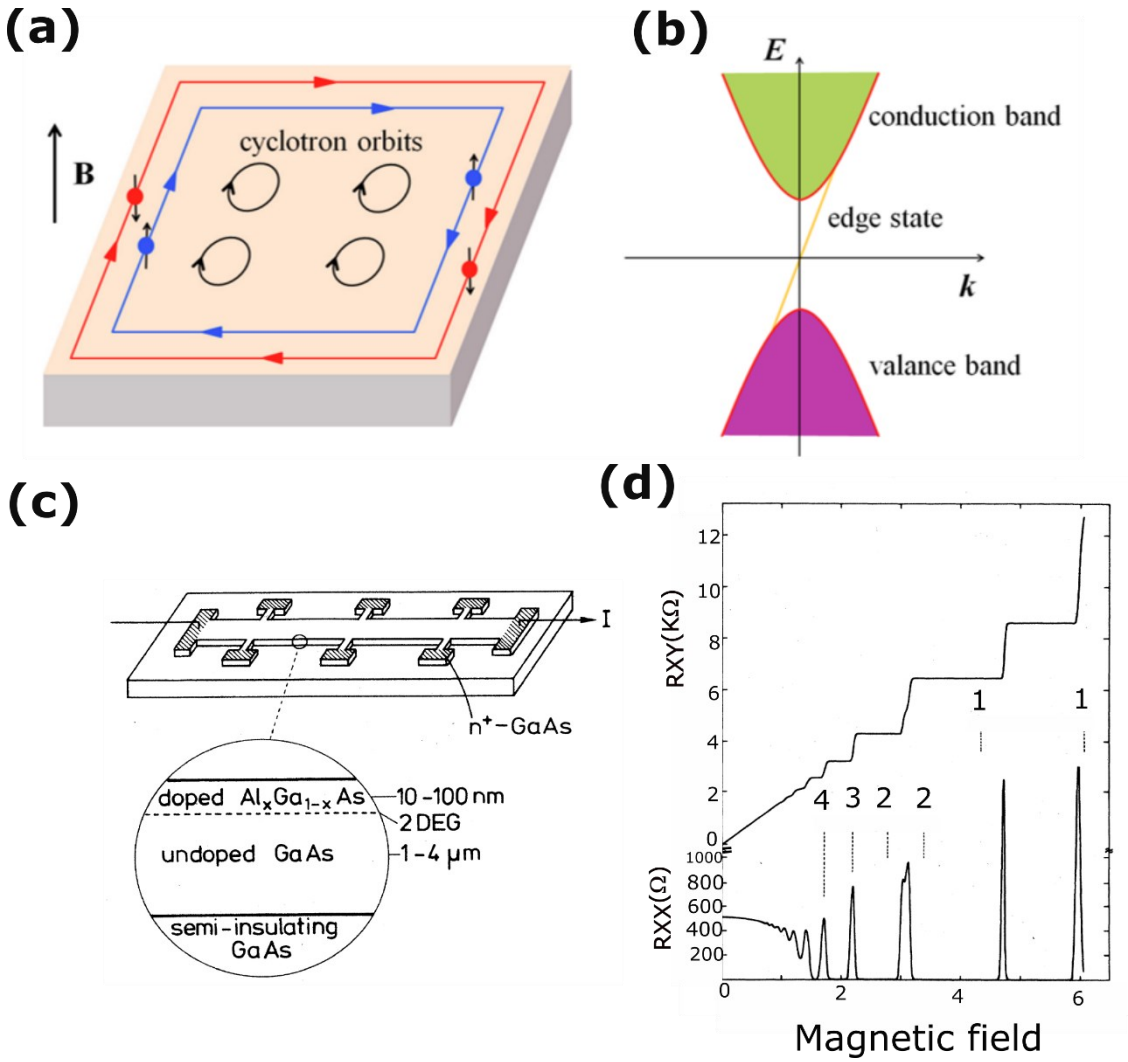

Figure 1.2 (a) *The schematic diagram of QHE with showing the mechanism of edge current* ***(b)*** *The schematic band structure of QHE system. .(adapted from Ref [10])* ***(c)*** *The illustration of the device configuration of 2DEG.* ***(d)*** *Resistance and Hall resistance is plotted against magnetic field with demonstration of the plateau as a function of magnetic field.(adapted from Ref [1])*

field perpendicular to the plane (see the ***Figure 1.2a***). Each Landau level is characterized by a Chern number. Consequently, a two-dimensional electron system subject to Landau quantization, with ν filled Landau levels, exhibits a quantized Hall conductance of $\nu e^2/h$[12]. This quantization represents the integer Quantum Hall Effect (QHE), first observed by von Klitzing in 1980[1]. He got Nobel prize in 1985 for discovering this phenomenon. Here ν is equal to the Chern number. The Chern number, denoted as C_n, serves as a topological invariant, signifying

its constancy despite smooth variations in the Hamiltonian. This consistency helps explain the stable measurement of σ_{xy} and counts the chiral edge states . It is crucial to emphasize that the topological numbers mentioned earlier are exclusively dependent on the characteristics of bulk states. In contrast, the quantum Hall effect is observable as a boundary state of a material. This distinctive attribute represents a defining aspect of topological materials, wherein the conductive behaviour at the boundary is dictated by the bulk properties—an occurrence recognized as the bulk-boundary correspondence phenomenon[13]. The bulk gap state along with conductive edge state is shown the ***Figure 1.2b.*** In **Figure 1.2c, d**, the first experimental observation of vanishing longitudinal resistance and quantized Hall resistance versus magnetic field is presented with the schematic of the device structure.

Quantum spin Hall Effect (*QSHE)*:

Over the recent years, theoretical scientists have suggested that electrical current might flow along the edges without a magnetic field. Their projections anticipate the emergence of edge

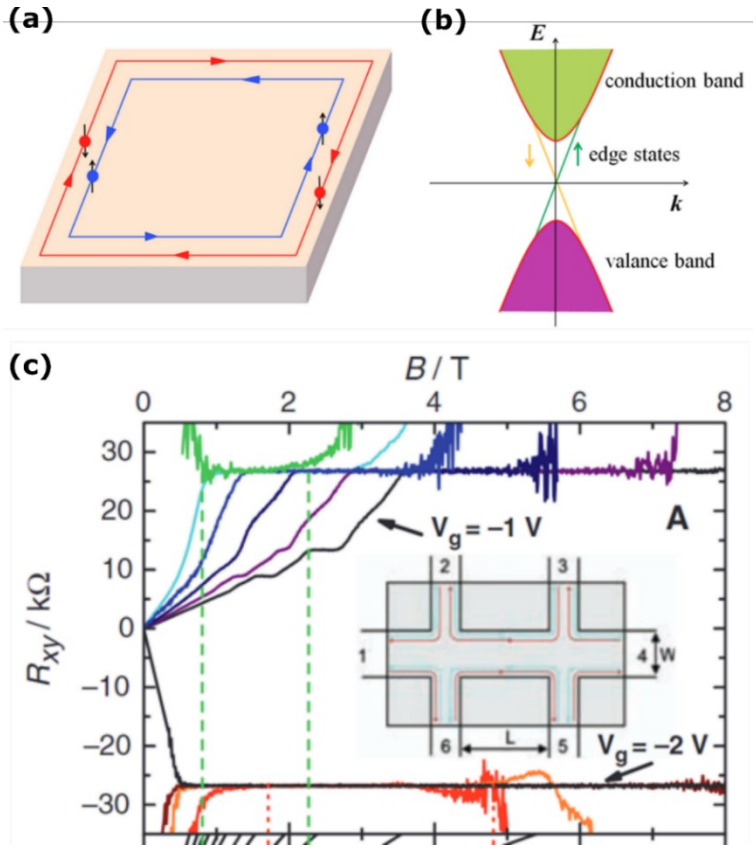

Figure 1.3 (a) *The schematic representation of the edge current due to QSHE* ***(b)*** *Band structure of QSHE system (adapted from Ref [10])* ***(c)*** *First experimental evidence of QSHE in* (HgTe/(Hg,Cd)Te) QW *as a function of magnetic field at different gate voltages (adapted from Ref [15]) with inset showing schematic of the device. structure.*

states in insulators possessing appropriate electronic configurations. Notably [2,3,14] distinct from the quantum Hall effect, these edge states are expected to exhibit a peculiar behaviour: carriers with opposing spins traversing in opposite directions along a specific edge, as illustrated in the accompanying diagram ***Figure 1.3a and b***. This phenomenon is called the quantum spin Hall effect, and researchers have eagerly tried to prove it through experiments.

Despite the abundance of insulators in the natural world, the majority lack the requisite structural characteristics for the potential manifestation of the quantum spin Hall effect. The distinctive electronic configuration of HgTe becomes crucial in this context. While bulk HgTe functions as an II-VI semiconductor, its electronic structure deviates from the norm. Typically, in analogous materials, the conduction band originates from s-states situated on the group II atoms, and the valence band arises from p-states at the VI atoms. However, in HgTe, this sequence undergoes an inversion below certain thickness. The signature of QSHE was discovered in (HgTe/(Hg,Cd)Te) QW [15] in 2007. The experimental result is shown in **Figure 1.3c** with the schematic of the device. The plot shows magnetic field dependent Hall resistance at different gate voltages.

Quantum anomalous Hall effect (*QAHE*):

The identification of the quantum spin Hall phenomenon has notably progressed the investigation into the quantum anomalous Hall phenomenon. Through the induction of

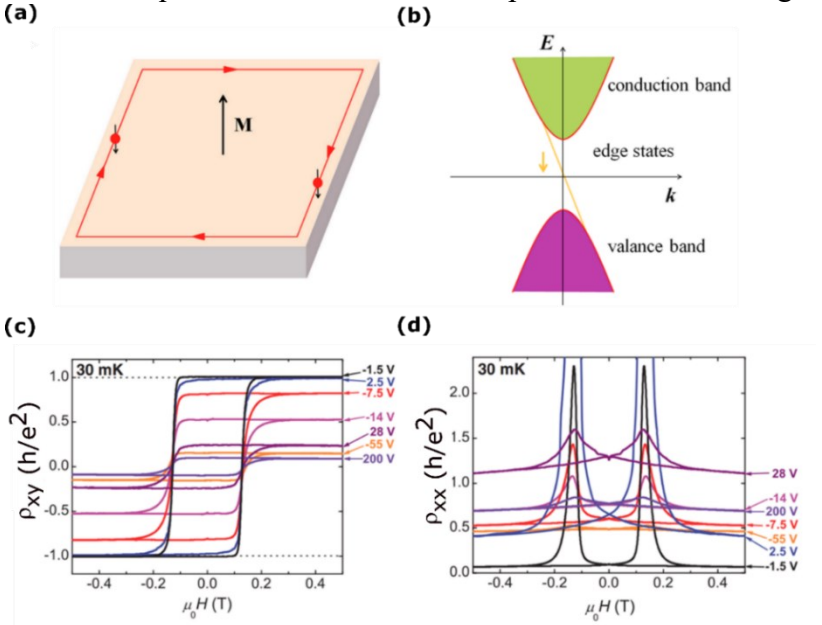

Figure 1.4 (a) *The schematic illustration of the edge current due to QAHE* ***(b)*** *Band structure of QAHE system (adapted from Ref [10])* ***(c)*** *First experimental evidence of QAHE showing the hysteresis loop at T =30 mK. at different gate voltages* ***(d)*** *The plot of resistance vs. magnetic field data at different gate voltages (adapted from Ref[16])).*

ferromagnetism and the disruption of time-reversal symmetry, a particular spin pathway in the quantum spin Hall configuration is inhibited as describe in **Figure 1.4a, and b**, consequently leading to the emergence of the quantum anomalous Hall phenomenon. After sustained dedication and hard work, Xue's group achieved the ground-breaking experimental observation of the quantum anomalous Hall effect without the necessity for an external magnetic field in the magnetically doped thin film of $Cr_{0.15}(Bi_{0.1}Sb_{0.9})_{1.85}Te_3$[16]. The **Figure 1.4c, and d** show that the Hall conductance becomes quantized when the longitudinal conductance is zero.

The quantization of Hall conductance serves as a notable outcome in this endeavour. The central idea of non-trivial phases of matter is based upon the fact whether[16] the system poses non-vanishing Berry curvature or not in k-space. In this direction mainly two types of bulk material can consider. Weyl semimetal and massive gapped Dirac semimetal are condensed matter systems whose electronic transport properties are dictated by the Berry curvature.

3D topological insulator:

Commencing from the quantum spin Hall insulator in two dimensions, scientists have investigated extending this idea to three-dimensional topological insulators featuring conductive surface states. Experimental validation has successfully confirmed the theoretical prediction. The surface states of these three-dimensional topological insulators share akin traits with the electronic structures of graphene, manifesting a relativistic linear relationship between energy and momentum[2,3,5,14]. Nevertheless, in contrast to graphene, these three-dimensional topological insulators are characterized by a solitary Dirac cone, devoid of any resemblance. To establish a three-dimensional topological insulator, a robust spin-orbit coupling (SOC) plays a pivotal role in substantially shaping the electronic configuration. Consequently, semiconductors incorporating hefty elements and narrow band gaps emerge as auspicious contenders, given the pronounced SOC impact in such heavy elements. To ensure the effectiveness of the spin-orbit coupling, the band gap must remain smaller than the energy scale of SOC, thereby guaranteeing the occurrence of the transition to a topological insulator[5].

The initial identification of a three-dimensional topological insulator pertai16ns to the Bi_xSb_{1-x} alloy[17]. Subsequent discoveries encompass the Bi_2Se_3 family, comprising Bi_2Te_3 and Sb_2Te_3[18,19]. In contrast to the Bi_xSb_{1-x} alloy, the Bi_2Se_3 variants prove comparatively straightforward in their preparation. They demonstrate topological insulator properties even

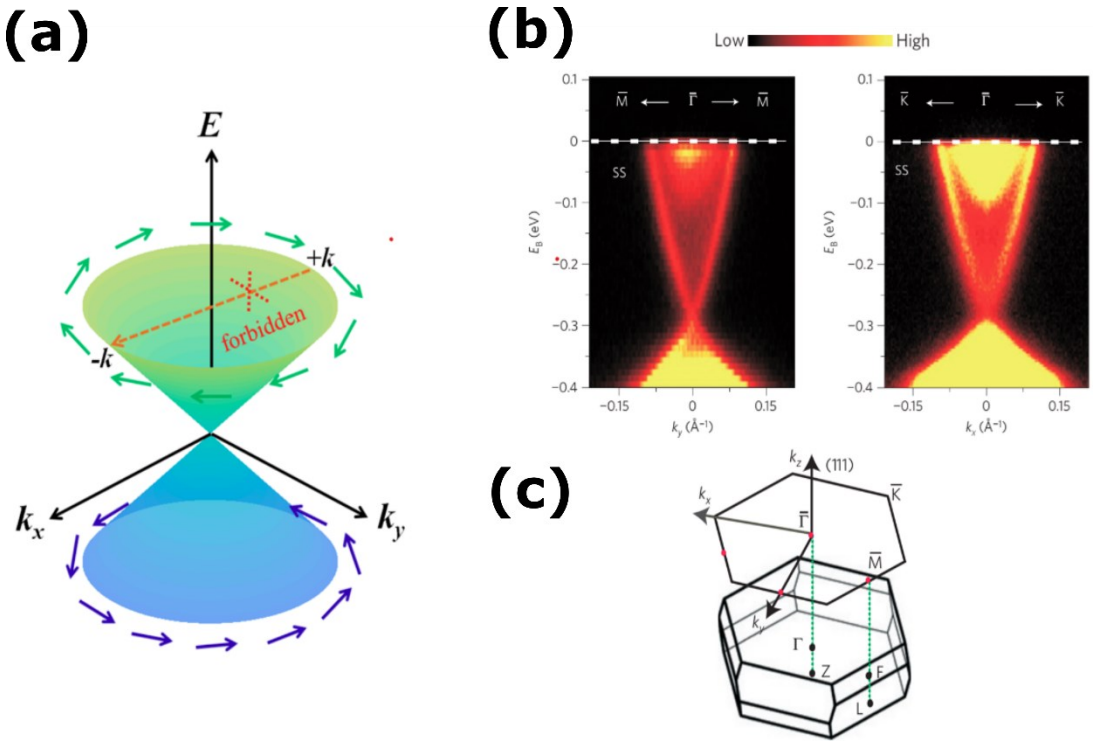

Figure 1.5 (a) *The helical-shaped Dirac cone surface features of three-dimensional topological insulators. The green and blue arrows are used to show the spin texture of Dirac electrons (adapted from Ref [12]).* ***(b)*** *The electronic structure of the topological insulator Bi_2Se_3. it displays the dispersion of the (111) surface measured via angle-resolved photoelectron spectroscopy (ARPES).* ***(c)*** *The corresponding Brillouin-zone is demonstrated (adapted from Ref [21]).*

under elevated temperatures. Consequently, Bi_2Se_3 emerges as a promising candidate for room-temperature applications in low-loss spintronic devices[20].

Dirac semimetal:

In 2004, Novoselov et al. achieved a ground-breaking milestone through the successful mechanical exfoliation to obtain monolayer graphene[21]. Graphene, a prominent example of a Dirac semimetal, manifests Dirac fermions at the K and K' points in its Brillouin zone, leading band gap surpassing 0.1 eV. Noteworthy is the Bi_2Se_3's band gap[22], approximately 0.3 eV (equivalent to 3600 K), markedly exceeding the energy scale at room temperature.

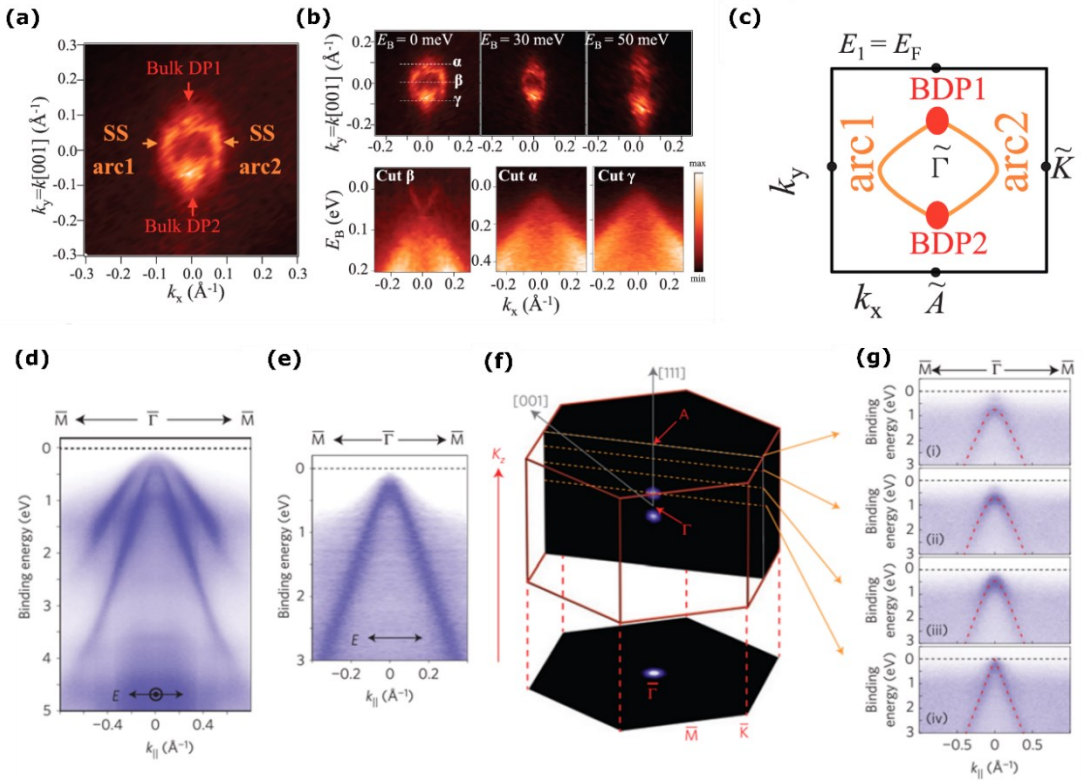

Figure 1.6: **ARPES studies of Na_3Bi:** ***(a)*** *The mapping of Fermi surface taken at a photon energy of* ***55*** *eV, is shown . BDP1 and BDP2 describe the Dirac points.* ***(b)*** *With a fixed photon energy of 55 eV, the constant energy contours are presented at three binding energy. The dispersion at the three cut is also shown below.* ***(c)*** *Schematically bulk Dirac point along with Fermi arc is depicted.(adapted from Ref[25])*

ARPES studies of Cd_3As_2: ***(d)*** *Band dispersion of Cd_3As_2 covering a large energy and momentum scale along the $\bar{M} - \bar{\Gamma} - \bar{M}$ direction measured by photons with mixed polarization (inset, with both components perpendicular and parallel to the $\bar{\Gamma} - \bar{M}$ direction)* ***(e)*** *Band dispersion measured with photon polarization parallel to the $\bar{\Gamma} - \bar{M}(inset)$* ***(f)*** *Visualization of the Fermi surface extends across the entirety of the 3D Brillouin zone in the upper panel, while its projection onto the surface Brillouin zone is depicted in the lower panel, specifically within the k_z–k_y plane. Notable high-symmetry points within the Brillouin zone are denoted in the plot, with directional indicators provided by grey arrows representing the [001] and [111] directions.* ***(g)*** *It demonstrating how the band evolve from parabolic dispersion to linear {from (i) to (iv)}..(adapted from Ref[28])*

Recently, graphene has garnered renewed attention owing to its exceptional physical attributes, encompassing superlattice structures and superconductivity in the realm of magic angle graphene[23,24]. Na_3Bi stands out as a noteworthy instance of a three-dimensional topological

Dirac semimetal, initially theorized[25] and subsequently validated through experimental investigations[26,27].

Characterized by time reversal and threefold rotational symmetry, Na_3Bi features two Dirac points along the Γ–A direction. Employing techniques like ARPES, experimental observations have unveiled the existence of Dirac cones and Fermi arcs connecting bulk Dirac points, as illustrated in the ***Figure 1.6a, b***. Fermi arcs are also depicted in ***Figure 1.6c.*** Transport measurements have further demonstrated intriguing phenomena, including negative magnetoresistance attributed to chiral anomalies and quantum oscillations. However, Na_3Bi's susceptibility to instability and sensitivity to air have presented challenges for deeper investigations. Another prominent three-dimensional Dirac semimetal, Cd_3As_2, is safeguarded by time reversal and fourfold rotational symmetry, with Dirac points situated along the Γ–A direction, as confirmed by ARPES experiments[28](**see *Figure 1.6d-g for experimental results***). Additionally, Cd_3As_2 has exhibited other captivating phenomena, such as quantum oscillations and negative magnetoresistance stemming from chiral anomalies[29]. Significantly, in 2017[30], the observation of a three-dimensional quantum Hall effect in Cd_3As_2 nanosheets marked a noteworthy advancement, expanding the exploration of the quantum Hall effect beyond two-dimensional systems.

Weyl Semimetals:

"Mathematization may indeed be considered a creative endeavour of humanity, akin to language or music," asserted Hermann Weyl, the German physicist renowned for his inclination toward mathematical elegance. This inclination led him to predict the emergence of a novel particle when the fermionic mass in the Dirac equation[31] reached nullity. Such a particle could bear electric charge but, in contrast to all known fermions, would lack mass[32]. Throughout his career, Weyl gradually distanced himself from this prediction, primarily due to its implication of breaking a specific symmetry known as parity, which was believed to be upheld at the time. Moreover, the anticipated particle remained elusive throughout his lifetime. Posthumously, the Weyl fermion found relevance in describing neutrinos, ultimately revealed to possess mass. For a considerable duration, the Weyl fermion seemed destined to remain a theoretical construct from the mind of a brilliant thinker. However, this perception changed when the Weyl fermion entered the domain of condensed matter physics.

[28][29][30]In three dimensions, the Weyl node [32] is the linear intersection of two bands. The Hamiltonian that can be used to describe Weyl Fermion is as follows:

$$H(k) = \pm \sum_i k_i \sigma_i \quad \text{.....1.14}$$

Where σ_i represents the Pauli spin matrices and the plus or minus sign signifies the chirality of the Weyl Fermion. Linear cones emerge when two bands intersect at a Weyl node. The Weyl node with positive chirality serves as the source for Berry curvature, while the one with negative chirality functions as the sink for Berry curvature, akin to a topological charge. Weyl nodes exhibit resilience to minor system perturbations, and they can only be created or annihilated in pairs of opposite chirality.

The topological charge of Weyl nodes serves as a discernible identifier, and a topological invariant can be employed for their characterization. Analogous to Gauss' law for electric charge, the total flux of Berry curvature passing through a closed surface is directly proportional to the enclosed topological charge. In simpler terms, the chirality of a Weyl node determines the sign of its associated Chern number. To maintain a total topological charge of zero, the cumulative Chern numbers for all Weyl nodes in a system must mutually cancel out, as these nodes consistently occur in oppositely chiral pairs[33].

Symmetries play a role in determining the quantity and location of Weyl nodes. In the presence of inversion symmetry (I), Weyl nodes with opposite chirality are constrained to exist at the same energy but with positive topological charge at momentum k and negative topological charge at momentum -k. Additionally, if the system upholds time reversal symmetry (T), a Weyl point at k is mapped onto the Weyl point at -k with the same chiral charge under the influence of T. However, if a material system does not violet the I*T symmetry, a Weyl node undergoes a transformative mapping, returning to itself, yet embracing an altered essence in the form of an opposing chirality. Therefore, the existence of Weyl nodes is precluded in systems that adhere to the combination of parity (I) and time-reversal (T). The topological node formed by the combination of these superimposed Weyl nodes, each bearing an opposite chirality, is denoted as a Dirac node.

As the annihilation of Weyl nodes exclusively occurs in paired configurations, and the adjacent vacuum lacks Weyl nodes, there necessitates a state on the surface establishing a connection between Weyl nodes characterized by opposing chirality. This distinctive surface state is identified as a Fermi arc[34,35]. Similarly, in the presence of a magnetic field along any given direction, the interconnection of two Weyl nodes exhibiting opposite chirality is facilitated through a chiral Landau level [36]. This phenomenon, known as chiral anomaly, contributes adversely to the magnetoresistance observed in Weyl semimetals.

One can divide the Weyl semimetal into three categories

- **Type I –** Here, the Weyl point serves as the central point around which the Fermi surface is concentrated.
- **Tilted Type I-** In this case, the type-I Weyl cone undergoes a tilt in an arbitrary direction, the center of the Fermi surface is moved from the Weyl point.
- **Type II-** In these materials, both electron and hole pockets are present at the Fermi level[37,38].

Experimental signature of topological semimetal:

Fermi arc:

Another significant characteristic of the Weyl semimetal phase under investigation is its distinctive surface states, which bear resemblance to those found in topological insulators. In contrast to the bulk Fermi surface, which is limited to a specific set of momentum points, surface states can be established for almost every surface momentum. These surface states

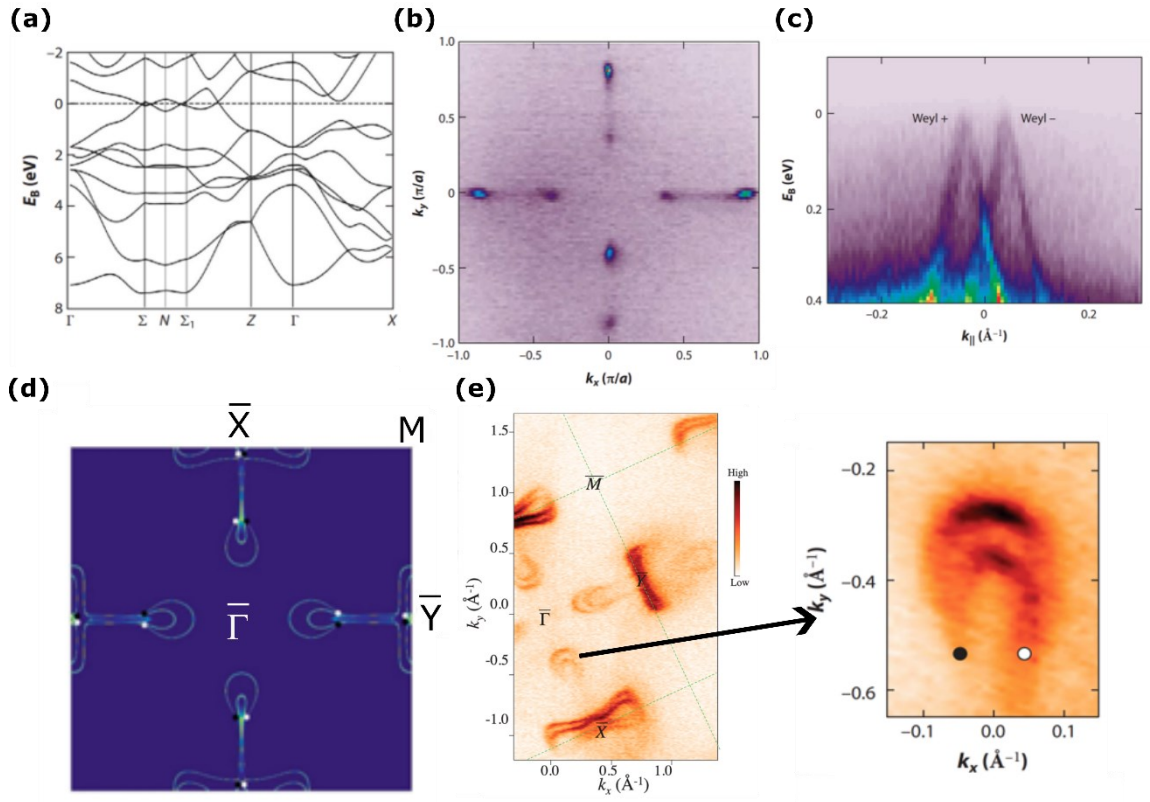

Figure 1.7 (a) *Theoretically calculated band structure of TaAs* ***(b)*** *ARPES measured k_x–k_y Fermi surface maps at the k_z value that corresponds to the Weyl nodes* ***(c)*** *ARPES data showing energy vs. momentum dispersion with displaying the Weyl cones with linear dispersion and ± chirality. (d) The Fermi arc is shown based on the theoretical calculation. (e) The experimentally observed surface state with showing the Fermi arc using the black arrow (adapted from Ref [38,39]).*

manifest as intriguing geometric formations known as "Fermi arcs" within the surface Brillouin zone. Notably, these arcs extend between the Weyl points, delineating a unique and intricate pattern that reflects the peculiar topological nature of the Weyl semimetal phase. This phenomenon underscores the rich and unconventional behavior exhibited by the surface states in Weyl semimetals, contributing to the unique properties and potential applications of this intriguing quantum state of matter. To detect experimentally the Fermi arc, one has to employ independent surface-sensitive ARPES (Angle-Resolved Photoemission Spectroscopy)[39,40]. Experimentally in parallel with the bulk-sensitive soft X-ray measurements, independent surface-sensitive ARPES investigations conducted at vacuum ultraviolet photon energies have demonstrated the presence of distinctive arcs on the (001) surface of TaAs (See ***Figure 1.7a, b*** The Fermi surface, as characterized by ARPES, exhibits three prominent features. These include a bowtie-shaped feature with its centre located at the $\bar{X}$ point, an elliptical feature centred at the $\bar{Y}$ point, and a crescent-shaped feature positioned near the midpoint of each $\bar{X}$, $\bar{Y}$ (See ***Figure 1.7d, e).***

Chiral anomaly in Weyl semimetals:

In the realm of classical physics, chirality is a fundamental and unchanging physical attribute, akin to angular momentum, energy, or electrical charge. This foundational principle mandates the overall conservation of chirality, preventing an arbitrary dominance of one chirality over its counterpart. However, a pivotal revelation emerged from a 1970s accelerator experiment, challenging the classical preservation of chirality when subjected to parallel electric and magnetic fields at the quantum level. This departure from chirality conservation manifested itself in the decay of a neutral pion into two photons, a process seemingly prohibited by the established law of chirality conservation.

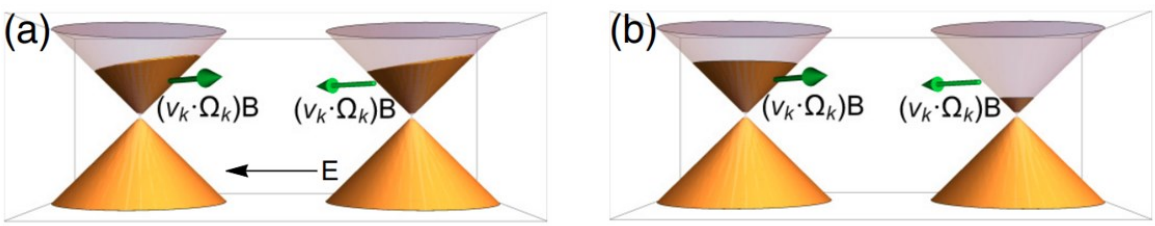

Figure 1.8. (a)*Weyl cone without applied magnetic field* ***(b)*** *Weyl cone with applied magnetic field (adapted from Ref [])*

Notably, even though the involved particles are bosons, distinct from massless Fermions, chirality still holds a defined meaning. However, unlike massless Fermions, it cannot be directly associated with the handedness of the particles. In the context of electronic transport inside a condensed matter system, the effect of chiral anomaly can be understood using semiclassical Boltzmann transport formalism. To capture the physics, two opposite chiral Weyl cones are considered (as depicted **in Figure 1.8a, b**). To describe the electron's motion in a crystal, one must rely on the semiclassical formula and according to that formulism, current density can be written as[41,42]:

$$\boldsymbol{j} = -e \int \frac{d\boldsymbol{k}}{(2\pi)^3} \mathrm{D}(\boldsymbol{B}, \boldsymbol{\Omega_k})^{-1} \dot{\boldsymbol{r}} f_k(\mathbf{r}) \qquad \ldots.1.15$$

Here, phase space volume is denoted by $\mathrm{D}(\boldsymbol{B}, \boldsymbol{\Omega_k})$ and it is equal to $[1 + e/\hbar(\boldsymbol{B} \cdot \boldsymbol{\Omega_k})]^{-1}$ when the system with finite Berry curvature is exposed to a magnetic field. The following two equations are used to describe the motion of the wave packet of the charge carrier with magnetic field in action.

$$\dot{\boldsymbol{r}} = \frac{1}{\hbar}\frac{\partial \epsilon}{\partial \boldsymbol{k}} - \boldsymbol{k} \times \boldsymbol{\Omega_k} \qquad \ldots\ldots1.16$$

$$\dot{\boldsymbol{k}} = e\boldsymbol{E} - \dot{\boldsymbol{r}} \times \boldsymbol{B} \qquad \ldots\ldots1.17$$

$$\dot{\boldsymbol{r}} = D\,(\boldsymbol{B}, \boldsymbol{\Omega_k})\,[\,\boldsymbol{v_k} + \frac{e}{\hbar}\boldsymbol{E} \times \boldsymbol{\Omega_k} + \frac{e}{\hbar}\,(\boldsymbol{v_k} \cdot \boldsymbol{\Omega_k})\boldsymbol{B}] \qquad \ldots..1.18$$

$\dot{\boldsymbol{r}}$ describe the group velocity. $f_k(\mathbf{r})$ is used to denote the distribution function of electron reside at state **k** with the real space position is **r**.

The distribution function can be evaluated using semiclassical Boltzmann transport formulism assuming **k**-independent relaxation time

$$\dot{\boldsymbol{k}} \partial_{\boldsymbol{k}} f_k(\boldsymbol{r}) = \frac{f_{eq}(r) - f_k(r)}{\tau(k)} \qquad \ldots..1.19$$

Using this, we can get

$$f_k(r) = f_{eq}(r) + [eD\,\tau \boldsymbol{E}.\boldsymbol{v_k} + \frac{e^2}{\hbar} D\tau\,(\boldsymbol{v_k} \cdot \boldsymbol{\Omega_k})(\boldsymbol{B}.\boldsymbol{E}) + \textbf{\textit{higher order terms}}]\frac{\partial f_{eq}}{\partial k} \ldots1.20$$

The deviation from the equilibrium state comprises three components. The first term accounts for the altered distribution influenced by the electric field E, with the component of $\mathbf{v_k}$ along **E** playing a pivotal role. The second term introduces the concept of the chiral chemical potential, signifying the phenomenon where electron travels from one chiral Weyl cone to another oppositely chiral Weyl cone when electric and magnetic

fields are parallel configuration. The overall contribution of the term ($\mathbf{v_k}$. **k**) **B** is non-zero from the opposite chiral Weyl cone.

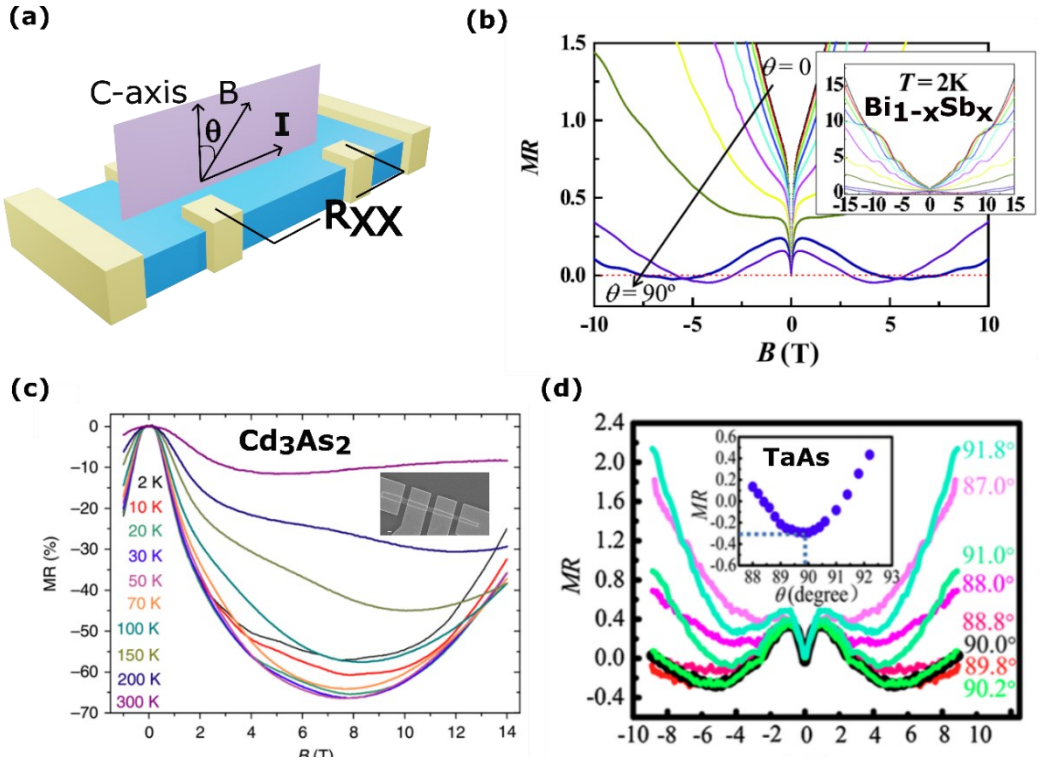

Figure 1.9 (a) *The schematic diagram of the LMR configuration with θ being the angle between current(I) and magnetic field(B). First observation NMR in Dirac metal* ***(b)*** *$Bi_{1-x}Sb_x$. (inset shows full range LMR data upto 15 T) (adapted from Ref [40])* ***(c)*** *Cd_3As_2. (adapted from Ref [28])**(d)** The first experimental signature of chiral anomaly driven NMR observed in inversion symmetry broken pure Weyl semimetal TaAs(adapted from Ref [41])*

the electric field and magnetic field are not perpendicular to each other, then the velocity due to Berry curvature (v_k. k) B and the chemical difference between the chiral Weyl cone shall give rise to additional conductivity which is proportional to B^2. This phenomenon is known as a chiral anomaly. Experimental observation of negative longitudinal magnetoresistance is believed to be caused by chiral anomaly (see **Figure 1.8**). As a result of this event, an additional unique symmetric (under reversal of magnetic field direction) Hall effect also appears in the Weyl system without Lorentz force which is known as the planar Hall effect. Experimental consequences of chiral anomaly first occur in a topological Dirac semimetal where TRS is broken by the magnetic field, and the Dirac semimetal turns into a Weyl semimetal and shows NMR. Examples of such Dirac semimetal is $Bi_{0.97}Sb_{0.03}$ crystal[43], Na_3Bi[27], and Cd_3As_2[29]. [44](see **Figure 1.9a-c**). However, it was in the year 2015, that experimental observations of negative longitudinal magnetoresistance were made within an inversion asymmetric pure Weyl

semimetal TaAs[44](see **Figure 1.9d**).

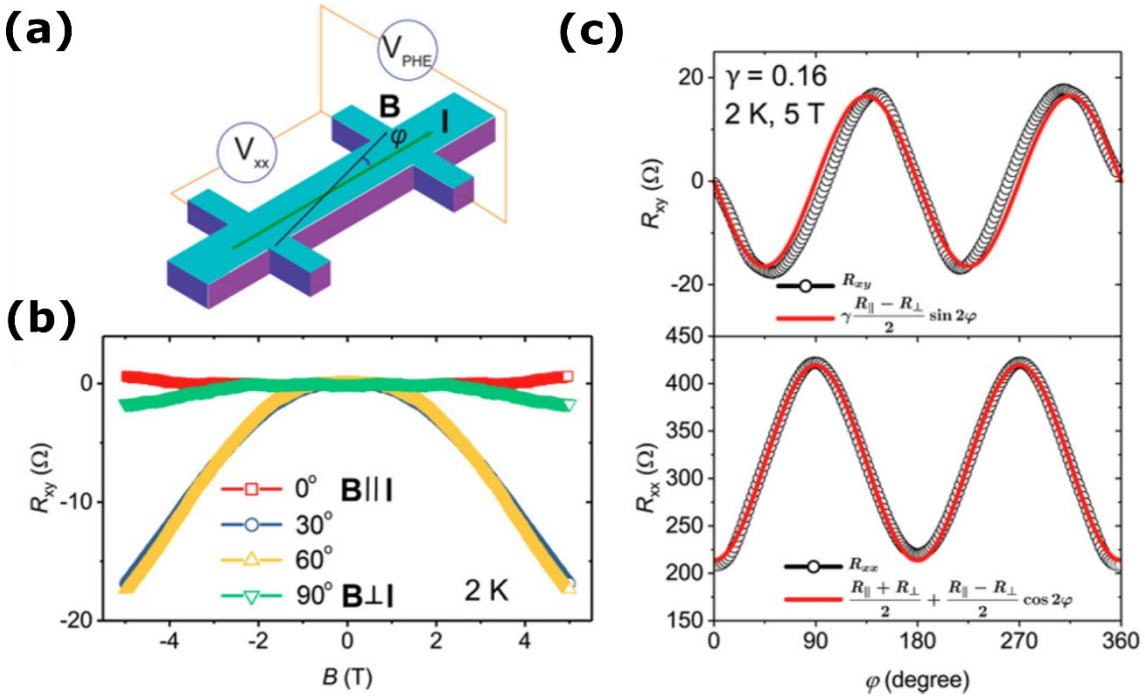

Figure 1.10 ***(a)*** *The schematic illustration of device configuration of the measurement of PHE of Cd_3As2.* ***(b)*** *The magnetic field variation of the Rxy measured at 2 K at different angle between current and magnetic field in the x-y plane.* ***(c)*** *The angular variation of the PHE signal(top) and in-plane resistance(bottom) at T= 2 K and B= 5 T (adapted from Ref [42]).*

Parallelly, the planar Hall effect (PHE) is another experimental signature for the chiral anomaly. It was first observed in a topological Dirac semimetal Cd_3As_2 along with NMR[45] (see **Figure 1.10a-c**).

Experimental signature of tilted Weyl/Dirac semimetal:

Berry curvature dipole driven Non-linear hall effect:

Weyl semimetals can be classified depending on the violation of Lorentz symmetry. Type I obeys Lorentz symmetry while type II breaks it and the Weyl cone shows significant tilting. The TaAs family of WSMs demonstrates characteristic Weyl cones in the bulk band structure and falls into the type-I category, where the Fermi surface condenses to a singular point at the Weyl point. More recently, the existence of type-II WSMs has been proposed in layered transition-metal dichalcogenides such as WTe_2 [46,47] and its counterpart $MoTe_2$ [48]. In these materials, both electron and hole pockets are present at the Fermi level. Type-II WSMs display anisotropic chiral anomaly, unique anomalous Hall effect[49], non-linear Hall effect[50–53], unusual

Seeback effect[54] , quasi-linear LMR, TMR, and PHE.[41,55,56]

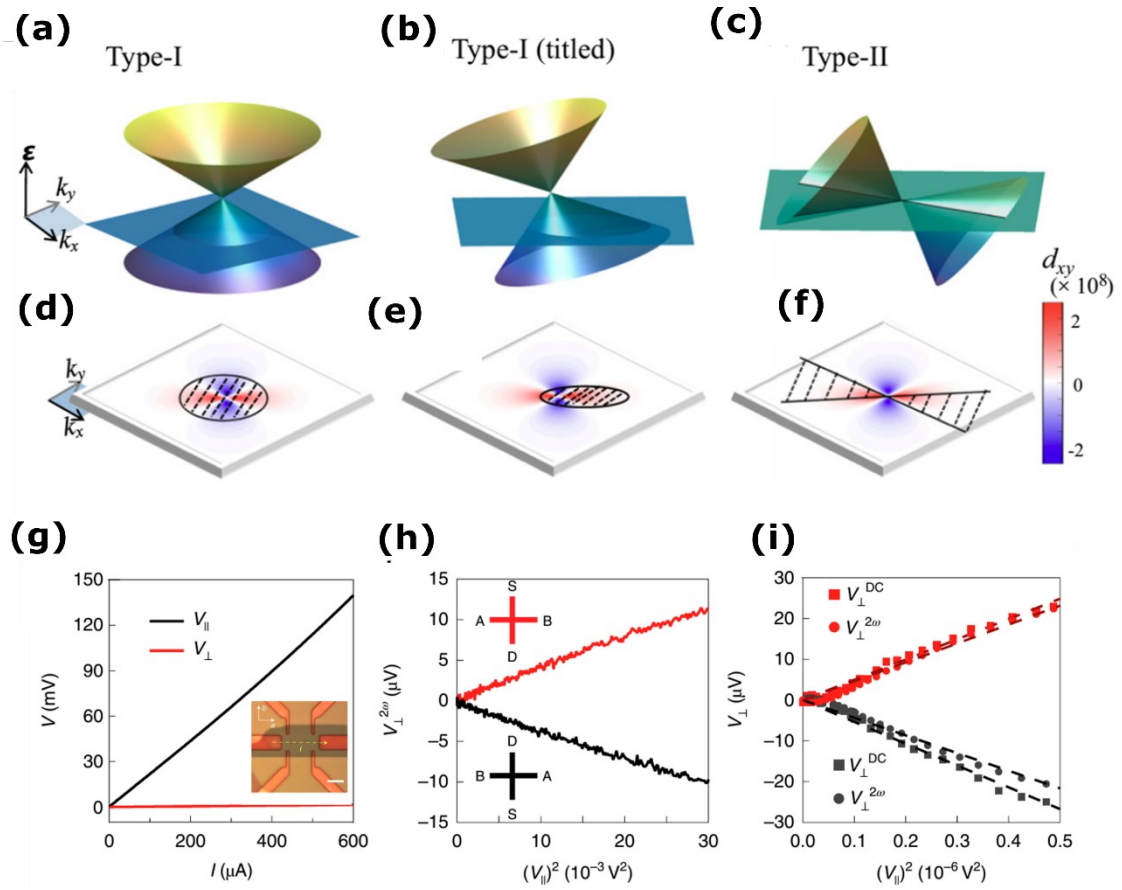

Figure 1.11 (a) *The Weyl cone of type -I* ***(b)*** *The Weyl cone of tilted type-I in nature* ***(c)*** *The Weyl cone of type-II in nature* ***(d)*** *BCD corresponding to the Wey cone of type -I.* ***(e)*** *BCD corresponding to the tilted type-I. (f) BCD corresponding to the tilted type-II.(the images from (a) to (f) are adapted from Ref[48]* ***(g)*** *I-V characteristic of* WTe_2 *in longitudinal and transverse direction to demonstrate ohmic contact.* ***(h)*** $V_\perp^{2\omega}$ *vs.* $V_{||}$ *in two configuration as shown in the top and bottom left inset. Red one describe Hall signal during forward current and black one is used to denote the result during reverse current. The result here are taken from five layered device* ***(i)*** *Here the same results* $V_\perp^{2\omega}$ *vs.* $V_{||}$ *in two configuration is plotted for four layered device (adapted from Ref [47]).*

An additional captivating experimental approach that can be utilized for discerning the characteristics of non-trivial electronic bands involves the utilization of the non-linear Hall effect. Hall effects fall short in exploring the complex geometric traits of Bloch states in materials that obey time-reversal invariance while breaking inversion symmetry. A recent breakthrough uncovers a crucial insight. The prior assertion holds only within the linear response regime, where Hall voltages exhibit linear proportionality to the external electric field. The narrative shifts when nonlinear Hall currents, with a quadratic relationship to the external

electric field, manifest even under time-reversal symmetric conditions. The genesis of this nonlinear phenomenon links to an intrinsic contribution tied to a concept akin to the dipole moment of the Berry curvature, called the Berry curvature dipole (BCD). Topological materials characterized by an asymmetric distribution of Berry curvature in momentum space manifest this distinctive non-linear Hall effect. A significant Berry curvature dipole (BCD) is present in systems with tilted Type I or II Weyl cones and systems with tilted massive Dirac cones.

1.3 Electronic correlation:

Fundamental to the realm of solid-state physics is the underpinning concept known as the free electron theory. This theoretical framework characterizes electrons within a condensed matter system as entirely devoid of interactions. An enhancement to this model arises when corrections, in the guise of the periodic lattice potential, are incorporated. This evolution transforms the theory into the realm of the nearly free electron theory, rendering it more precise in depicting actual material systems. This refined model extends its applicability to a diverse array of materials, encompassing metals, semiconductors, and insulators.

Substances exhibiting characteristics beyond the scope of explanation provided by the unbound or nearly unbound electron theory, which neglect electron-electron interactions, present a realm of intricacy. Within heavy fermion systems, a phenomenon of hybridization manifests between the f-shell and the conduction electrons, frequently resulting in substantial alterations to the electron mass through a process known as renormalization[57]. Interactions involving electrons and phonons possess the capability to generate an attractive potential between two electrons, thereby facilitating the coherent formation of Cooper pairs within BCS superconductors. This mechanism serves as a resolution to a Fermi surface instability. Additionally, the manifestation of charge density waves (CDWs) stems from instabilities at the Fermi energy. In this context, these instabilities are mitigated through energy minimization achieved by introducing a periodic lattice modulation. Similarly, spin density waves (SDWs) manifest as fluctuations in the magnetic moment rather than variations in electron density[58,59]. Many of these complex electronic states either work together or compete within the same materials. The iron pnictides, for instance, frequently exhibit both SDW and unconventional superconductivity (SC), facilitated by magnetic influences. In the domain of heavy fermions, a superconducting ground state often suppresses the dominant magnetic order. Transition metal dichalcogenides (TMDs) and cuprates offer yet another instance where the dual characteristics of superconductivity (SC) and charge density wave (CDW) behaviors are observed.

1.3.1 Charge density wave (CDW):

In the realm of charge density wave (CDW) transitions, encompassing both two-dimensional

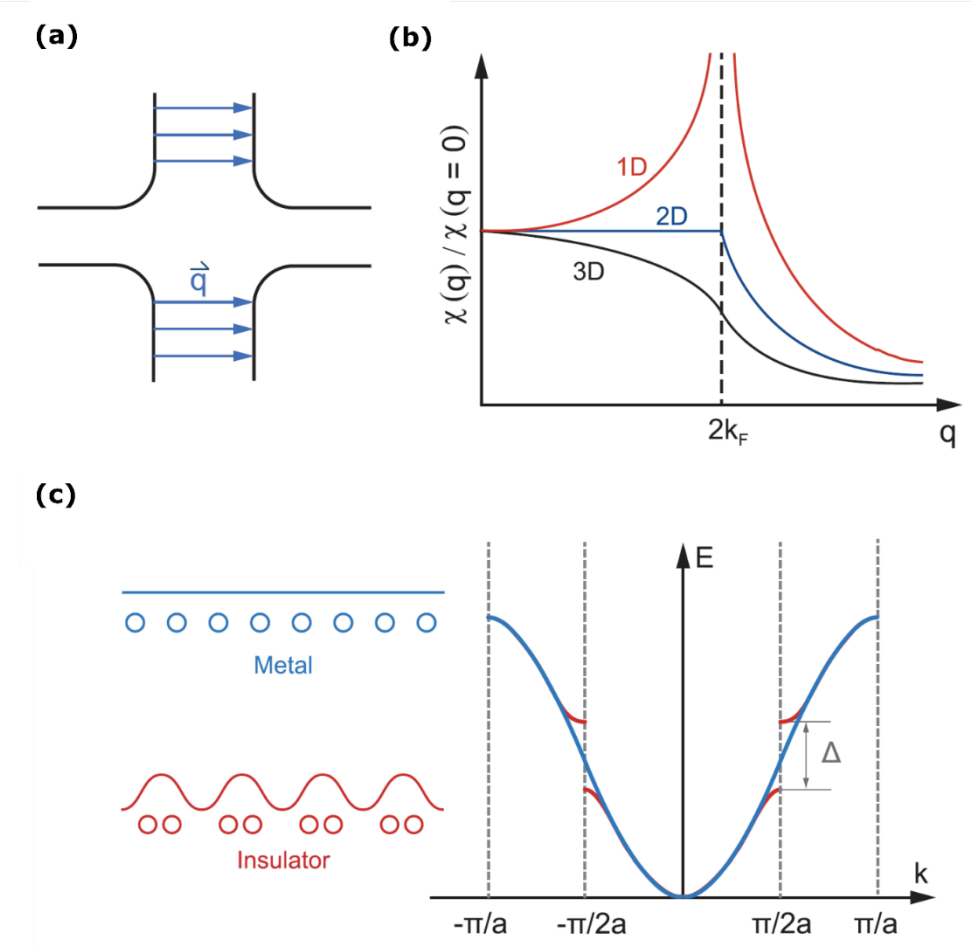

Figure 1.12 (a) *A depiction of Fermi surface nesting showcasing a wavevector q.* ***(b)*** *The zero-temperature Lindhard response function c(q) one-, two-, and three-dimensional free electron gases.* ***(c)*** *Conceptual portrayal of a Peierls transition for a one-dimensional substance, featuring the configuration and dispersion pre-(post-) transition depicted in blue (red). A distinct gap emerges at the wavevector q = 2k$_F$, aligning with the fresh lattice periodicity (adapted from Ref [60]).*

(2D) and three-dimensional (3D) systems, elucidation is commonly provided by three distinct models: Fermi surface nesting (FSN), electron-phonon coupling (EPC), and excitonic insulator (EI). Transition metal dichalcogenide (TMD) materials consistently exhibit the requisite conditions for these intricate mechanisms. Moreover, the pervasive manifestation of CDW as a phenomenon with diminished dimensionality finds an apt host in the stratified structure of TMDs, rendering them a versatile and accommodating platform for the intricacies of CDW behaviour[60–62].

1.3.1.1 Peierls distortion

The genesis of FSN (see **Figure 1.12a**) CDW traces its origins to the Peierls distortion of pure 1D metals. As portrayed in **Figure 1.12c,** the atomic chains of 1D metals succumb to instability at lower temperatures. A key change happens when the lattice constant doubles, causing the Brillouin zone to be cut in half. This change creates an energy gap at $k = \pm\pi/2a$, giving rise to electronic modulation characterized by a wave vector of $2k_F$ (displayed in **Figure 1.12c**). The intricate interplay between lattice distortion and electronic energy reveals a delicate equilibrium, with the elastic energy from the former proving less than the reduction in the latter. Consequently, the doubled lattice stands as an energetically stable configuration. Noteworthy in this context is the equivalence of the CDW vector ($q_{CDW} = 2k_F$) to the vector linking the Fermi surface zone boundary ($k = \pm\pi/2a$). This complex phenomenon is called 1D FSN. and, to some extent, extends its influence to 2D scenarios, wherein CDW arises from FSN as parallel Fermi surface (see **Figure 1.12a**) contours find connection through a CDW wave vector, known as the FS nesting vector (q_{FS}).

The Peierls transition, marked by the opening of the Fermi surface gap, precipitates a transition from a metallic to an insulating state. In instances where the periodicity of the electron density aligns as a rational multiple of the lattice distortion, a commensurate charge density wave (CCDW) materializes. Conversely, when the ratio of the two periodicities assumes an irrational number, an incommensurate charge density wave (ICDW) ensues, resulting in an electron density that oscillates out of phase with the lattice distortion. Consequently, the fundamental aspects of Peierls' model encompass: the manifestation of FSN within the electronic structure, a distinct spike evident in the Lindhard function **(**see **Figure 1.12b**), the emergence of a Kohn anomaly within phonon spectra, a pivotal transition within the lattice structure, and a transformation from metal to insulator state.

1.3.1.2 Role of Electron-Phonon Coupling (EPC)

In a stratified quasi-2D material $NbSe_2$, the traditional and extensively studied CDW system, a plethora of investigations [63–69] have revealed that the observed charge ordering phase shift diverges from the Peierls' depiction. Specifically, there is no indication of Fermi surface nesting. $NbSe_2$ possesses a hexagonal stratified arrangement with a lattice constant of 3.443 Å. Initial diffraction analyses[70,71] and recent scanning tunnelling microscopy (STM) observations [63] have consistently verified the structural transition at $T_{CDW} = 33.5$ K, with $q_{CDW} \cong 0.7$ Å^{-1}.

Recent inelastic X-ray scattering experiments [66] disclosed a Kohn-like irregularity in phonon spectra and demonstrated that phonon softening centred around $q_{CDW} \cong 0.7$ Å^{-1} triggered the structural transition. Nevertheless, the measured resistivity versus temperature displayed no alteration at the CDW transition temperature, suggesting the absence of a metal-insulator transition linked with the structural transition. Most notably, as illustrated in ***Figure 1.13a***, the Fermi contour derived from ARPES measurements does not show any sign of FSN[65]. A diagram (***Figures 1.13a***) illustrates the Fermi contour derived from the precise fitting of ARPES data, side by side with the wavevector of the charge density wave (~q_{CDW}), determined through diffraction analyses. Attributing the emergence of the charge density wave to Fermi surface nesting (FSN) is untenable. The lack of FSN becomes evident in the Lindhard susceptibility function plots (both real and imaginary is shown in ***Figure 1.13 b,c*** generated from the assessed electronic structure[61]. These plots exhibit no discernible peak at the q_{CDW} position[65].

Mazin and colleagues employed the traditional CDW materials $NbSe_2$, $TaSe_2$, and $CeTe_3$ to

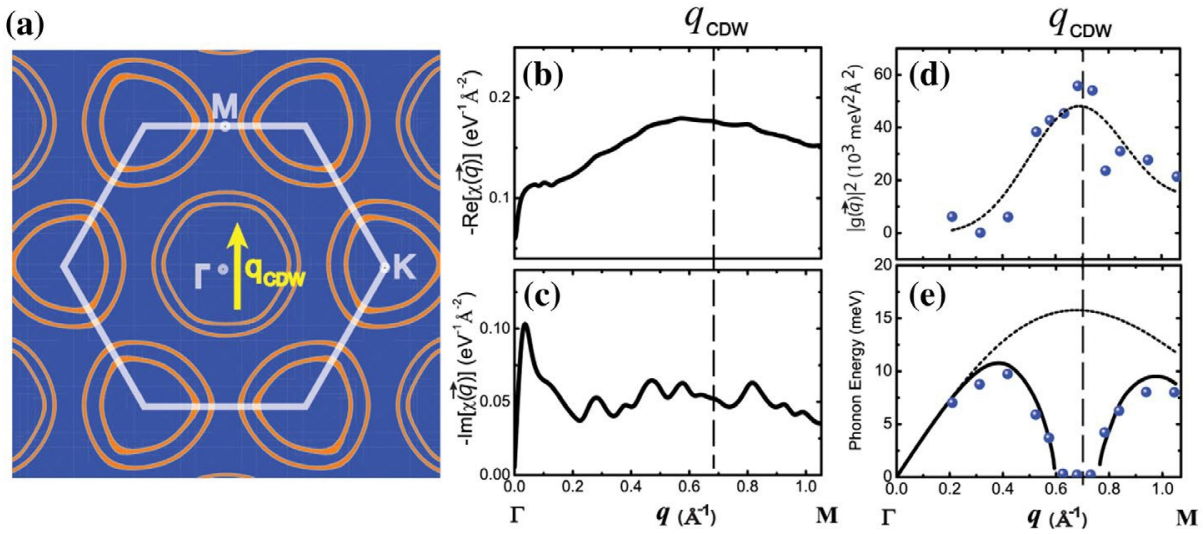

Figure 1.13 (a) *Illustration of Fermi Surface contours alongside the experimental* $\vec{q}_{CDW}$. *of* $NbSe_2$ ***(b)*** *Re*$\chi(q)$ *and* ***(c)*** *Im*$\chi(q)$ *are computed from empirical evidence in the ΓM direction.* ***(d)*** *Present the derived Electron-Phonon Coupling (EPC) matrix element* $g(\vec{q})^2$. ***(e)*** *Depict the observed phonon dispersion (points) at T = 8 K and predict the soft phonon behavior (solid line) utilizing* $g(\vec{q})^2$ *and an estimated bare phonon (dashed line) dispersion (adapted from Ref [54,55]).*

support their conclusion and demonstrated that by adequately incorporating EPC, the observed properties could be elucidated[67,68]. It is evident, therefore, that experimental investigations should thoroughly examine the phonon spectra to ascertain the q-dependence of EPC (as shown in ***Figure 1.13d)***. While one might assert that both FSN and EPC entail electron-lattice interaction, wherein electrons transition from occupied to unoccupied states, they must be

delineated due to the distinct nature of their scattering mechanisms: FSN entails elastic scattering, whereas EPC involves inelastic scattering from the lattice.

Inelastic X-ray scattering unveils a temperature-dependent peculiarity in the acoustic phonon branch at a specific wave vector, denoted as q_{CDW}. The observed data on the modified phonon dispersion along the direction from Γ to M (***Figure 1.13 b,c***) distinctly illustrates a pronounced softening of phonons occurring approximately at $q_{CDW} \cong 0{:}695$ $Å^{-1}$, suggesting a direct correlation between the charge density wave (CDW) and the observed anomaly akin to the Kohn effect. Just preceding the transition temperature, the phonon energy exhibits an imaginary component, signifying a structural rearrangement of the lattice. Beyond the transition temperature, there is a noticeable reduction in phonon energy near q_{CDW}, albeit it does not reach zero.

1.3.1.3 Excitonic insulator:

Jerome and colleagues [72] introduced the concept of the excitonic insulator mechanism. In semiconductors characterized by a narrow band gap or semi-metals with minimal band overlap, the population of charge carriers remains limited. Within this context, these carriers have the propensity to coalesce into excitons—composite entities comprising bound hole-electron pairs. This phenomenon occurs when the indirect gap, whether positive in semiconductors or negative in semi-metals, is smaller than the binding energy of the exciton. Consequently, this process extracts charge carriers from the Fermi surface, instigating the formation of an insulating state. In scenarios involving an indirect gap, the outcome is a nonzero exciton momentum, thereby triggering a subsequent transition to a charge density wave (CDW).

1.3.1.4 The Jahn–Teller effect:

The Jahn–Teller effect, originally proposed by Hughes, is instigated by a structural distortion that disrupts the degeneracy of the ground state energy[73]. To exemplify, the transition metal T within the TX_2 dichalcogenides can adopt either octahedral (1T) or trigonal prismatic (2H) T-X_6 coordination. Distinct energies characterize the transition metal d bands contingent upon the octahedral or trigonal prismatic T-X_6 coordination, where the 2H polytype exhibits a lower d_z^2 energy than its 1T counterpart. Consequently, a transition to trigonal coordination could diminish the energy of the octahedral polytype. This transition occurs when the chalcogen ions X surrounding a transition metal ion, T, in the octahedra, rotate in opposing directions.

Consequently, a localized augmentation in conduction electron density (negative charge) emerges at the corners of the unit cell, constituting an attractive potential for the positively charged T ions. The outcome is a lattice distortion propelled by a T-X coordination in real space, rendering it a manifestation of the band Jahn–Teller effect rather than a Fermi surface effect.

The phase shifts linked to charge density wave (CDW) occurrences vary significantly depending on the system. No single mechanism universally applies across all materials. Typically, the transition's mechanism proves far more intricate than the simplified Peierls' model. Comprehending the nuances of structural shifts alongside the anisotropic electronic structure is essential for delving into the roots of the phase transitions observed in transport measurements.

1.3.2 Magnetism:

Another phenomenon which is caused by the electronic interaction is magnetic ordering in a material system. This phenomenon is driven by the quantum mechanical exchange interaction, denoted as J, operating between neighbouring moments. Initially proposed independently by Werner Heisenberg and Paul Dirac, this interaction accounts for the electrostatic forces considering the Pauli exclusion principle[42,74].

All materials are composed of atoms, and the way matter behaves is intricately connected to the arrangement of these atoms and their interactions with each other. Within an atom, electrons, which carry a negative charge, can be described as circling the nucleus, possessing an orbital angular momentum denoted by L. Classical mechanics dictates that,

$$L = \boldsymbol{r} \times m_e \boldsymbol{v} \qquad \text{.....1.21}$$

In this scenario, with r, m_e, and v representing the electron's orbital radius, mass, and velocity respectively, the expression for the magnetic dipole moment m of a small current loop can be derived as follows:

$$\boldsymbol{m} = IA\boldsymbol{u}_N = I\pi r^2 \boldsymbol{u}_N \qquad \text{.....1.22}$$

$$\text{and the current} \quad I = e\omega = \frac{e\ v}{2\pi r} \qquad \text{.....1.23}$$

In this scenario, e represents the charge of an electron, while ω stands for the angular frequency of said electron, u_N the unit vector normal to area A. When we integrate Equations 1.21, 1.22, and 1.23 together, we obtain

$$m = -(e)/(2m_e)L \qquad \text{.....1.24}$$

In this context, the parameter $-e/2m_e$ is referred to as the gyramagnetic ratio.

Due to the motion of electrons, all atoms inherently possess a magnetic dipole moment, rendering all matter susceptible to magnetic influence. However, the generation of this magnetic moment isn't solely attributed to the orbital angular momentum (**L**) of electrons. In quantum mechanics, another crucial factor called intrinsic (spin) angular momentum (**S**) exists. Essentially, all elementary particles, including electrons, possess spin, akin to their angular momentum around their respective axes. This spin, being a purely quantum mechanical concept with no classical counterpart, also contributes to the generation of a magnetic dipole moment. Consequently, the total angular momentum (J) is defined as the sum of orbital and spin angular momenta, **J = L + S**. As emphasized by Mattis and Gould[74] , spin (S) plays a significantly larger role in determining a material's magnetic properties compared to orbital angular momentum (**L**), with the latter often found negligible.

Given that all substances exhibit some degree of response to a magnetic field, it is relevant to clarify the notion of magnetic materials. These materials can be categorized based on the alignment of their magnetic dipoles: parallel, anti-parallel, or lacking alignment altogether. When individual dipole moments exhibit random orientation resulting in a net sum of zero ($\Sigma m = 0$), the material is termed paramagnetic or diamagnetic. In colloquial terms, such materials are often labelled as non-magnetic. Nonetheless, paramagnetic and diamagnetic substances may display partial alignment under the influence of an external magnetic field. Conversely, if dipole moments exhibit non-random alignment even in the absence of external magnetic influence, the material is classified as ordered. Ordered magnetic materials encompass ferromagnets, antiferromagnets, and ferrimagnets. Table 2 illustrates various examples of distinct magnetic materials.

1.3.2.1 Diamagnetism and Paramagnetism:

In materials exhibiting diamagnetism or paramagnetism, the individual dipole moments *m* lack interaction, leading to random orientation and a resultant zero net magnetic moment, as depicted in **Table 1 row 2**. However, when subjected to an external magnetic field, these dipole moments can undergo partial alignment. Yet, upon removal of the applied magnetic field, these materials do not retain any magnetization due to the dominance of intrinsic thermal energy over the potential energy organizing the dipoles, resulting in thermal agitation that randomizes the orientations of *m*. The distinction between these materials lies in the direction of the induced magnetic field: paramagnetic materials exhibit a magnetic field aligned with the applied field, while diamagnetic materials show a field opposed to it. Diamagnetism arises from the motion

of electrons around nuclei, as per Lenz's Law, wherein the application of an external field prompts electrons to adjust their velocity to counteract changes in magnetic flux. Diamagnetic effects are inherent in all matter due to electron motion, albeit usually subtle. Often, diamagnetism is overshadowed by paramagnetism or ferromagnetism in many materials. Paramagnetism's accurate description necessitates a quantum physics framework. Atoms within paramagnetic materials possess an electron spin denoted by S, which remains nonzero. Upon the application of an external magnetic field, these spins align themselves with the field direction, thereby generating a magnetic field parallel to the external field.

1.3.2.2 Ferro, Ferri, Antiferro-magnetism :

Ordered magnetic materials exhibit a structural configuration wherein their dipole moments naturally align in specific orientations relative to each other. Despite thermal agitation, these materials maintain fixed dipole moment arrangements due to insufficient energy to randomize them. In ferromagnets, all dipole moments align parallelly, facilitating their magnetic behaviour as depicted in **Table 1** Conversely, antiferromagnets and ferrimagnets feature dipole moments coupled in antiparallel configurations, resulting in mutual cancellation. The distinguishing factor between antiferromagnets and ferrimagnets lies in the extent of this cancellation.

In antiferromagnets, dipole moments within sublattices possess identical magnitudes, resulting in complete cancellation, as shown in **Table 1 row 4**. Conversely, ferrimagnets exhibit dipole moments of varying magnitudes, illustrated in **Table 1 row 5**, resulting in a nonzero net magnetic moment. This macroscopic distinction leads antiferromagnets to behave akin to non-

Table 1. Summary of magnetic materials (taken from Ref [57])

Magnetism	Examples	Magnetic behaviour		
Diamagnetism	Bi, Si, Cu, inert gases Susceptibility small and negative (-10^{-6} to -10^{-5})	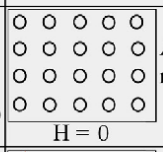	Atoms have no magnetic moments.	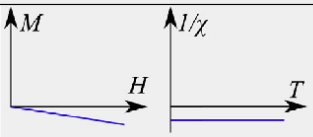
Paramagnetism	Al, O_2, MnBi Susceptibilty small and positive (10^{-5} to 10^{-3})	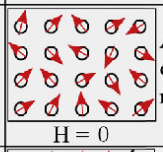	Atoms have randomly oriented magnetic moments.	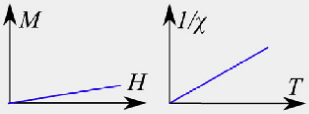
Ferromagnetism	Fe, Ni, Co, Gd Susceptibility large (generally > 100)	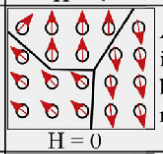	Atoms are organized in domains which have parallel aligned magnetic moments.	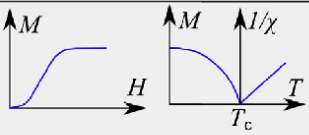
Antiferromagnetism	Cr, MnO, FeO Susceptibilty small and positive (10^{-5} to 10^{-3})	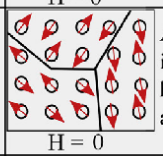	Atoms are organized in domains which have antiparallel aligned moments.	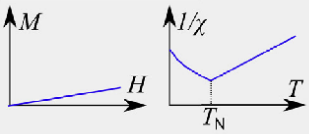
Ferrimagnetism	Fe_3O_4, $MnFe_2O_4$, $NiFe_2O_4$ Susceptibility large (generally > 100)	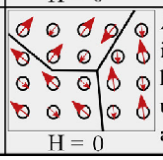	Atoms are organized in domains which have a mixture of unequal antiparallel aligned moments.	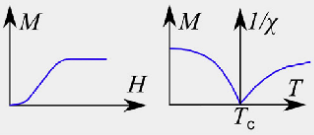

magnetic materials, while ferrimagnets resemble ferromagnetic substances. In materials exhibiting ferro-, ferri-, and antiferromagnetic, the interaction between the intrinsic atomic magnetic moments gives rise to a long-range spatial arrangement. This phenomenon is driven by the quantum mechanical exchange interaction, denoted as J, operating between neighbouring moments. Initially proposed independently by Werner Heisenberg and Paul Dirac, this interaction accounts for the electrostatic forces considering the Pauli exclusion principle. It involves two electrons whose total wave function must be antisymmetric, leading to either a spin-singlet state ($S = 0$) or a spin-triplet state ($S = 1$), characterized by energy eigenstates E_S and E_T. The exchange interaction is quantified as the energy disparity between the singlet and triplet eigenstates, expressed as $J = E_S - E_T$. When $E_S < E_T$, resulting in $J < 0$, the singlet state becomes energetically favourable, leading to antiparallel alignment of spins. Conversely, when $E_S > E_T$, favouring parallel alignment results in ferromagnetic coupling.

1.4 Correlation and topology

1.4.1 Topological materials with electronic interaction:

Numerous collective instabilities and fundamental aspects of topology captivate researchers in the field of condensed matter studies. It proves intriguing to investigate the intricate relationship between these occurrences within a solitary quantum substance, paving the way for an array of extraordinary characteristics. For instance, within $(TaSe_4)_2I$, the onset of a charge density wave (CDW) transition at temperatures below 263 K triggers the emergence of axion insulator properties by unveiling Weyl nodes[75]. Conversely, the induction of superconductivity in Weyl semimetals WTe_2 and $MoTe_2$ under pressure enables their topological edge states to exhibit superconducting behaviour, holding promise for advancements in quantum computation[76,77]. In the research area of topology and correlation, Kagome metals AV_3Sb_5 (where A = K, Rb, and Cs) show huge potential. The electronic bands neighbouring the Fermi energy in AV_3Sb_5 showcase intriguing characteristics, featuring Dirac cones and van Hove singularities (VHSs), distinguished by their peculiar odd Z_2 indices. These features potentially induce anomalous Hall effects within a magnetically frustrated sublattice. Furthermore, the onset of in-plane 2 × 2 CDW and superconducting orders beneath their respective critical temperatures in AV_3Sb_5 further sparks intense scrutiny regarding their formation mechanisms and intricate interplay[78,79]

The topological Kondo insulator represents a distinct category within heavy-fermion correlated systems. Initially observed four decades ago, Kondo insulators were recognized as narrow-gap semiconductors. It has been highlighted that conventional Kondo insulators can be classified topologically. Notably, SmB_6[80] and YbB_{12} [81] have garnered significant interest as potential topological Kondo insulators. The presence of topologically protected surface states has been identified as the underlying cause of a longstanding puzzle: the low-temperature saturation of electrical resistivity. Furthermore, in addition to the topological Kondo insulator, recent investigations have unveiled a distinct type of topological state termed Weyl-Kondo semimetals. Examples include the non-centrosymmetric compound $Ce_3Bi_4Pd_3$[82] and the centrosymmetric material YbPtBi[83] when subjected to a magnetic field. Noteworthy aspects of these studies encompass the examination of electron correlation's impact on topological transport characteristics and the exploration of Weyl semimetals proximate to the magnetic field-induced quantum critical point. The profound influence of electron correlation serves to enhance the diversity of topological states in materials.

1.4.1.1 Interplay between topology and CDW:

In their investigation, the quasi-one-dimensional substance $(TaSe_4)_2I$[75] recently demonstrated to exhibit Weyl semimetal characteristics in its unaltered configuration (Figure 1b). Its Fermi boundary originates solely from Weyl cones, hosting 24 pairs of Weyl points with opposing

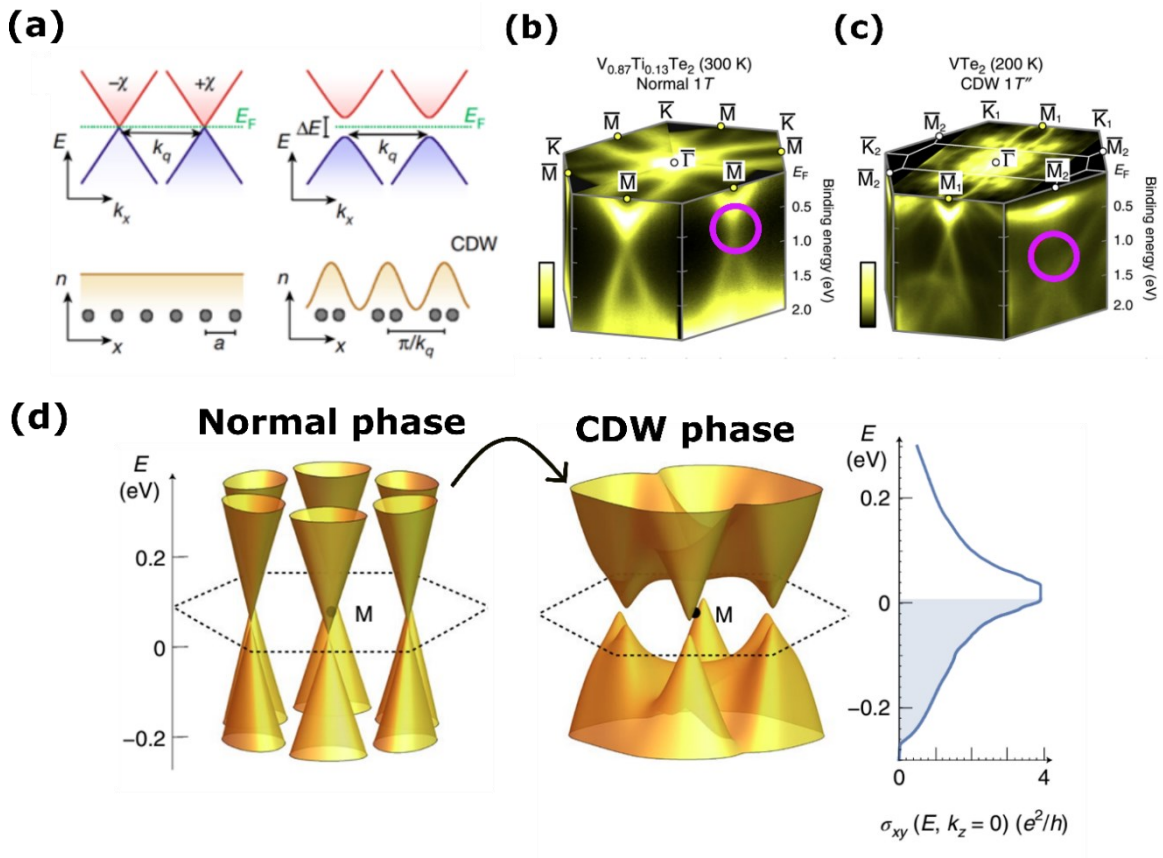

Figure 1.14(a) *CDW mediated gapping out of the Weyl cone to form an axionic insulator of $(TaSe_4)_2I$ (adapted from Ref [75])* ***(b)*** *An aerial perspective ARPES depiction reveals 1T-$V_{0.87}Ti_{0.13}Te_2$ at 300 K, utilizing a photon energy of 21.2 eV.* ***(c)*** *Similarly, another depiction, mirroring the former, illustrates 1T"-VTe_2 at 200 K, employing a photon energy of 90 eV(adapted from Ref [84]).* ***(d)*** *The emergence of a chiral time-reversal breaking CDW modulation initiates a topological gap opening at the Fermi level (on the left). This separation results in a nonzero Berry curvature, whose accumulation induces a substantial anomalous Hall effect (depicted on the right). This depiction showcases the anomalous Hall conductance σ_{xy} vs. E at $k_z = 0$. σ_{xy} is expressed in units of e^2/h, with e representing the elemental charge and h denoting Planck's constant (adapted from Ref [85]).*

Below the critical temperature, Tc = 263 K, $(TaSe_4)_2I$ adopts an incommensurate CDW state, undergoing a transition akin to Peierls phenomena, concomitant with the emergence of a gap of approximately 260 meV in single-particle excitations. This gapped material is believed to be an axionic insulator (see **Figure 1.14a)**. Another example of the intricate interplay between CDW and topology is described in 1T-VTe_2, where a flat band appears due to the formation of

CDW from a Dirac-like band[84] (see **Figure 1.14 b,c**). In the Ref [84], they initiate with $TiTe_2$ exhibiting a straightforward 1T configuration reaching the minimum temperature, then progress towards the single crystal $V_{1-x}Ti_xTe_2$ to reach both 1T and 1T″ phases at suitable temperatures. The chiral time-reversal breaking CDW order creates a gap near the Fermi level in the Kagome superconductor KV_3Sb_5. This gap engenders a non-vanishing Berry curvature, which produces a remarkable anomalous Hall effect[85].Another example of topological correlated materials, $EuAl_4$ [86], undergoes a series of antiferromagnetic (AFM) transitions in its CDW-ordered state and exhibits a topological Hall signal inside the complex CDW state with probable chiral spin texture.

Lanthanum-based $LaAgSb_2$ from the square net series has been rigorously studied for decades due to its exotic properties such as linear Dirac-like dispersive bands and the presence of multiple CDW transitions. A distinctive feature was discovered between normal and CDW state which makes this material a potential candidate for studying correlation and topology[87,88]. A unique chiral characteristic was also identified in different CDW states of 1T-TaS_2[89,90], which makes this material, a promising subject for investigating in this research field.

1.4.1.2 Magnetic topological materials:

Over a century ago, Edwin Hall observed a significant phenomenon in ferromagnetic semimetals and metals, known as the anomalous Hall effect (AHE). This effect, characterized by the relationship between Hall resistivity and an applied external magnetic field, was noted to correlate strongly with magnetization. Recent understanding highlights the crucial role of Berry curvature in influencing the AHE in these materials[91,92]. Berry's insights elucidated that energy-level crossings give rise to physical band crossings, akin to magnetic monopoles known as Weyl points. It is noteworthy that magnetic Weyl semimetals are prevalent, with each crossing point in the band structure of a ferromagnetic centrosymmetric compound associated with nodal lines or Weyl points.

The most basic form of topological semimetal, lacking time-reversal or crystalline symmetry, represents the physical embodiment of conventional Weyl fermions. These fermions manifest as two-fold degeneracies emerging when two singly degenerate bands intersect at any point within the Brillouin zone, showcasing linear dispersion away from the point of degeneracy. Notably, Weyl fermions possess a significant topological characteristic known as the Chern number (σ), denoted by $|C| = 1$, evaluated on a sphere surrounding the Weyl point. This Chern number serves as a nontrivial topological invariant, imparting local stability to Weyl nodes against gapping. The Berry curvature, crucial for understanding electronic transport phenomena, concentrates near these Weyl nodes, contributing significantly to the emergence of a large anomalous Hall effect. Few examples are given below.

Anticipated antiferromagnetic topological semimetals have been foreseen based on investigations into large anomalous Hall effects in Mn_3X (X = Sn, Ge, and Ir, Sb) and via direct ab initio calculations in Mn_3Sn and Mn_3Ge featuring kagome layers of Mn atoms[93–95]. The non-collinear magnet Mn_3Sn, emerges as a candidate for magnetic Weyl semimetal, hosting six pairs of Weyl points.

$YbMnBi_2$ is another potential candidate within the 112-pnictide family for Weyl semimetal behaviour. In this compound, the anticipated Weyl nodes are generated through a similar mechanism. Its tetragonal unit cell, comprises a 2D square lattice of Bi atoms, providing a platform for the proposed topological fermions. Experimental data, including Shubnikov–de Haas (SdH) oscillations observed in magneto transport measurements, suggest a low mass for

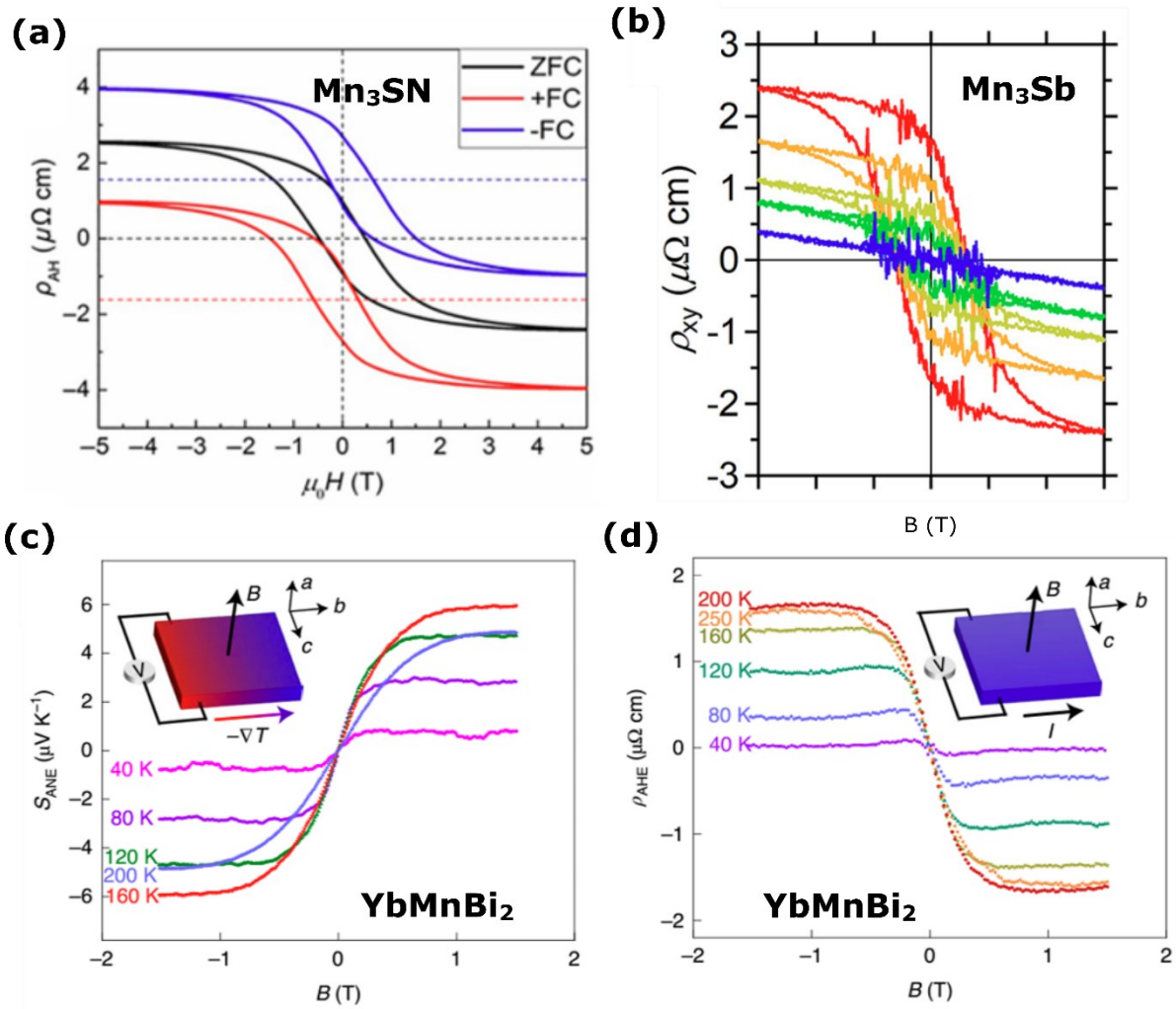

Figure 1.15 ***(a)*** *Anomalous Hall effect (AHE) vs. magnetic field of Mn_3Sn after field cooling (FC) and zero field cooling (ZFC). (adapted from Ref [90])* ***(b)*** *The magnetic field evolution of AHE collected from Mn_3Sb (adapted from Ref [92]).* ***(c)*** *Anomalous Nernst signal vs. magnetic field of $YbMnBi_2$ at different temperature* ***(d)*** *Anomalous Hall resistivity vs. magnetic field of $YbMnBi_2$ at several temperature. (adapted from Ref [93]).*

the charge carriers, aligning with the expectation of Weyl nodes proximate to the Fermi energy. A giant Berry curvature-driven anomalous Nernst effect is detected in $YbMnBi_2$[96] Notably, certain ferromagnetic kagome lattice materials like $Co_3Sn_2S_2$, Fe_3Sn_2, and FeSn exhibit intriguing topological properties. For instance, theoretical predictions for $Co_3Sn_2S_2$ indicate the presence of three pairs of Weyl points under out-of-plane ferromagnetic order, a proposition supported by observations of a giant anomalous Hall effect and angle-resolved photoemission spectroscopy (ARPES) results[85]. Fe_3Sn_2 displays two Dirac cones with a 30-meV gap near the Fermi level. Similarly, in FeSn, a flat band alongside a pair of Dirac bands has been observed[97]. In Eu-122 systems, such as $EuCd_2As_2$, $EuSn_2As_2$, or $EuIn_2As_2$, aside from the antiferromagnetic transition at low temperatures (T_{AF}), significant spin-reorientation (SR) magnetic orders have been detected across a broad temperature range[98–100]. For instance, in

$EuCd_2As_2$, robust spin fluctuations emerge around 100 K, propelling the magnetic Weyl Fermions well beyond the AF transition. Consequently, unconventional anomalous Hall and Nernst effects also manifest above T_{AF}, exhibiting distinct temperature and field behaviours

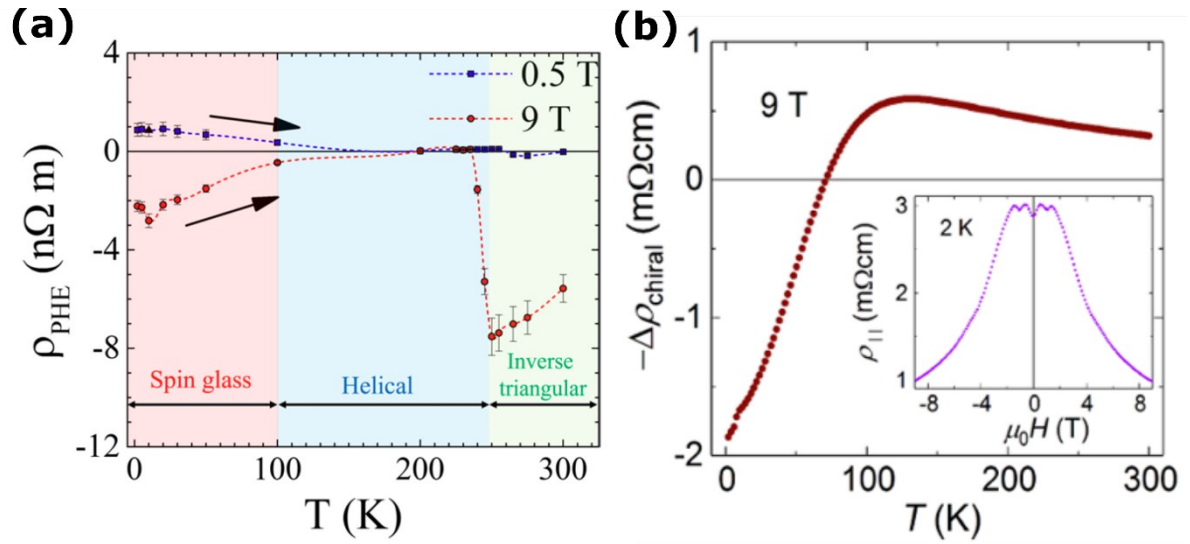

Figure 1.16 ***(a)*** *The temperature dependence of PHE amplitude (at B=9 T, and 0.5 T) of anti-ferromagnetic Mn_3Sn (the color shade is used to show different spin arrangement state) . (adapted from Ref [101])* ***(b)*** *The PHE amplitude ($-\Delta\rho_{chiral}$) at B=9 T vs. temperature (T) of GdPtBi with inset showing chiral anomaly driven NMR data. (adapted from Ref [146])*

compared to those below T_{AF}. In $EuIn_2As_2$, identified as an axion insulator, a magnetic polaron (MP) emerges above T_{AF}, resulting in substantial negative magneto resistivity (MR). Additionally, some studies have reported helical magnetic orders coexisting with A-type AF lattice below T_{AF}, indicating a complex magnetic structure for $EuIn_2As_2$. Moreover, Weyl physics in magnetic Weyl semimetals (MWSMs) is particularly intriguing due to the interplay between magnetism and topological ordering. This interaction gives rise to a plethora of rich and unconventional quantum phenomena, including quantum anomalous Hall (QAH) effects and axion insulators. In MWSMs governed by broken time-reversal symmetry (TRS), the manifestation of Weyl physics, such as chiral anomaly, is notably distinct. Specifically, MWSMs hosting fewer Weyl points (WPs) but with a well-defined helicity, such as chiral Majorana modes, are more favoured compared to MWSMs with a higher WP count, where helicity becomes less well-defined due to the broken Lorentz invariance.

The PHE signal which is assumed to be caused by non-vanishing Berry curvature shows an anomaly with reduction of temperature. Often the anomaly occurs around the spin ordering temperature which indirectly implies the connection between topology and magnetism as also previously observed. Several non-trivial spin textures are probed using the PHE study of Mn_3Sn[101]. The amplitude of the PHE signal shows an anomaly when the system transforms to

different antiferromagnetic state starting from inverse triangular configuration to Helical then finally spin glass state. GdPtBi, for instance, has been proposed as a magnetic field-driven Weyl semimetal. It shows negative MR along with PHE signal driven by chiral anomaly as proposed previously in the literatue[102,103] and the PHE amplitude shows sign reversal which indicates a possible competition between different mechanisms. The PHE signal also shows a kind around the magnetic transition. All these features suggest a possible link between spin ordering and nontrivial band which can be probed through the PHE.

In regards to magnetic topological materials, rare-earth-based magnetic $RAgSb_2$ series become the potential candidates. To explore the field of topological magnetic materials and the interplay between topology and magnetism, we chose $GdAgSb_2$ which is an AFM material from the $RAgSb_2$ series. Previously In this material, powder neutron diffraction study, x-ray resonant exchange scattering measurements, and Mossbauer spectroscopy were conducted and discovered that the moment of Gd atoms is arranged perpendicular to the c-axis anti-ferromagnetically below 13.8 K. Extensive magnetic measurements were performed on this system but electronic transport study on this is rarely conducted. A large and non-saturated MR with anisotropic is discovered in this material which indicates topological properties. The mechanism behind this extraordinary transport in this system is not properly addressed in the literature. In chapter 5, we discussed the material system with details of magneto-transport techniques like TMR, LMR, and PHE. A distinct transport property is discovered below and above T_N. We also conducted a detailed magnetisation study by extracting De Hass Van Alphen oscillation and calculated the effective mass.

1.5 Motivation of the thesis:

Topological materials, distinguished by their unique electronic configurations, provide a platform for unprecedented quantum phenomena and extraordinary behaviours. Within their ordered atomic structures, electrons exhibit intricate patterns dictated by topological properties, leading to phenomena such as the quantum Hall effect and topological insulators. These materials challenge conventional understanding and hold immense potential for transforming fields from electronics to quantum computing. The exploration of topology in condensed matter physics commenced with the revelation of the quantum-Hall effect, demonstrating a profound quantization of Hall coefficients due to the Berry phase. Klaus von Klitzing's pioneering experimental work in unveiling this effect earned him the Nobel Prize in 1985. Subsequently, there has been a surge in both theoretical and experimental efforts to unravel the mysteries of

topological materials. This surge has resulted in the prediction and discovery of numerous topological materials, including 3d topological insulators, Dirac, Weyl, and nodal line semimetals. This exploration extends beyond traditional boundaries to encompass correlated systems, where the interaction between topology and Coulomb forces leads to a plethora of exotic phenomena. The Nobel Prize awarded to Robert B. Laughlin, Horst Störmer, and Daniel Chee Tsui in 1998 for their work on "fractional" quantum hall systems marks a significant milestone in understanding the role of topology in interacting systems. Subsequent extensive theoretical and experimental investigations have been conducted in the research area of topological and correlated materials. The intricate interplay between topology and phenomena such as magnetism or CDW often results in the emergence of exotic phases such as the axion insulator. For instance, electronic interaction-driven charge-density waves can be observed in materials like the Weyl semimetal $(TaSe_4)_2I$, where the CDW induces the axion insulator phase. The antiferromagnetic $MnBi_2Te_4$ has also been extensively studied due to its combination of topology and magnetism, hosting a non-trivial axion insulator phase. Other examples of topologically correlated materials include topological Kondo insulators, topological Mott insulators, and alterations in topological classification. The influence of electron correlation on topological states presents a particularly intriguing avenue, with the potential to fundamentally alter ground state properties. Consequently, the relationship between Coulomb forces and topology stands as a central focus in condensed matter physics, providing vital insights into a diverse array of materials. This dissertation will delve into specific cases, utilizing real material examples to investigate the intricate interplay between charge/spin ordering and topological phases. Our focus will be on $LaAgSb_2$ and 1T-TaS_2, where complex charge ordering occurs through CDW formation, and the potential antiferromagnetic non-trivial semimetal $GdAgSb_2$, to explore the realm of topological correlated systems. Lanthanum-based $LaAgSb_2$ from the square net series has been rigorously studied for decades due to its exotic properties such as linear Dirac-like dispersive bands, CDWs, and superconductivity. Notably, distinct phenomena like linear and quadratic transverse magnetoresistance are observed below and above CDWs, respectively. This discovery underscores the need for a thorough exploration of the impact of CDWs on the material's topological properties.

To further proceed to show a possible connection between topology and correlation, we select a particularly fascinating and widely investigated quasi-2d CDW system, 1T-TaS_2, in which external tuning factors like temperature, pressure, or chemical substitution span an extremely complicated electronic phase diagram. This remarkable phase diagram also shows pressure-induced superconductivity and a phase known as the Mott phase in addition to multiple charge

density waves. Apart from that, a many-body collective phenomenon in condensed matter known as the chiral charge density wave which is observed in 1T 1T-TaS_2 may have implications for topological physics and unconventional superconductivity. This motivates us to study the relationship between CDW ordering and non-trivial electronic bands in this system. The electrostatic interaction between electrons respecting the Pauli exclusion principle gives rise to magnetism. To further enrich the field of interaction and topology, we also investigate the complex connection between magnetism and topology in this thesis by studying an antiferromagnetic $GdAgSb_2$ from the rare-earth-based square net $RAgSb_2$ series. In this material series previously people discovered linear dispersion, AFM, and CDW, heavy Fermion which indicates that $GdAgSb_2$ may be a possible magnetic topological system.

1.6 Organization of the thesis:

The entire thesis has been divided into six chapters and one appendix. The overview of different chapters is given below:

In the chapter 1, the concept of topology in generic sense as well as in the context of condensed matter physics has been introduced. Starting for the observation of quantum Hall effect, the journey of topological idea in condensed matter physics is presented. We have introduced the non-trivial topological materials exhibiting QSHE, QAHE, 3d TIs, 3d Dirac and Weyl semimetal, along with their experimental observations. Then we bring in the idea of electronic correlation. In this context, the concept of charge density waves is discussed, being relevant for the thesis. After a brief introduction to different magnetic systems, we discuss the work related to the coexistence and interplay of CDW, topology and magnetism are presented. $LaAgSb_2$ and 1T-TaS_2 as CDW systems and $GdAgSb_2$ as a magnetic system are chosen to explore the research idea of topological and correlated system. This thesis describes how the Charge ordering and magnetic ordering coexist with the topological properties and affect the topological properties.

In the chapter 2 contains details about the experimental techniques that is employed for understanding the effect of Berry curvature on the transport properties. Furthermore, the working principle of the characterization techniques are discussed here.

In the chapter 3, we focused on the $LaAgSb_2$ which is a square-net CDW Dirac system. We investigated the effect of CDW in the system by performing the magnetic field dependent electronic transport below and above T_{CDWs}. A sign change in the amplitude of the PHE signal below CDW is observed. The transverse magnetoresistance is quadratic in normal phase, but a

linear MR is found inside CDW state, along with a distinct feature in the in-plane angular MR. The PHE signal increases quasi-linearly with magnetic field. We also present the temperature evolution of the ordinary Hall coefficient which shows anomaly around the phase transition. With the help of electronic band structure, we demonstrated that this unusual finding might be attributed to the transformation from a normal semi-Dirac system to a tilted Weyl semimetal driven by the chiral charge density wave (CDW), as finite Berry curvature is detected within the CDW state.

In the chapter 4, To dig deeper into topology and CDW, we turned our attention to studying 1T-TaS_2, a classic CDW system. We used two types of Hall effect experiments, called non-linear Hall effect (NLHE) and planar Hall effect (PHE), to look at how charge ordering affects the material's topological properties. Our findings showed that there were measurable NLHE and PHE signals only within the fully commensurate CDW (C-CDW) state, suggesting that this state has non-trivial topological characteristics. Additionally, we ran theoretical calculations to determine the Berry curvature dipole (BCD) within the C-CDW state. We also investigated any changes to the Fermi surface by conducting ordinary Hall effect and Seebeck measurements.

In the chapter 5, we looked at how spin ordering, which is affected by exchange interaction, impacts the topological properties, along with electronic interaction which is discussed in the previous chapter. To explore this research direction, we performed details magnetotransport studies on square-net antiferromagnetic $GdAgSb_2$. A low effective mass is calculated from the De-Haas Van Alphen data of magnetization. The similar PHE signal like several topological material has also been discovered in this system. A distinct nature of PHE above and below Neel temperature is found with a kink around the Neel temperature which suggest the possible effect of magnetism on the topological feature. The possible semimetallic nature also been demonstrated through two band fitting of the ordinary Hall and magnetoresistance data. Overall, in this chapter we have tried to show the effect of magnetism on the topological properties though magnetization, magnetotransport studies, PHE, and in-plane angular magnetoresistance.

In the chapter 6, we present the conclusion of the thesis and the future scope in the research direction of topology and correlation in the condensed matter physics.

In the appendix, we have presented the noise spectroscopic study of chemical vapour deposited(CVD) graphene based field effect transistor.

Chapter 2

Experimental techniques:

This chapter provides an overview of the experimental methods used in this thesis. The first section describes Physical property measurement set-up (PPMS) based magneto-transport like Magnetoresistance, Hall effect, Planar Hall effect etc. Next, we explain the working principle of instrument which is used for characterize the materials. After that, we describe home-built electronic transport setups, which include low-temperature cryogenic insert development, noise spectroscopy techniques, and non-linear Hall techniques.

2.1 Magneto transport:

The Physical property measurement set-up (PPMS), as depicted in **Figure 2.1a**, stands as a remarkably versatile measurement platform, offering not only turn-key functionality but also customizable features, is used for measuring the magneto -transport properties. The result is a conducive, low-vibration environment conducive to the precise measurement of samples, marking a significant advancement in experimental accuracy and reliability.

There is a sample chamber at the bottom of the PPMS. We can put the "puck" (**Figure 2.1a**) into the sample chamber using the puck inserting tool. The puck has 12 sockets at the bottom, which connect to the outbox of the PPMS when the puck is put in place. We can put the sample on top of the puck.

2.1.1 Hall effect:

Edwin H. Hall introduced the classical Hall effect in 1979, delineating the trajectory of a charged particle subjected to a magnetic field. Consider a scenario where electrons are constrained to move exclusively along the x-y plane. When a persistent current(I) flow along the x-direction, and a magnetic field(B) is applied perpendicular to this current (in the z-direction), the charge carriers undergo the influence of the Lorentz force. Consequently, the electrons deviate from their original path, leading to the accumulation of opposite charges at the corresponding boundaries of the sample. This charge accumulation engenders an internal electric field.

When the electric force reaches a magnitude sufficient to counterbalance the Lorentz force imposed by the applied magnetic field, electrons can traverse from the upper edge to the lower

edge of the material. This migration results in a voltage difference between the two edges of the sample, denoted as Hall voltage (V_H).

In a state of equilibrium, the Lorentz force is expressed as:

$$\mathbf{F} = q(\mathbf{E} + \mathbf{v} \times \mathbf{B}) = 0 \quad \ldots\ldots\ldots 2.1$$

Here, v represents the particle's velocity, and q is the charge of the particle. If t denotes the thickness of the sample, the Hall voltage V_H) and Hall resistance (R_h) between two boundaries can be expressed as:

$$V_H = \frac{IB}{nte} = R_h \times I \quad \ldots\ldots\ldots 2.2$$

In this equation, R_h signifies the Hall resistance, n denotes carrier density and I is the current coursing through the sample. This formulation implies a linear dependence of Hall resistance on the applied magnetic field. When a magnetic field is present, the charged particle follows a circular path with a cyclotron frequency (ω_c) given by, ω_c=eB/m. Here, e = 1.6×10^{-19} C, B represents the strength of the magnetic field, and m is the mass of an electron.

2.1.2 Magnetoresistance:

The magnetoresistance arises from the diversion of electrons from the direction of the electric field due to the Lorentz force, leading to an increase in resistivity with a concurrent rise in the magnetic field. This effect is usually small at low magnetic fields but can become much larger at high fields. In classical OMR theory, OMR is always positive and proportional to the square of the magnetic field when the product of the cyclotron frequency (ω_c) and the relaxation time (τ) is very small and constant when $\omega_c\tau \gg 1$. For stoichiometric semiconductors, where the number of electrons equals the number of holes, OMR behaves differently. The relationship is given by:

$$\mathrm{MR} \propto \mathrm{B}^2(\omega_c\tau \ll 1) \quad \ldots\ldots\ldots 2.3$$

$$\mathrm{MR} \propto c\mathrm{onst}\,(\omega_c\tau \gg 1), \mathrm{n} \neq p \quad \ldots\ldots\ldots 2.4$$

In the classical Hall effect, when there's a vertical magnetic field (B), a current flowing lengthwise creates a Hall voltage (V_{xy}) perpendicular to the current direction. In regular systems with just one type of charge carrier (either electrons or holes), this Hall voltage creates an electric field that balances out the Lorentz force, allowing the carriers to keep moving straight ahead. In semimetals, however, both electrons and holes move sideways in the same direction. This cancels out V_{xy}, making it zero or very small. So, the carriers are always pushed sideways by the Lorentz force. Subsequently, under a small B, this sideways push with open

orbits causes a giant magnetoresistance (GMR) that increases quadratically with the magnetic field in semimetals like WTe_2 [104]. Positive magnetoresistance (MR) typically manifests in metals, semiconductors, and semimetals, whereas negative MR is observed in magnetic materials. MR, in most nonmagnetic compounds, is a relatively feeble phenomenon. It is delineated by quadratic field dependence in low fields, reaching a saturation point with a magnitude of a few percent in the case of metals [42,105].

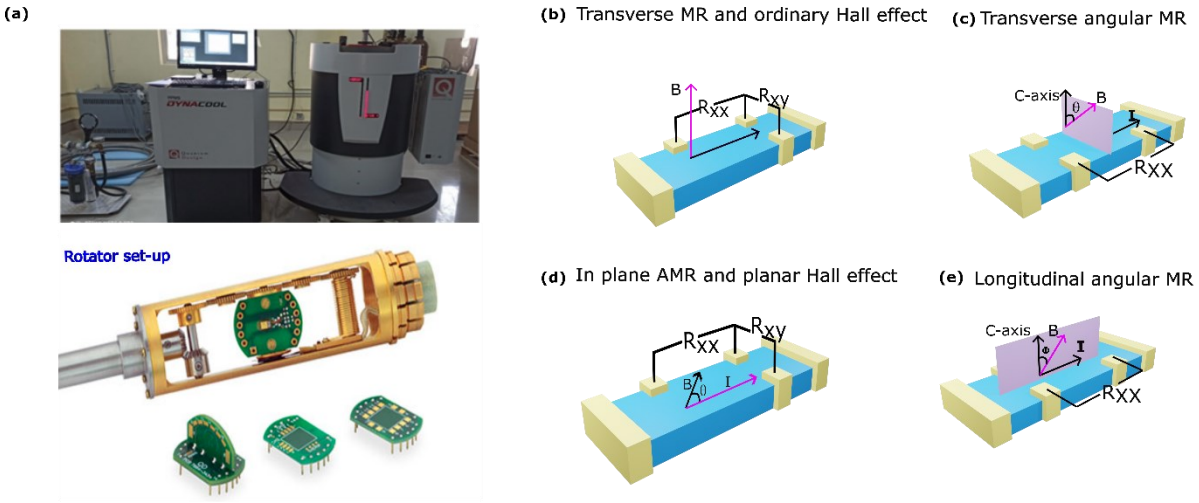

Figure 2.1 (a) *The photographic image of PPMS set-up(top) and the rotators set-up(bottom).* ***(b)*** *Transverse MR and ordinary Hall effect set-up* ***(c)*** *Transverse angular MR* ***(d)*** *In-plane AMR and planar Hall effect.* ***(e)*** *Longitudinal angular MR.*

A **linear magnetoresistance** is frequently observed in topological quantum materials, including topological insulators (TIs) and Dirac and Weyl semimetals. This observation is quite unusual as the "classical" magnetoresistance (MR) observed in most metals and semiconductors depends quadratically on the magnetic field ($MR_{xx} \propto B^2$), it is reasonable to speculate that LMR may be linked to the unique electronic band structure of topological materials, such as the linear band dispersion near Dirac points.

The **linear magnetoresistance** might be caused by several reasons like charge-inhomogeneity theory where it is caused due to interorbit transfer of carriers mediated by fluctuation of charge carrier or by disorder[106]. According to the Abrikosov's theory[107], **linear magnetoresistance** might arise because of a Dirac-like linear dispersive band. Abrikosov's idea suggests that the probability of transferring electrons in a certain direction, known as the longitudinal transfer probability, depends on the magnetic field **B**. In materials with Dirac-like linear dispersion, the way electric charges screen each other, represented by the Thomas–Fermi screening wave vector (or reciprocal Debye screening radius), changes with the magnetic field. Conversely, in

regular materials with a different electron dispersion pattern, this screening wave vector remains constant regardless of the magnetic field. Further studies on topological materials suggested that the linear non-saturated magnetoresistance might arise due to non-vanishing Berry curvature[11,56].

2.1.3 Planar Hall effect:

The Planar Hall Effect (PHE)[102,103] is a phenomenon in which the external magnetic field is oriented within the plane defined by the Hall electrodes, distinguishing it from other Hall effects where the magnetic field is perpendicular to this plane. PHE is primarily a consequence of the anisotropic magnetoresistance (AMR), which manifests itself in both parallel and perpendicular orientations relative to the in-plane rotational magnetic field (B) (see **Figure 2.1d** for the experimental set-up). The characterization of PHE involves the measurement of longitudinal and transverse resistances (R_{xx} and R_{yx}^{PHE}). The emergence of PHE can be attributed to various factors, including intrinsic magnetism, topological properties, and the anisotropic Fermi surface of the material under investigation[45,108–112]. The interaction of these factors with the in-plane rotational magnetic field leads to distinctive changes in resistances, providing a means to explore and identify the underlying physics of different quantum materials. By analysing the behaviours of R_{xx} and R_{yx}^{PHE} in response to the magnetic field, one can gain valuable insights into the unique properties and characteristics of materials exhibiting

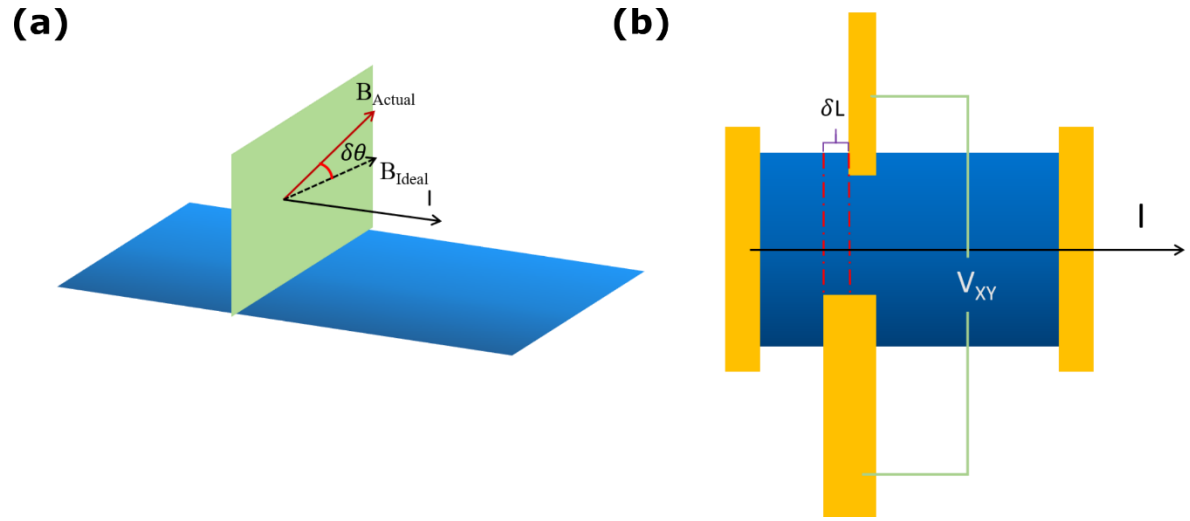

Figure 2.2 (a) *The error due to the misalignment due to tilt of the crystal plane from the planar magnetic field. (b) The error due to the misalignment of the Hall electrode.*

the Planar Hall Effect. In general, the angular dependence of PHE signal follows the Eq. 2.3 and the **Figure 2.3c** shows the typical angular dependence of the PHE.

$$\rho_{xy}^{PHE} = -\Delta\rho^{PHE} \operatorname{Sin}\theta \operatorname{Cos}\theta \ , \qquad \ldots\ldots\ldots \qquad 2.5$$

$$\text{where } \Delta\rho^{PHE} = \rho_{||} - \rho_{\perp}$$

$$\rho_{xx}^{\text{IN-plane AMR}} = \rho_{\perp} - \Delta\rho^{PHE} \operatorname{Cos}^2\theta \qquad \ldots\ldots\ldots \qquad 2.6$$

To obtain the actual planar Hall signal, two potential errors typically arise, primarily due to the misalignment of the crystal plane with the magnetic field and misalignment in the Hall

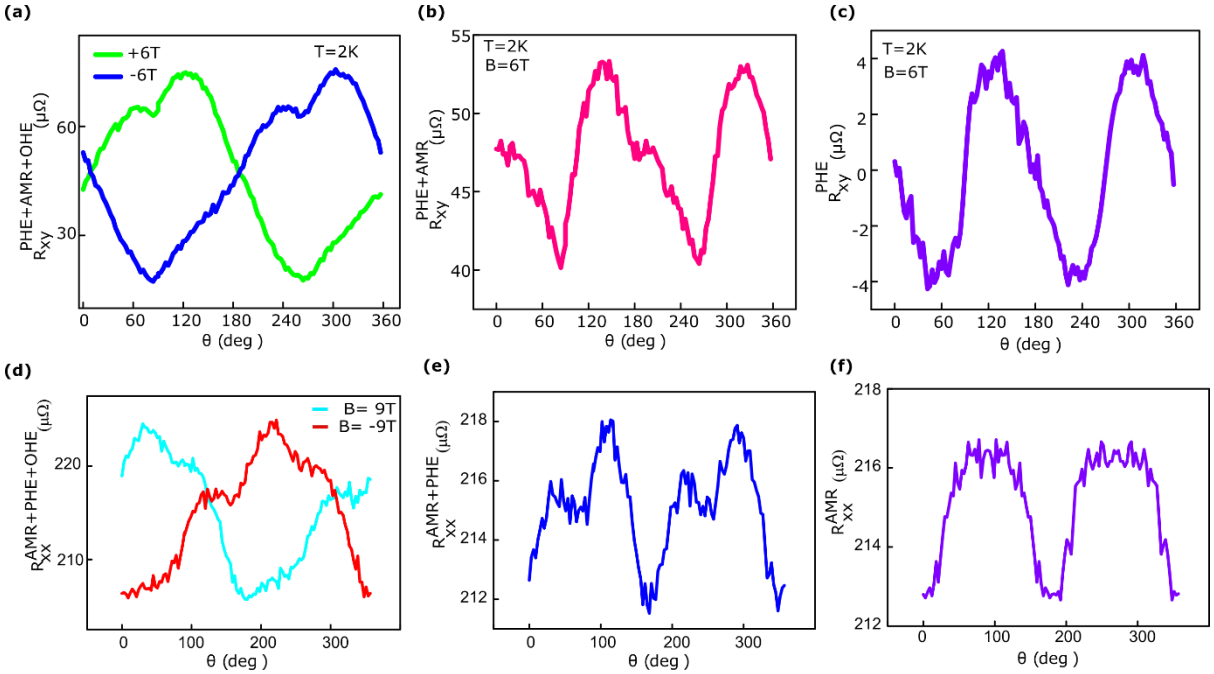

Figure 2.3: (a). *$R_{xy}^{PHE+AMR+OHE}(+6T)$ and $R_{xy}^{PHE+AMR+OHE}(-6T)$ vs. θ at T=2K.* ***(b).*** *$R_{xy}^{PHE+AMR}(+6T)$ vs. θ at T=2K after removing the out of plane Hall components by following the* ***Eq. 2.7.*** ***(c).*** *$R_{xy}^{PHE}(+6T)$ vs. θ at T=2K after removing the angular MR part by following the* ***Eq. 2.8a.*** ***(d)*** *$R_{xy}^{PHE+AMR+OHE}(+9T)$ and $R_{xy}^{PHE+AMR+OHE}(-9T)$ vs. θ at T=2K. $R_{xy}^{PHE+AMR}(+6T)$ vs. θ at T=2K after removing the out of plane Hall components by following the* ***Eq. 2.7.*** ***). (f)*** *$R_{xy}^{AMR}(+9T)$ vs. θ at T=2K after removing the angular MR part by following the* ***Eq. 2.8b.***

electrodes, as schematically shown in **Figure 2.2a** and **2.2b**, respectively. The following two equations can be employed to get rid of the errors.

$$R_{xy}^{PHE+AMR} = \frac{[R_{xy}^{PHE+AMR+OHE}(B,\theta) + R_{xy}^{PHE+AMR+OHE}(-B,\theta)]}{2} \qquad \ldots\ldots\ldots \qquad 2.7$$

$$R_{xy}^{PHE} = \frac{\left(R_{xy}^{PHE+AMR}(\theta) - R_{xy}^{PHE+AMR}(\pi-\theta)\right)}{2} \qquad \ldots\ldots\ldots \qquad 2.8a$$

$$R_{xy}^{AMR} = \frac{\left(R_{xy}^{PHE+AMR}(\theta) + R_{xy}^{PHE+AMR}(\pi-\theta)\right)}{2} \qquad \ldots\ldots\ldots \qquad 2.8b$$

Figure 2.3a shows the raw data for + 6 T and - 6T. **Figure 2.3b** demonstrate the corrected signal after averaging the signal at B = 6 T and B = - 6 T. The actual PHE signal can be obtained after correcting the signal further using Eq. 2.8a (see **Figure 2.3c**). Subsequently, for topological materials, the angular dependence of In-plane AMR can also be extracted using Eq. 2.8b (see **Figure 2.3(d-f)**).

2.2 Magnetization

2.2.1 Vibrating-sample magnetometer (VSM):

VSM is also known as a Foner magnetometer, serves as a scientific apparatus designed to gauge magnetic characteristics by relying on Faraday's Law of Induction. MIT Lincoln Laboratory's Simon Foner conceived the VSM in 1955, disclosing his invention in 1959. Additionally, G.W. Van Oosterhout and P.J. Flanders made references to it in 1956. The initial step involves placing a sample within a consistent magnetic field. If the sample possesses magnetic qualities, it aligns its magnetization with the external field.

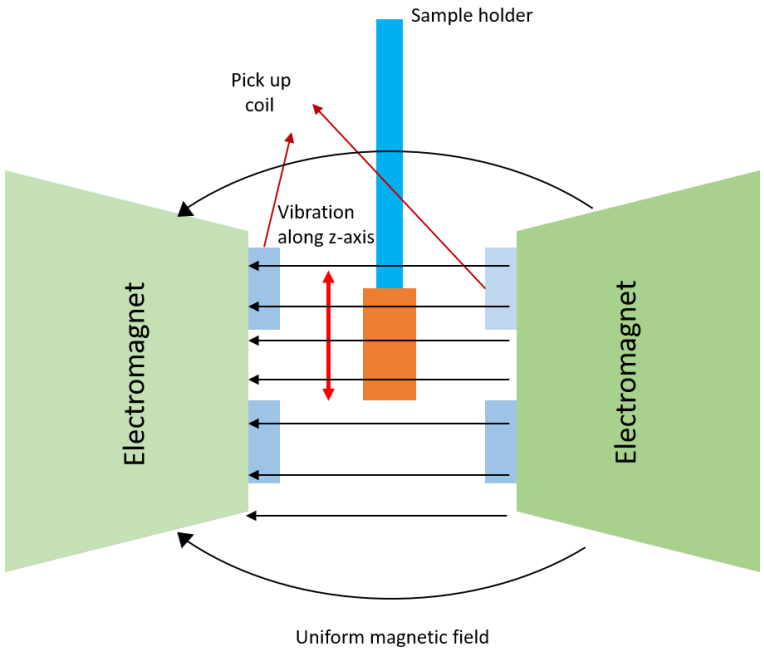

***Figure 2.4**: Schematic of a VSM set-up*

The magnetic dipole moment of the sample generates a magnetic field that changes over time as the sample moves vertically. This movement is typically facilitated using a piezoelectric material. The oscillating magnetic field induces an electric field in the VSM's pickup coils.

Consequently, the current generated is proportionate to the sample's magnetization—higher induced current corresponds to greater magnetization. Consequently, a hysteresis curve is typically recorded, allowing deduction of the magnetic properties of the sample.

One can have an intuitive idea about the ordering of spin moments of different kinds of magnetic systems through magnetization measurement. Magnetization data is crucial for understanding and characterizing the complex behaviours in ferromagnetic, antiferromagnetic, and spin glass superconductors. In ferromagnets, magnetization measurements reveal how magnetic domains align, indicating the material's response to external magnetic fields and temperature changes. For antiferromagnets, magnetization data helps identify the arrangement of opposite spins and their influence on the material's magnetic properties. In spin glass systems, which exhibit disordered magnetic states, magnetization measurements uncover the random freezing of spins and the resulting magnetic frustration. Overall, magnetization data provides insights into the interactions and transitions within these materials, aiding in the development and optimization of advanced magnetic and superconducting technologies. It also helps to characterize the superconductor through observing the Meissner effect. When it enters a zero-resistance state, characterized by perfect diamagnetic screening and an abrupt decrease in susceptibility. In the superconducting state, the volume susceptibility is exactly -1 in SI units or $-1/4\pi$ in cgs units[113].

Magnetization measurements in presence of magnetic field can also be used to probe the Fermi surface of a material. The oscillatory fluctuation known as the de Haas-van Alphen (dHvA) effect manifests as a periodic alteration in the diamagnetic susceptibility concerning the strength of a magnetic field (B). This approach provides detail insights into the extremal areas of a Fermi surface. The inaugural detection of this phenomenon dates to 1930 when de Haas and van Alphen conducted experiments. Their investigation centred on the magnetization (M) of semimetal bismuth (Bi) at 14.2 K, charting its dependence on the magnetic field (B) in elevated fields[**114**]. The findings revealed a periodicity in the magnetic susceptibility M/B relative to the reciprocal of the magnetic field (1/B). Notably, this occurrence exclusively materializes under conditions of low temperatures and large magnetic fields. Analogous oscillatory tendencies have also been identified in magnetoresistance, recognized as the Shubnikov-de Haas effect.[114,115]

2.3 Scanning tunnelling microscopy (SEM)

It serves as a potent instrument in material science. It employs a high-energy electron beam

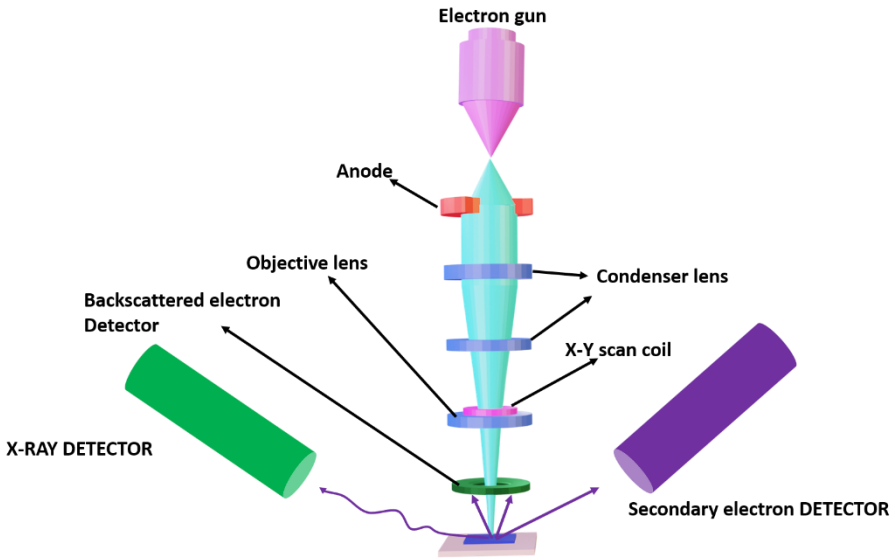

Figure 2.4: *The schematic diagram of* Scanning tunnelling *microscopy*

directed through a sample, enabling observation of its crystal structure, morphology, and elemental composition. SEM facilitates examination of crystal grain boundaries, structural dislocations, and material defects, as well as the analysis of the quantity, size, and shape of low-dimensional entities such as quantum dots, nanosheets, and nanowires.

Electron beams emit from the source of the column in the electron gun and gain speed as they traverse through the column under a set accelerating voltage (1 keV – 30 keV). Components such as condenser lenses and apertures work to diminish the beam's width. The ultimate lens within the column, the objective lens, concentrates the beam onto the surface of the sample. Beam diameters in an SEM vary greatly, ranging from less than 1 nanometer to 20 nanometers, contingent on the electron gun type, accelerating voltage, and lens setup.

Samples are affixed onto a stage within the chamber, with both the column and chamber maintained in a vacuum through a combination of pumps. The degree of vacuum relies on the microscope's design. Certain microscopes facilitate adjustable pumping, permitting the sample chamber to sustain a lower vacuum than the remainder of the column to facilitate low-vacuum imaging. The electron beam's position on the sample is regulated by scan coils positioned above the objective lens. These coils enable the beam to traverse the surface of the sample in the X-Y plane. Once scanned, the beam interacts with the sample, producing various signals such as

secondary electrons, backscattered electrons, and characteristic X-rays. These signals are subsequently detected by suitable detectors (as shown **in Figure 2.4**).

A scan generator, in conjunction with an external computer equipped with specialized software, synchronizes the data from the scan generator (containing the beam's X,Y position at each time period) with the intensity recorded by the detector. This synchronization allows for the real-time display and examination of a grayscale image, pixel by pixel. Adjusting the dwell time of the electron beam at each X,Y position can modulate the signal-to-noise ratio. Additionally, magnification is determined by the size of the scanned area, with higher magnifications corresponding to progressively smaller scanned areas. The number of pixels within a given scan area can also be adjusted, affecting the apparent resolution.

2.4 X-ray diffraction (XRD):

The X-ray diffraction (XRD) method, a non-invasive approach, is utilized for probing the atomic arrangement within crystalline materials. By directing a beam of X-rays onto the specimen, which then undergoes diffraction by its atomic planes, one can ascertain details such as crystallite dimensions, structural imperfections, and phase composition. Through analysis of the angles and strengths of these diffracted beams, a wealth of information regarding the atomic structure, crystallinity, and thickness of films can be obtained, encompassing factors like

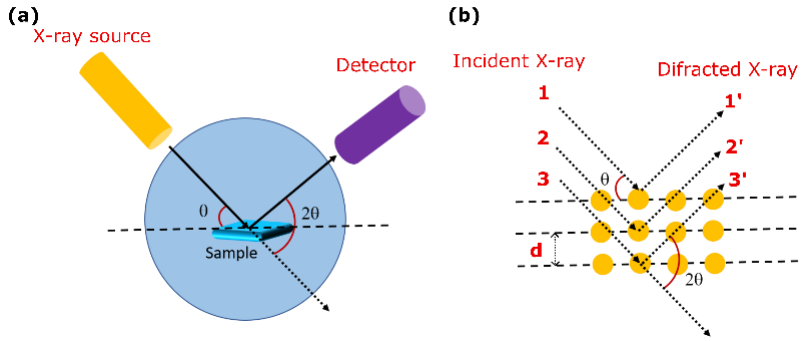

Figure 2.5: *Schematic diagram of (a) X-ray diffractometer and (b) X-ray diffraction*

strain, orientations, and defects. In Chapter 2, section 2.4, a depiction of the XRD technique is given. The apparatus comprises an X-ray tube as the radiation source, optical components guiding the incident beam, and a goniometer supporting the sample stage and detector. The crystal lattice, behaving akin to a periodic array of atoms, exhibits elastic scattering of

electromagnetic waves, including X-rays. These scattered waves interfere constructively under specific conditions dictated by Bragg's law, expressed as:

$$2dsin(\theta)=n\lambda \quad \ldots\ldots\ldots\ldots\ldots \quad 2.9$$

Here, d represents the spacing between atomic planes, θ denotes the incident angle, n signifies any integer, and λ stands for the wavelength of the X-ray beam. Consequently, diffraction patterns manifest solely at incidence angles corresponding to the lattice structure's spacing d. Notably, diffraction arises only when Bragg's law is satisfied, facilitating constructive interference between X-rays and atomic planes, with observations including both the intensities and angles of the reflected beams relative to the incident direction (2θ).

2.5 Electronic transport:

2.5.1 Low-temperature electronic transport set-up:

A cryogenic apparatus of utmost importance for executing precise electrical transport experiments is the variable temperature insert. In the pursuit of this objective, we have designed a dipstick, whose intricate design is illustrated in Figure 2.13. This specialized probe encompasses several integral elements, notably a sample holder firmly attached to a copper plate, a primary stainless-steel tube facilitating wire connections, and four smaller diameter stainless steel tubes, serving a dual purpose by accommodating connections for the heater wire and housing the conduit for gas purging. Additionally, a vacuum jacket has been incorporated into the design to effectively shield the primary samples to avoid sudden cooling in liquid nitrogen environment. Also, establishment of a vacuum (~ 10^{-4} - 10^{-6} mbar) within the chamber is necessary to ensure a gradual and precisely controlled cooling mechanism for our specimen. The dipstick integrates a 25ohm manganin heater wire (see **Figure 2.6**), facilitating precise control over the temperature of the sample stage. Complementarily, a PT100 temperature sensor is strategically positioned near the sample holder, enabling accurate real-time monitoring of the sample temperature. The wires emanating from the room temperature source are intricately wound around the copper stage for efficient thermalization with the bath. The temperature is controlled by tuning the heater power using temperature controller (Lakeshore,

Model 340). The finely tuned PID parameters of the temperature controller yield an exceptional

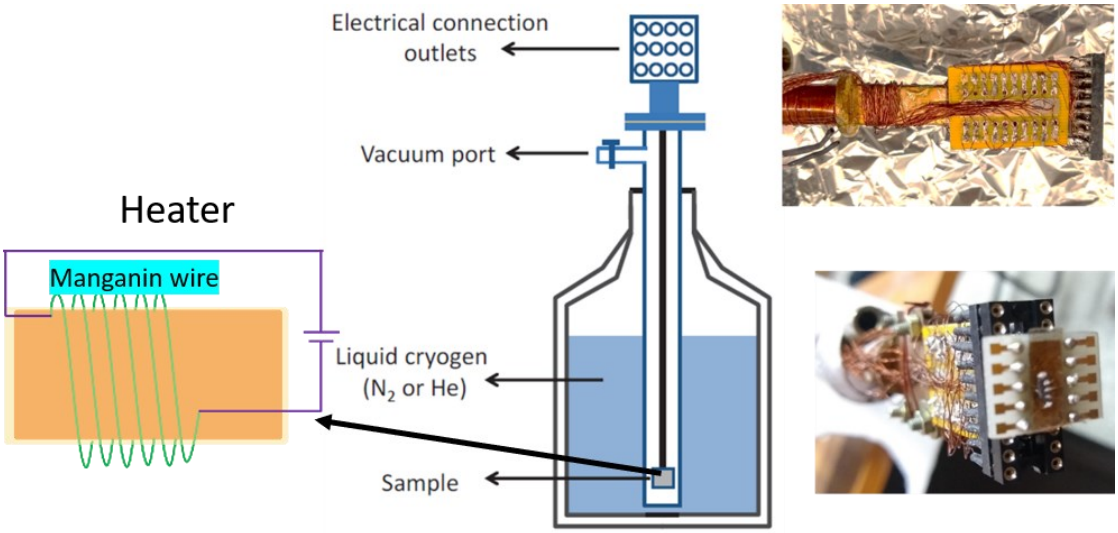

Figure 2.6: *Schematic of the dipstick inside the Nitrogen Dewar (left) with the black arrow showing the heater made of manganin wire. Image of the sample holder of the dipstick (right side).*

temperature stability at the sample stage within few milli Kelvin accuracy. For connecting the sample wires to the instruments, we employ BNC cables, which are then affixed to a breakout box. To ensure that our sample never remains floating, we implement a three-way switch and establish connections. This configuration ensures that the sample is either grounded or set to the desired voltage level for the experiment. LabVIEW based programmes are developed to perform the measurements.

2.5.2 Non-linear Hall effect:

An additional captivating experimental approach that can be utilized for discerning the characteristics of non-trivial electronic bands involves the utilization of the non-linear Hall effect. Hall effects fall short in exploring the complex geometric traits of Bloch states in materials that obey time-reversal invariance while breaking inversion symmetry. A recent breakthrough unveils a crucial nuance. The prior assertion holds true only within the linear response regime, where Hall voltages exhibit linear proportionality to the external electric field. The narrative shifts when nonlinear Hall currents, with a quadratic relationship to the external electric field, manifest even under time-reversal symmetric conditions. The genesis of this nonlinear phenomenon links to an intrinsic contribution tied to a concept akin to the dipole moment of the Berry curvature, called the Berry curvature dipole (BCD). Topological materials characterized by an asymmetric distribution of Berry curvature in momentum space manifest this distinctive non-linear Hall effect. Substantial BCD manifests within the system, akin to the inclined Type I or II Weyl cones and the system with massive tilted Dirac cone.

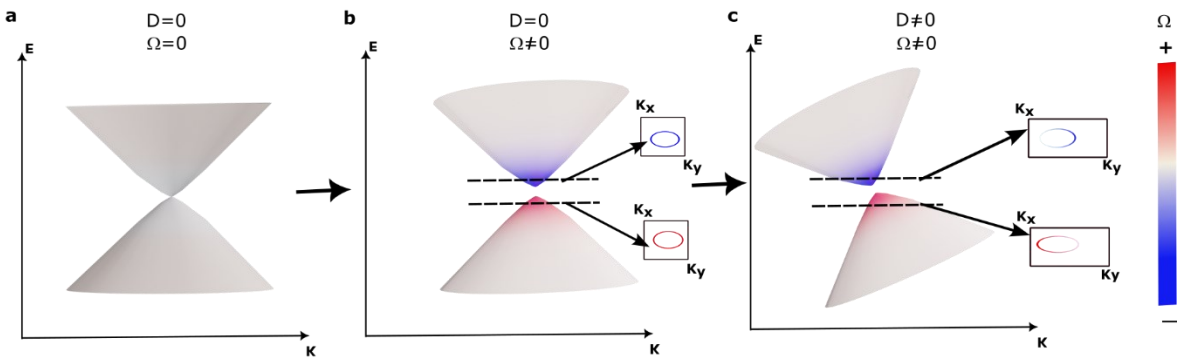

Figure 2.7 (a) *The schematic of a massless inversion symmetric Dirac cone with Zero Berry curvature (BC)* ***(b)*** *By breaking inversion symmetry, opening an energy gap at the Dirac point results in significant BC (Ω) close to the edge of the bands (see color bar). But the distribution is uniform at any Fermi level (dashed line)* ***(c)*** *The states at the Fermi level can have different Berry curvatures and anisotropic Fermi velocity(* $\frac{\partial \varepsilon}{\partial k^{\alpha}}$*) by tilting the Dirac cone, which results in non-zero Berry curvature Dipole (D).*

A massless Dirac fermion (found in graphene) has no Berry curvature (Ω) to begin with (**Figure 2.7a**). Breaking inversion symmetry to create an energy gap near the Dirac point, as in the case of gapped graphene) results in a significant Berry curvature close to the gap (**Figure 2.7b**). But still, the BCD is zero as the BC is uniform at the Fermi level. As depicted in **Figure 2.7c,** the tilted Dirac cone near each hot spot makes the distribution of BC to be non-uniform, resulting in a finite BC dipole at the Fermi level.

$$\mathrm{BCD} = -\frac{1}{\hbar}\int \delta(\varepsilon - \varepsilon_F)\frac{\partial \varepsilon}{\delta \mathrm{k}_{\alpha}}\Omega(\mathrm{k})\, d^2\mathrm{k} \qquad \ldots\ldots\ldots 2.10$$

where is the energy is denoted by ε, k is the crystal momentum wavevector, ε_F presents the chemical potential and $\partial\varepsilon/\partial \mathrm{k}_{\alpha}$ is the group velocity along α. For a gapless Dirac cone, the Berry curvature is zero, so BCD is also vanished. But for non-tilted gapped Dirac cone, BC is constant. However, the group velocity $\partial\varepsilon/\partial \mathrm{k}_{\alpha}$ have equal but opposite value on the opposite sides of the Fermi surface, so the integral is zero. The Berry curvature and group velocity acquire different value because of the tilted Dirac cone which induces a finite BCD in the system with tilted gapped Dirac cone (**Figure 2.7c**).

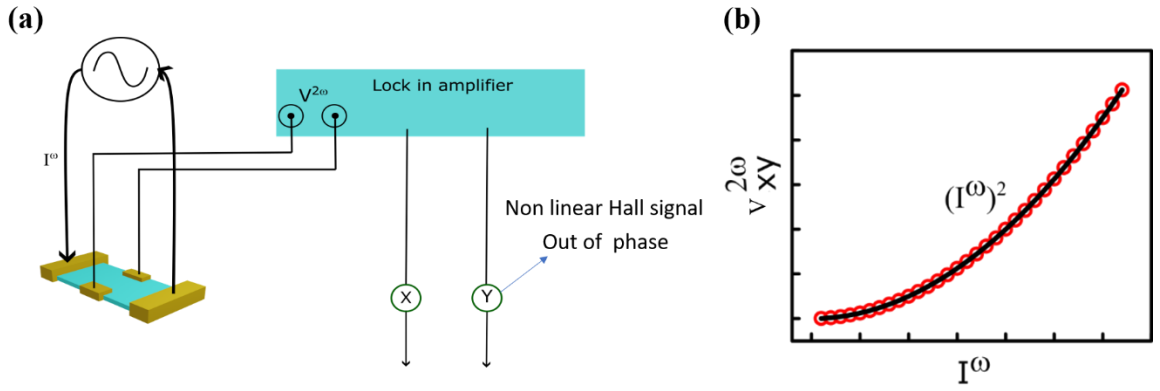

Figure 2.8 (***a***) *The illustration of the second harmonic Hall voltage (NLHE) measurement set-up based upon lock in amplifier* (***b***) *The typical curve of* $V_{xy}^{2\omega}$ *vs.* I^{ω}.

For observing the second-order conduction one has to use $j_{\alpha}^{2\omega} = \chi_{\alpha\beta\beta} E_{\beta} E_{\beta}$. As we measure the voltage difference, so we need to transform the current into electric field. See the following equation:

$$E_{\alpha}^{2\omega} = \frac{\chi_{\alpha\beta\beta}}{\sigma} E_{\beta} E_{\beta} = \frac{\chi_{\alpha\beta\beta}}{\sigma} E_{\beta 0} E_{\beta 0} \sin^2(2\omega t) = \frac{\chi_{\alpha\beta\beta}}{2\sigma} E_{\beta 0} E_{\beta 0} \left[1 - \sin\left(2\omega t + \frac{\pi}{2}\right)\right] \quad \text{.....2.11}$$

In the nonlinear measurement, we detect the voltage at the second frequency 2ω using lock in amplifier with a phase shift of $+\pi/2$(out of phase componenet of lock in amplifier). The experimental technique to detect the nonlinear Hall signal is schematically shown in **Figure 2.8a**. The typical nature of the IV plot is shown in **Figure 2.8b**.

2.5.3 Thermo-electric effect

The phenomenon known as the Seebeck effect involves the creation of an electromotive force (EMF) across two distinct points within a conductor experiencing a variance in temperature. This EMF is specifically referred to as the Seebeck EMF, or alternatively, the thermoelectric EMF. The relationship between this EMF and the temperature difference is quantified by the Seebeck coefficient. In the context of measurement, a thermocouple evaluates the potential difference between the hot and cold ends of dissimilar materials. The magnitude of this potential difference corresponds directly to the temperature difference between the ends. Initially identified in 1794 by the Italian scientist Alessandro Volta, this phenomenon bears the name of the Baltic German physicist Thomas Johann Seebeck, who independently rediscovered it in 1821[116].

Copper blocks are used as a heat source and heat sink, as mentioned in **Figure 2.9a** . cigarette rolling papers (Odet-Cascadec-Bolloré (OCB)) is attached to the copper block with the help of two-component epoxy glue (Stycast 2850 FT with catalyst 9) to electrically isolate but

thermally coupled to the Cu block. The sample is then thermally anchored with cigarette rolling papers paper using silver paste. Furthermore, the silver paste is used as an electrode on the sample. The whole system is mounted in a vacuum-sealed homemade cryogenic insert. The Seeback voltages are acquired using a Keithley 2182A nanovoltmeter. The temperature controller, Lakeshore-336, collects the temperature difference between the two ends terminal of the sample using two Pt-100 thermal sensors (**see Figure 2.9a**).

2.5.4 Noise spectroscopy

Electrical systems, whether in materials or devices, often experience small fluctuations in their electrical resistance. These fluctuations are known as "resistance fluctuations" or "electrical noise". The average or typical resistance of a material is called the "time-averaged resistance" and is represented by the symbol <R>. However, the actual resistance at any given moment, R(t), can vary slightly around this average value. This variation is represented as $\Delta R = R(t) - \langle R \rangle$.These resistance fluctuations arise from small changes happening at the microscopic level within the material. By studying these fluctuations, we can gain insights into the underlying physical properties and behavior of the material or device at the most fundamental, microscopic scale. Understanding resistance fluctuations is important not only from a scientific perspective, but also for practical applications where electrical systems need to function reliably. Analysing these fluctuations can help identify and address issues in the design and operation of electrical components and devices.

There are mainly three types of Noise presents in a condensed matter system:

Johnson noise: Thermal fluctuations, commonly referred to as 'Nyquist noise', or 'Johnson noise', are a manifestation of the fluctuation-dissipation theorem[117]. The power spectral density (PSD) of thermal fluctuations for a resistor with resistance R maintained at temperature T is represented by,

$$S_V(f) = 4k_BTR. \quad \ldots\ldots 2.12$$

This spectral power ($S_V(f)$) remains constant across frequencies, akin to white noise. It is unaffected by the current flowing through the resistor or the material properties of the resistor, rendering it impractical except when assessing the effective electron temperature.

Shot noise: It is stemming from discrete carrier movement in devices, also exhibits a white noise profile. It manifests as fluctuating current with a spectral dependency, $S_I(f)$, directly proportional to the charge carrier (q) and current (I) in the device:

$$S_I(f) = 2q < I > \ldots..2.13$$

Shot noise serves as a crucial tool in mesoscopic physics, providing direct experimental insights into the charge and statistics of current-carrying quasiparticles in the system, especially noticeable at low temperatures and high frequencies.

1/f noise: The phenomenon of 1/f noise, prevalent in almost any resistor carrying current, showcases voltage fluctuations with a power spectrum following a $1/f^{\alpha}$ pattern, with α approximately equal to 1. Referred to as '1/f noise' or 'flicker noise' in literature, it is typically presumed that noise levels decrease inversely with the volume of the sample between probes. However, reducing sample size maintains noise source dimensions, intensifying overall electronic transport fluctuations. The spectral power of voltage noise $S_V(f)$ exhibits quadratic dependence on applied bias, leading to its augmentation beyond thermal voltage upon applying appropriate bias voltage. 1/f noise observations span various material systems, including semiconductors, metallic and magnetic films, spin glasses, heterogeneous conductors, superconductors in normal states, tunnel junctions, electronic devices, magnetic sensors, and even heartbeats. Beyond applications, it serves as a tool to explore diverse physics phenomena, encompassing structural phase transitions, magnetic domain wall motion, electron glasses, and quantum transport in low-dimensional systems[118–126].

Experimental Technique:

Generally, the fluctuation of voltage $\Delta V = \Delta V_{cf} + \Delta V_{bg}$ encompasses both conductance and background variations. The Power Spectral Density (PSD) $S_V(f, \delta)$ of the output ΔV (t) from the lock-in amplifier is expressed as follows:

$$S_V(f, \delta) \approx G_0^2 [S_V^0(f_0 - f) + (I_{rms})^2 S_R(f) \cos^2 \delta] \ldots.2.14$$

Here, $S_V(f, \delta)$ represents the PSD due to background fluctuations, and $S_R(f)$ denotes the spectral density of resistance fluctuations in the sample. G_0 signifies the product of the preamplifier and lock-in amplifier gains, f_0 stands for the excitation frequency, f indicates the measurement frequency, I_{rms} denotes the RMS value of the biasing current, and δ represents the phase angle of input voltage detection to the lock-in amplifier concerning the bridge current. When δ equals 0, $S_V(f, 0)/(G_0)^2 = S_V^0 + S_V^f$ (indicating noise from both sample and background

in the in-phase component). Conversely, when δ equals π/2, $S_V(f,\delta)/(G_0)^2 = S_V^0$ (signifying only background noise in the quadrature component). Hence, subtracting the out-of-phase signal from the in-phase one reveals the noise stemming from the sample due to resistance fluctuations. The concurrent measurement of background noise alongside conductivity noise represents the prime advantage of the AC technique[127] (see **Figure 2.10a**)

Data from the lock-in amplifier was sent to the computer using a 16-bit analogue-to-digital converter (either a in-built data acquisition of MFLI lock in or a National Instruments 16-bit DAQ) connected through LabVIEW. The acquisition card has an input impedance of about 10MΩ.

Due to under sampling of the data, there might be a discrepancy in noise measurement process. This discrepancy emerges due to inadequate sampling rates unable to catch high frequencies. As a result of this, the low frequency power spectral density is corrupted with the higher frequency signal due to aliasing effect. The aliasing problem is depicted in **Figure 2.9b**. In **Figure 2.9b**, the signal's sampled points suggest a single wave of a sinusoid, but in actuality, they represent five waves.

To overcome this issue, the anti-aliasing low pass filter is used to remove the unwanted signal. Employing the lock-in time constant targeted toward a value near fs/2 (~ 10ms), alongside the utmost attainable roll-off (~ 24dB/octave). Thus, any element exceeding fs/2 undergoes cutoff, with an attenuation surpassing 10^5 at f's/2, marking the effective bandwidth pre-decimation.

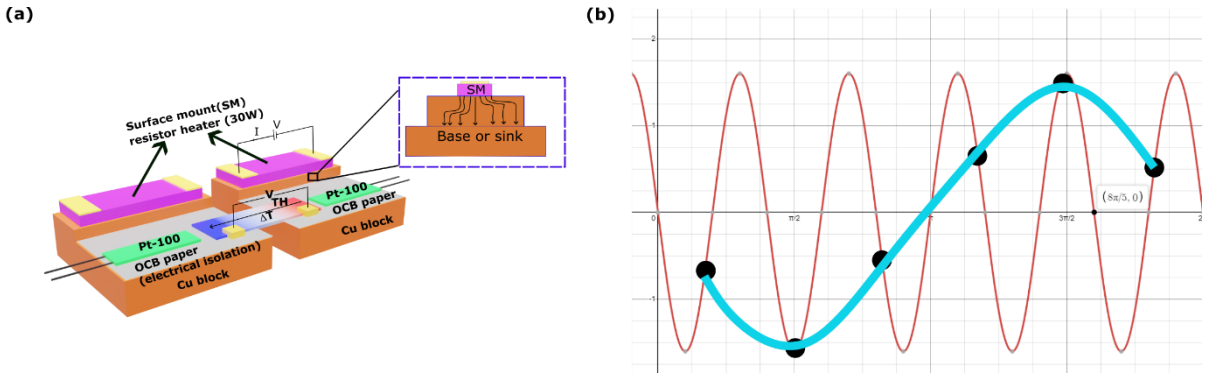

Figure 2.9 (a) *The schematic presentation of the Seeback effect set-up.* ***(b)***The red signal undergoes under sampling, represented by black dots, leading to the digitized signal depicted as a cyan line, which appears to possess a lower frequency compared to the original signal.

Subsequently, the signal undergoes digital passage through an anti-aliasing filter, with a cut-off set at f's/2, exhibiting an effective roll-off potentially reaching 80-100 dB/octave. This effectively eradicates all stray signal remnants beyond f's/2. The dataset is then resampled, capturing every 64th or 128th data point, thus reducing the sampling rate to fs, devoid of any aliased signals. Consequently, this approach

enables the acquisition of clear spectra across numerous frequency orders. FIR digital filters, employing a Kaiser window design, were deployed. To enhance efficiency and optimize memory utilization, decimation unfolds in three stages. For a total decimation factor of 64, a sequence of successive decimation factors of 8, 4, and 2 is utilized, while for a factor of 32, 4, 2, and 2 are employed. The digital filter's roll-off is maximized during the final stage. The data, transformed into digital form and then reduced significantly, underwent analysis to derive the voltage fluctuation's power spectrum. This was accomplished through a discrete Fourier transform approach termed the "averaged periodogram method," pioneered by Welch [128]. This

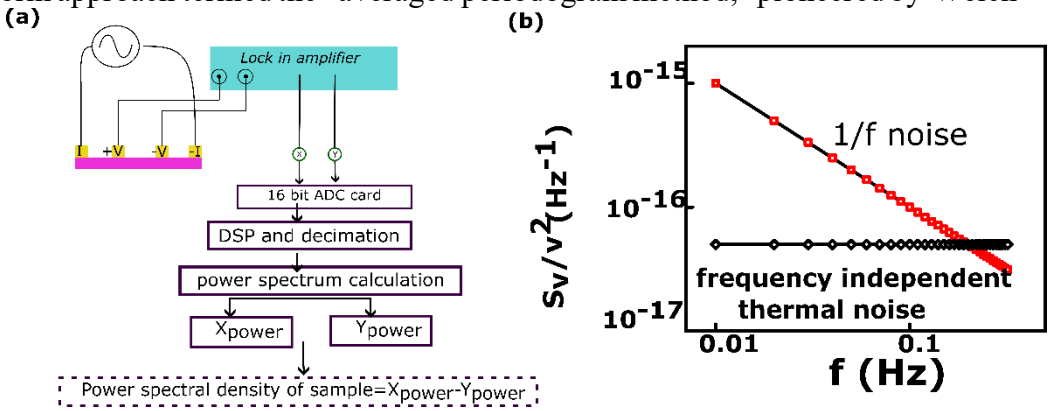

Figure 2.10 (a) *Lock-in amplifier based ac technique for measuring noise and the schematic diagram for obtaining the power spectral density (PSD).* ***(b)*** *A typical PSD vs. frequency plot displaying flicker noise and thermal noise in the same graph.*

technique offers notable benefits, including decreased computational steps and memory requirements, thereby shortening the overall processing time.

Chapter 3

Detection of Nontrivial Topology Driven by Charge Density Wave in a Semi-Dirac Metal

3.1 Introduction:

Efficient single-particle methods, exemplified by electronic structure computations, have proven to be adept in the successful identification of numerous topological materials through their distinctive topological invariants. However, the introduction of electron-electron interactions into this realm reveals a spectrum of more unconventional consequences. The theoretical landscape propose intriguing scenarios, suggesting that a Weyl semi-metal, under the influence of attractive electron-electron interactions, may undergo a transformative phase, emerging as a topological superconductor. Conversely, certain Weyl semi-metals that incorporate repulsive electron-electron interactions may manifest incommensurate charge density waves, with theoretical models predicting the occurrence of peculiar axion electrodynamics[129].

Beyond these captivating scenarios, the exploration of emergent topological phases has extended to include a plethora of novel quasiparticles. Among these are the quantum spin-hall insulator[3,15], fractional Chern insulator[130], and the intriguing possibility of an axial Higgs mode[131] This study aims to understand the unusual electronic structure of $LaAgSb_2$ with a broader goal to find materials with exotic ground states. $LaAgSb_2$, selected as an example of a square net compound, represents a type of structure where many intermetallic compounds have been identified as topological semi-metals[132,133]. As we delve into the unique characteristics of $LaAgSb_2$, we aim to contribute valuable insights to the evolving landscape of topological materials, shedding light on their potential applications and the fundamental understanding of exotic quantum states.

ARPES measurements, complemented by first-principal calculations, robustly confirm the presence of a tilted Dirac cone within the electronic structure of $LaAgSb_2$[87]. This distinctive feature adds a layer of complexity to the material's behaviour and contributes to the ongoing debate surrounding its unique electronic properties. Furthermore, $LaAgSb_2$ exhibits a notable

dual-phase behaviour concerning charge density waves (CDWs). The first CDW transition occurs at 211 K and is characterized by an incommensurate wave modulation spanning approximately 40-unit cells along the lattice vector *a*. Subsequently, at a lower temperature of 186 K, a second CDW transition ensues, associated with an incommensurate CDW along the c direction[134,135]. Intriguingly, as the temperature continues to decrease, a commensurate order emerges, involving six-unit cells[136].

However, despite the wealth of experimental data, the nature and origin of these CDWs in $LaAgSb_2$ remain subjects of ongoing discussion within the scientific community. Fermi surface measurements suggest a nesting vector near the calculated one, yet numerous experimental observations present challenges to a nesting-driven CDW scenario[67,137]. This difference shows that many complex factors affect the CDW phenomena in LaAgSb2. We need a better understanding of these factors and how they influence the material's electronic behavior. The combination of ARPES measurements, first-principle calculations, and complex CDW transitions in $LaAgSb_2$ creates an interesting avenue that encourages more research and could help us better understand exotic quantum states in topological materials. These observations align with the evolving understanding that, while there may be Fermi surface regions parallel to one another, other effects generally take precedence, and the direction of the charge density wave (CDW) modulation exhibits little to no correlation with the nesting vector. NMR experiments reveal that, despite the long wavelength associated with the CDW at 211 K, only two distinct La species have emerged, a phenomenon that appears unusual[138]. Moreover, the recent observation of superconductivity below 300 mK, coexisting with the CDW, suggests a robust electron-phonon coupling[139]. This coupling has been invoked in discussions about the characteristics of materials like $NbSe_2$[140], and 2H-$TaSe_2$[141].

An intriguing observation in the realm of electronics is the identification of non-saturated, quasi-linear magnetoresistance (MR) exhibiting distinctive characteristics both above and below the charge density wave (CDW) transitions[88]. The persistence of unsaturated quasi-linear MR at low temperatures remains enigmatic, with a simple attribution to the quantum limit of possible Dirac fermions in an isotropic Dirac semimetal[107]. Conversely, it has been theorized that systems featuring an anisotropic and tilted Dirac cone may display unsaturated quasi-linear MR whenever nonvanishing Berry curvature is present, indicative of a topological origin[56,142]. A deeper understanding of the interplay between topological characteristics and the CDW phase in this system is necessary.

The Planar Hall effect (PHE), denoting the transverse voltage generated when electric and magnetic fields are coplanar, has recently emerged as a transport-based probe for detecting non-trivial bands in various topological semi-metals or insulators[102,143–145]. Examples include $ZrTe_5$[146], Cd_3As_2[45], GdPtBi[147], VAl_3[148], Ta_3SiTe_6[149], Bi_2Se_3[150], and SmB_6[151].

In this chapter, we present the identification, achieved through first-principle calculations and electronic transport measurements, of an unconventional topological transition mediated by charge density wave (CDW) transitions in single crystals of $LaAgSb_2$. Experimentally, an anomaly in the ordinary Hall coefficient and zero-field resistivity is observed around 211 K, indicative of the CDW transition mediating the reconstruction of the Fermi surface. Additionally, in the low-temperature phase, we observe quasi-linear magnetoresistance, aligning with earlier findings in the literature [88].The most intriguing observation is the Planar Hall Effect (PHE) persisting from low temperatures to room temperature, accompanied by a change in the amplitude's sign at temperatures above the first charge density wave transition ($T > T_{CDW1} \approx 211$ K). Our computational analysis indicates a charge density wave (CDW) phase mediated by phonons, diverging from a mechanism driven by Fermi-surface nesting. This results in the distinctive stabilization of a low-temperature chiral metal phase. Concurrently, the low-temperature structure exhibits a breaking of inversion symmetry, leading to the presence of finite Berry curvature, explaining the observed PHE. Due to the anisotropic nature of the Dirac cone, the PHE in the high-temperature phase originates from an anisotropic response to a in plane magnetic field.

3.2 Experimental Results:

3.2.1 The crystal structure, electronic band structure, and resistivity vs temperature:

Single crystals of $LaAgSb_2$ were made[1] by the Sb-flux technique[88,136].Elemental La (Alfa Aesar 99.9%), Ag (Alfa Aesar 99.99%), and Sb (Alfa Aesar99.999 9%) in molar ratio 1: 2:20 were kept in an alumina crucible. The crcible was then placed in a quartz tube and sealed under dynamic vacuum. The quartz tube was kept at temperature 1050 °C for 12 h, and slowly cooled (2 °C h^{-1}) to 670 °C. At this temperature, the crystals were isolated from the flux of Sb by centrifugation. The obtained crystal was rectangular with crystallographic c-axis along the perpendicular of the plane. The Energy Dispersive X-Ray Spectroscopy (EDX) was done for elemental analysis on different regions of the single crystal (see **Figure 3.1b, and c**). The

[1] The single crystal was grown by Ratnadwip Singh from Prof. Prabhat Mondal's lab, S.I.N.P, Kolkata.

crystal structure of $LaAgSb_2$ is characterized by the tetragonal P4/mm space group. **Figure 3.1a** illustrates two distinct types of Sb atoms in the material. To create 2D layers, a specific type of Sb atom (depicted by red balls) and Ag atom (depicted by green balls) arrange themselves in a square net. These layers are alternately stacked along the crystal's c-axis and include sandwiched La ions (blue balls) and the other type of Sb atoms (yellow balls). The Brillouin zone for this structure, along with the corresponding high-symmetry points, is depicted in the inset of **Figure 3.1d**[2] The electronic band structure calculation reveals the presence of multiple linear bands intersecting the Fermi energy in various directions of high symmetry. **Figure 3.1e** displays the dispersion of these bands crossing the Fermi energy. The linear bands are highlighted using blue circles. The anisotropic nature of the linear dispersive band is shown in **Figure 3.1f** with k_z fixed at zero. The subsequent discussion focuses on temperature-dependent electrical resistivity, uncovering an anomaly in the zero-field resistivity upon cooling the sample below a typical temperature of 211 K (T_{CDW1}), consistent with earlier reports (see **Figure 3.2a**). Additionally, the system exhibits another anomaly at T_{CDW2}, discernible from the $\partial\rho/\partial T$ versus T plot in the left inset of **Figure 3.2a**. The partial opening of a gap, induced by a charge density wave (CDW) forming along the a and c axes, is associated with the transitions at T_{CDW1} = 211 K and T_{CDW2} = 183 K. The incommensurate order emerging at 211 K, spanning about 40-unit cells along the lattice vector a, has been attributed to the CDW transition. Consequently, the appearance of multiple inequivalent lattice sites would be anticipated. Intriguingly, NMR measurements reveal the detection of only two unique La sites. These measurements also suggest the potential existence of an underlying periodic unit. The CDW transition, initially incommensurate at T ≈183 K, descends in temperature and becomes commensurate at T≈164 K, involving six-unit cells in the c direction. To gain a deeper understanding of the system's behaviour, we concentrate on this transition. The lattice parameter c experiences a reduction with decreasing temperature. The electrons of Sb atoms, positioned directly above Ag atoms in the high-temperature structure (see **Figure**

[2] The theoretical band structure calculations were performed by Prasun Boyal from Prof. Priya Mahadevan's group (S.N.B.N.C.B.S)

3.1a),experience stronger repulsion from the Ag atoms' electrons. Consequently, neighbouring layers exhibit displacement in the x-y plane and form a modulated structure, as depicted in **Figure 3.2e,** when accounting for atomic displacements to minimize the total energy in a supercell involving six repeat units along the c lattice vector. The optimized unit cell reveals

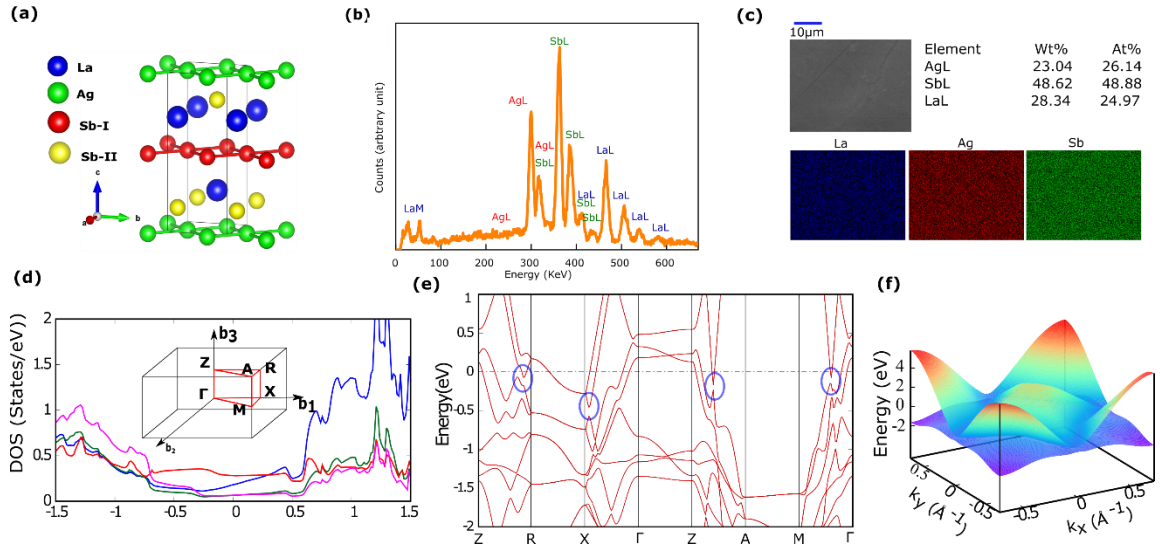

Figure 3.1: (a) *The room temperature tetragonal crystal structure of LaAgSb2 (side view).* ***(b)*** *The EDAX/ EDX spectroscopy data on a randomly selected area of a grown single crystal of* $LaAgSb_2$ ***(c)*** *FESEM image of a grown single crystal of* $LaAgSb_2$ *along with The elemental analysis of the EDAX data (for the elements present in the grown single crystal (where, Wt% and At% imply molar weight ratio and atomic weight ratio, respectively).* ***Overlay*** *of elemental mappings of La, Ag and Sb.* ***(d)*** *Atom projected partial density of states. Inset demonstrates Brillouin zone of* $LaAgSb_2$ *.****(e)*** *Electronic band structure of* $LaAgSb_2$ *including spin orbit interactions. The zero of the energy is Fermi energy (indicated by the blue dashed line). The linear band dispersions in the vicinity of the Fermi level have been indicated by the blue circled regions.* ***(f)*** *Anisotropic Dirac dispersive band which cross the Fermi energy across the* $k_z=0$ *plane of the Brillouin zone.*

an energy difference of 11 meV per formula unit. Despite the unusual presence of a chiral structure in a metallic system, $LaAgSb_2$ displays extremely weak bonding in the c direction. Our calculations, indicating an exfoliation energy of 115 meV $Å^{-2}$, confirm the classification

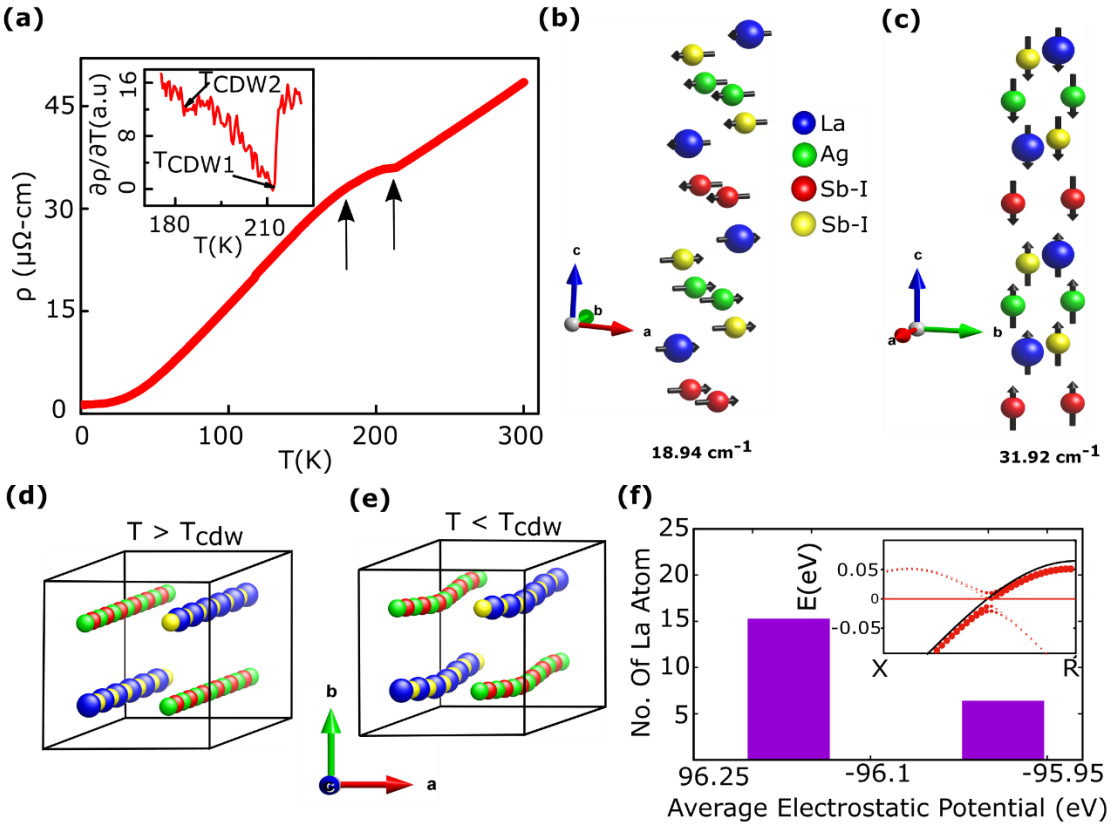

***Figure 3.2**: **(a)** Resistivity (ρ) versus temperature (T) plot exhibiting anomalies near the two CDW transitions indicated by the black arrows. Inset, showing the corresponding ∂ρ/∂T versus T curve to depict two CDW transitions (T_{CDW1} and T_{CDW2}) more clearly. The low frequency phonon modes for a bilayer with their frequencies indicated have been given. Panel **(b)** shows a shear mode, while panel **(c)** represents a compression mode. (d) Top view of the crystal structure of LaAgSb2 **(d)** without CDW modulation ($T>T_{CDW1}$) and **(e)** with CDW modulation ($T< T_{CDW2}$). **(f)** Histogram plot of no. Of La atoms in the CDW structure as a function of their average electrostatic potential. Two distinct types of La atoms in the modulated structure is observed. The inset showing Band structure of the modulated supercell unfolded onto the high temperature structure X to R direction. A small band gap opens because of the modulation in the c direction. Size of the red dots are proportional to the contribution of the supercell states at those k points. The black line corresponds to the band dispersion for the high temperature structure. The red dot-dashed line represents the Fermi energy in the calculation*

of this material within the potentially exfoliable group[152]. Additionally, our computations reveal the presence of very low-energy phonon modes, consistent with observations in other layered systems. These modes include shear modes that facilitate layer sliding and layer compressions, actively contributing to the formation of the modulated structure (see **Figure 3.2b** and **c** for the modes). This aligns with experimental evidence of low-energy modes reported in reflectivity studies[135]. The band dispersions, calculated for the modulated structure, have been unfolded onto the Brillouin zone of the high-temperature structure. This analysis reveals a small band gap along the RX direction, while a metallic band is observed in the other directions **(**see **Figure 3.2f)**

3.2.2 Planar Hall Effect and Magnetoresistance Measurement:

To explore the effect of charge ordering due to CDW formation on the transport mechanism in the system, we utilize a perpendicular magnetic field and measure the magnetoresistance as well as Hall signal with varying magnetic field (see **Figure 3.3a** for the schematic illustration of the measurement set-up). The MR shows a quadratic magnetic field dependency inside the normal phase as plotted in the left inset of **Figure 3.3b**. The MR data collected at T=300 K is fitted using the semiclassical Boltzmann transport's equation that follows[105]

$$MR = \frac{\alpha B^2}{\beta + B^2} \quad \ldots\ldots 3.1$$

Here α, β are used to denote fitting parameters.

However, a quasi-linear increase of MR with a magnetic field is discovered inside the CDW state of this system (see **Figure 3.3b**). The observation is well matched with the earlier studies in this system[88]. The Fermi surface's quasi-2D nature is verified through angular TMR studies inside the CDW phase which is plotted in **Figure 3.3c**. The experimental configuration is schematically shown in the bottom right inset of **Figure 3.3c.** Next, the ordinary Hall effect measurement is performed. The non-linear increase in Hall resistivity with an increase in magnetic field (B) below T=50 K, as depicted in **Figure 3.3d** is likely Dirac/Weyl Fermion. To correctly measure the angular planar Hall signal, the magnetic field is rotated in such a way that the current and magnetic field consistently remain in the same plane. We measure the Hall resistivity and magnetoresistance (MR) at various angles (θ) between the current and magnetic field to capture the planar signal. In **Figures 3.4a, and b**, the intrinsic planar Hall effect (PHE) signal is depicted for two representative temperatures, T = 10 K and 287 K, with B = 9T, after eliminating all misalignment components. The procedure to eliminate the misalignment is described in chapter 2.In the charge density wave (CDW) phase at 10 K, the planar Hall effect (PHE) signal exhibits typical characteristics, that contain valleys at 45° (225°) and peaks at 135° (315°).

[45]However, in the normal phase, a 180° phase-shift occurs, with peaks at 45° (225°) and valleys at 135° (315°). To further analyse the PHE data, Equation 3.4 is employed on the temperature dependent angular PHE data (with B fixed at 9 T), and Figure 3.4d illustrates the extracted $\Delta\rho$

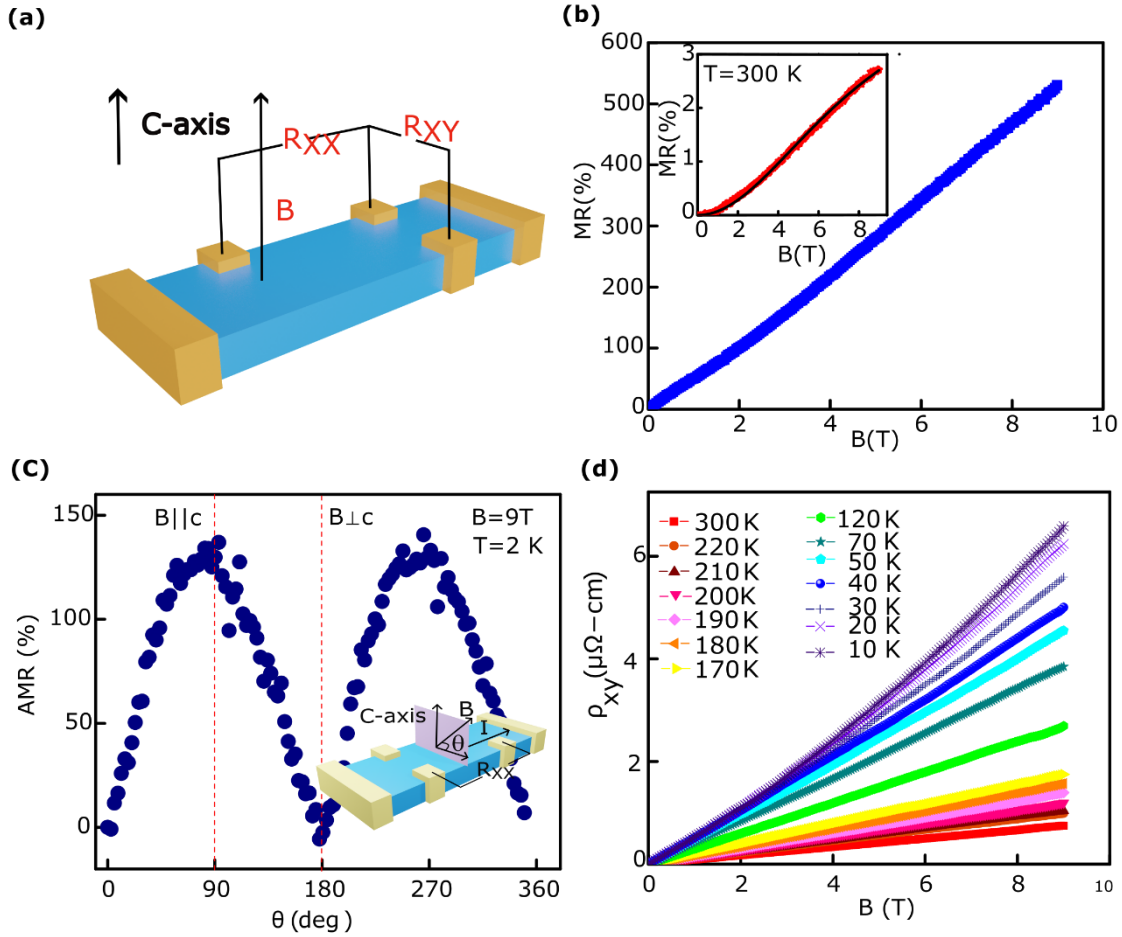

Figure 3.3: (a) *The schematic illustration of the measurement set-up for the magnetoresistance and ordinary Hall effect studies.* ***(b)*** *The TMR as a function of magnetic field at t=2 K with inset demonstrated the TMR vs. B plot at T=300 K while black line showing the fitting curve with equation* ***3.1****.* ***(c)***Angular transverse magnetoresistance (TMR) vs. θ at T=2 K and B=9T *with inset showing the configuration* ***(d)*** *Hall resistivity at different temperature*

versus T using a fixed magnetic field of 9 T. Clearly, with the temperature rising from 2 to 110 K, the Planar Hall Effect (PHE) coefficient systematically diminishes, reaching a point where it becomes nearly vanishes in the proximity of the Charge Density Wave (CDW) transitions. (T ≥ 150 K). Nevertheless, as noted in our dataset, it reappears at temperatures exceeding T_{CDW1} (≈211 K), but this time the amplitude is negative. Notably, a discernible PHE signal with $\Delta\rho$ = -ve is detected inside the normal state (T = 287 K), with a magnitude of ≈1.08×10^{-2} μΩ cm, which is an order of magnitude smaller than the value at T = 2 K ($\Delta\rho = 1.13 \times 10^{-1}$ μΩ cm). We choose another sample and measure the PHE signal above and below CDW.

The reversal in the amplitude of the Planar Hall Effect (PHE) caused by the formation of charge density waves (CDW) is confirmed for sample II. The effect of the CDW on the in-plane anisotropic magnetoresistance (AMR), which roughly follows Equation (2) at both below and above the CDW transitions, is then examined.

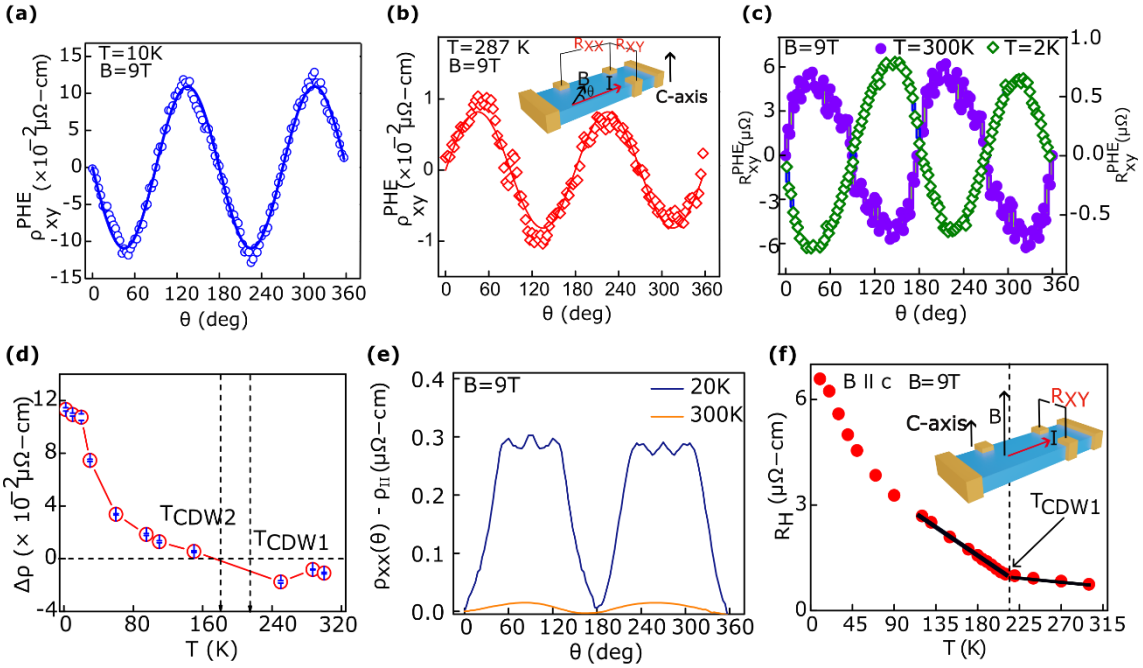

***Figure 3.4**. Angular variation of PHE resistivity (ρ_{xy}^{PHE})) at **(a)** T=10 K and **(b)** T=287 K (with inset showing experimental configuration of PHE measurement set-up.) with the fitted curve (solid lines) by Equation (1). **(c)** Angular variation of PHE resistivity (ρ_{xy}^{PHE})data taken from second sample at T=2 K and T= 300 K **(d)**) Temperature dependence of $\Delta\rho(B=9T) = \rho\perp - \rho\|$, extracted from the fitting of the PHE signal using Equation (1). Both the T_{CDWS} are indicated by vertical dotted lines. **(e)**Angular variation of the in-plane resistivity difference ($\rho_{xx}(\theta) - \rho_{\|}$) for B=9Tat temperatures below and $T>T_{CDWS}$ (T=20 and 300 K). **(f)** The temperature variation of the ordinary Hall coefficient (R_H), measured at B=9T with mentioning the CDW temperatures by arrow.*

Yet, in the high-temperature counterpart (>T_{CDW1} = 211 K), additional peaks appear in the charge density wave (CDW) phase at specific angles that are not visible. The CDW transitions break the crystal symmetry, intensifying the anisotropy in the Fermi surface. In the presence of a magnetic field, this lattice anisotropy induces anisotropic carrier scattering, potentially resulting in the emergence of additional peaks in the in-plane angle-dependent magneto-resistance, as per the semiclassical approximation. There have been reports of the topological Kagome metal KV_3Sb_5, which also undergoes charge density wave transitions, displaying a similar in-plane angle-dependent magneto-resistance. Furthermore, a modification in slope is observed near the charge density wave (CDW) transitions (**Figure 3.4f**) in the temperature dependence of the antisymmetric out-of-plane Hall coefficient (as illustrated in the inset of

Figure 3.4f for the configuration of the out-of-plane Hall effect measurement). This indicates a substantial reconstruction of the Fermi surface due to the formation of CDWs. Although there is a discernible slope change at $T \approx T_{CDW1}$, no discernible significant change is found $T \approx T_{CDW2}$. The temperature-dependent planar resistivity and planar Hall signals, coupled with the alteration in the ordinary Hall coefficient, unequivocally signify a modification in the topological characteristics of the electronic bands, facilitated by the formation of charge density waves.

Illustrated in **Figure 3.5a**, we conduct measurements of the angular Planar Hall Effect (PHE) signal in the charge density wave (CDW) state (T = 2 K) at various magnetic fields to gain insights into the PHE. Notably, **Figure 3.5b** demonstrates that the amplitude of the PHE, $\Delta\rho$,

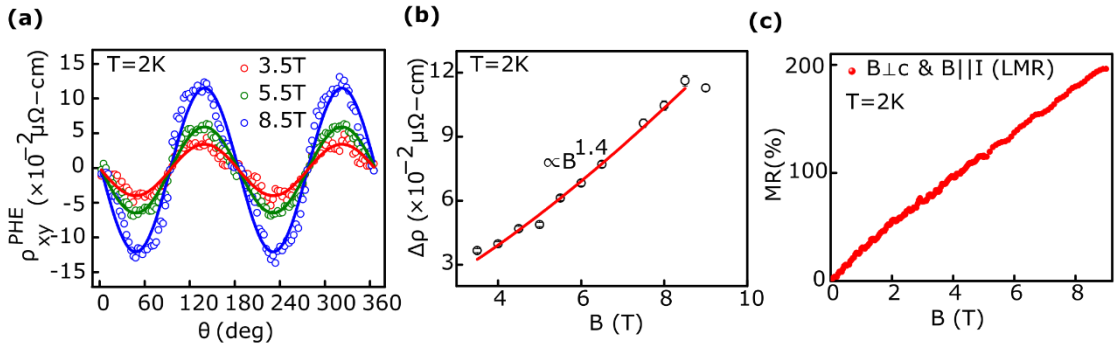

Figure 3.5. ***(a)*** *Planar Hall resistivity (ρ_{xy}^{PHE}) of $LaAgSb_2$ as a function of angle between the current (I) and magnetic field (B) at different B (T=2K).* ***(b)*** *Magnetic field dependence of $\Delta\rho=\rho_{\perp}-\rho_{\parallel}$, extracted by fitting the PHE signals with Equation (1) for different magnetic fields. The red solid line shows the fitted curve with a power law of B^{α}, where α=1.4.* ***(c)*** *Magnetic field evolution of longitudinal magnetoresistance (LMR) of the same sample with temperature fixed at 2 K.*

follows a power law with the magnetic field, exhibiting an exponent (α) of 1.4. Furthermore, we perform measurements of the longitudinal magnetic resonance (LMR) at T = 2 K with the current (I) and magnetic field (B) aligned parallel to each other (**Figure 3.5c**). LMR is commonly employed to identify chiral anomaly-assisted negative magnetoresistance. Contrary to expectations, our findings reveal a positive, non-saturating LMR that increases in a quasi-linear manner with the applied magnetic field, suggesting that the observed magneto-transport behaviour may be attributed to alternative mechanisms.

3.3 Theoretical Understanding of PHE:

Now, we'll try to comprehend the peculiar temperature-dependent behaviour of the PHE signal**.** **Figure 3.1a** depicts a Centro-symmetric high-temperature structure, and the magnetic nature

of the material is absent inside the normal phase. Thus, the system maintains time-reversal symmetry as well as inversion. As a result, the intrinsic Berry curvature is zero, suggesting that the PHE at high temperatures has a non-topological origin. Anisotropy in the in-plane resistivity in the presence of a magnetic field results from the anisotropy of the Dirac cones, as has been explained in the literature[150]. As backscattering between states at k and −k is permitted in the direction parallel to the in-plane magnetic field, while that is not the case in the direction perpendicular to the field, one finds that $\rho_{||}$ becomes $>\rho_{\perp}$ which leads to a planar Hall signal with negative amplitude according to the Eq. 3.4.

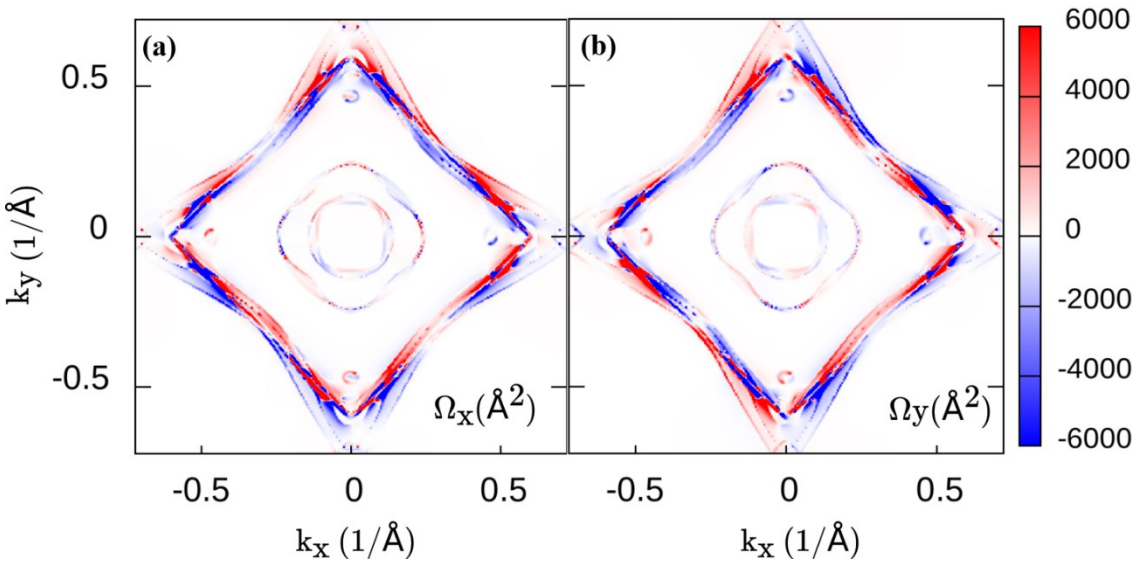

Figure 3.6: 2D colour plots of the **(a)** x and **(b)** y-component of Berry curvature in k_z=0 plane in the CDW phase

The centro-symmetric structure becomes non-centro symmetric by the formation of CDW modulation that we find (**Figure 3.1f**). The x and y components of the large intrinsic Berry curvature that results from this are displayed in **Figures 3.6 a, and b**, respectively. This is in line with the PHE signal's large-amplitude observed at low temperatures. In these systems, it is also anticipated to see a positive PHE amplitude ($\Delta\rho$) induced by the chiral anomaly and negative LMR, both of which vary quadratically with B. On the other hand, we find a quasi-linear positive $\Delta\rho$ and a quasi-linear positive LMR (see **Figure 3.5d**). Apart from the nonvanishing Berry curvature, emergent Weyl cones are tilted based on our theoretical calculations conducted in the CDW phase. Thus, the quadratic B term resulting from the chiral chemical potential imbalance and the linear B corrections to the resistivity caused by the tilted Weyl cones combine to produce the observed LMR and PHE signals[56,153]. Moreover, the same tilted Dirac cone-driven mechanism can also be attributed to our results of linear unsaturated

positive TMR[56] and the observed quasi-linear thermo-electric behaviour[154] as reported earlier[88].

3.4 Summary:

In conclusion, we have looked at $LaAgSb_2$, a material with square net structures, and investigated how its electronic structure changed as a function of temperature and the resulting topological characteristics. Its high-temperature structure has been linked to anisotropic Dirac cones, but the existence of inversion symmetry implies that it would not have any topological characteristics. This, together with the fact that there is a sign change and enhancement in its value below the CDW transitions, renders the observation of the planar Hall effect both at high and low temperatures perplexing. We employed geometry optimizations within first-principles electronic structure calculations to ascertain the low-temperature structure because the system's structure is unknown inside CDW phases. Despite the compound's three-dimensional network, we find a small exfoliation energy that places it in the regime of two-dimensional exfoliate materials with extremely low-energy shear phonon modes. This aligns with the main distortion observed in the optimized crystal structure, where adjacent layers are shifted relative to one another, resulting in a chiral structure that is surprisingly metallic as well. This shear instability is caused by the increased Coulomb repulsions between electrons on atoms that belong to different layers as the temperature drops. Due to the breaking of the inversion symmetry at low temperatures, this has a large Berry curvature. The tilted Dirac cone in a magnetic field is the source of the planar Hall effect in the high-temperature phase[150].

Chapter 4

Signature of commensurate CDW driven non trivial phase in 1T TaS_2

4.1 Introduction:

In our earlier exploration of topology and correlation in a condensed matter system in Chapter 3, we delved into how CDW can drive a system to acquire non-zero Berry curvature. Now, as we progress in our journey, it's crucial to revisit these insights on another CDW system, to better understand the implications. Here in this chapter, we focus on a particularly fascinating and widely investigated CDW system quasi-2d 1T-TaS_2, in which external tuning factors like temperature, pressure, or chemical substitution span an extremely complicated electronic phase diagram[60,155–161] This remarkable phase diagram also shows pressure-induced superconductivity and a phase known as the Mott phase in addition to multiple charge density waves (CDWs)[162,163]. A potential topological quantum spin liquid state has also been predicted due to the triangular arrangement of spin ½ Tantalum (Ta) atom inside C-CDW phase[164,165]. Apart from that, a many-body collective phenomenon in condensed matter known as the chiral charge density wave which is observed in 1T TaS_2[90] may have implications for topological physics and unconventional superconductivity[166]. Therefore, to deepen our understanding of topology and correlation, a complex CDW system like 1T-TaS_2 has been chosen.

As already discussed in Section 1.2.1.1 of Chapter 1, Berry curvature (BC), which is a geometrical property arising from the cyclic motion of electrons in k-space is believed to be the touching stone for detecting non-trivial bands. In the presence of an electric field, the BC acts like a magnetic field and drives the charge carrier to move perpendicular to the electric field like Lorentz force[11,142,167]. The anomalous Hall effect (AHE), anomalous Nernst effect (ANE) [168,169], planar Hall effect (PHE)[41,45,55,102,143,144] and additional phase shift in quantum oscillations[170,171] are examples of several exotic transport phenomena that result from BC, which is frequently thought of as a type of magnetic field in momentum space. The Chern number results from the integral of BC over the Brillouin zone for fully populated bands which

is the central idea of Topological properties[14]. In the linear response regime, the dissipation-less AHE vanishes in systems that preserve time-reversal symmetry. However, Sodemann and Fu suggested that The BC dipole (BCD) is crucial to the second-order nonlinear Hall effect (NLHE) in time-reversal invariant but non-centrosymmetric materials[172]. For details and understanding of the NLHE effect reader can see the Chapter 2. There is a fast-expanding interest in finding quantum materials that host the NLHE effect, which is in line with the increasing interest in different nonlinear phenomena such as nonlinear optics[173]. In response to a longitudinal AC probe current, it generates a second-harmonic Hall voltage that has potential uses in high-frequency rectifiers, wireless charging, energy harvesting, infrared detection, etc. In several material systems, including two-dimensional (2D) monolayer or few-layer WTe_2[50,51,174], Weyl semimetal $TaIrTe_4$[175], two-dimensional (2D) MoSSe[176] and twisted WSe_2[177], corrugated bilayer graphene[178], and a few topological materials, BCD and its associated NLHE have been predicted[179]. The discovery and characterisation of quantifiable signals of the topological shift close to criticality, however, for systems with a topological electronic phase transition in which local order parameter physics is absent, remains mainly an open subject. Recent theories claim that simultaneous changes in the BCD occur together with topological phase transition[180].

Here, we unveil the emergent topological behavior resulting from a CDW transition in 1T-TaS_2. As the system transitions from the nearly commensurate (NC) to the commensurate (C) CDW phase, a pronounced PHE signal emerges abruptly, accompanied by a strong NLHE signal. This transition coincides with a change in the sign of both the ordinary Hall coefficient and the Seebeck coefficient, indicating a substantial alteration in the Fermi surface due to the CDW transition. Collectively, these transport features suggest a topological transition driven by the formation of the commensurate CDW phase. Our theoretical calculations reveal the emergence of the Berry curvature dipole induced by the inversion symmetry breaking of the chiral CDW phase and the tilted nontrivial gapped anti-crossing band. This strong coupling between BC and CDW ordering further gives rise to finite nonlinear Hall effect and planar Hall effect in the C-CDW phase

4.2 Experimental Results:

4.2.1 Crystal structure and resistance inside different phases:

To characterise the different ground states, at first, we measure the resistance as a function of temperature. The resistance vs temperature plot is shown in Fig 1b. which indicates different degrees of commensurate CDW phases. There is a hysteresis between the cooling (Blue curve) and heating (Red curve) curves, which suggests a first-order phase transition during the transition between NC-CDW and C-CDW as also reported early[181]. A hexagonal Star of David

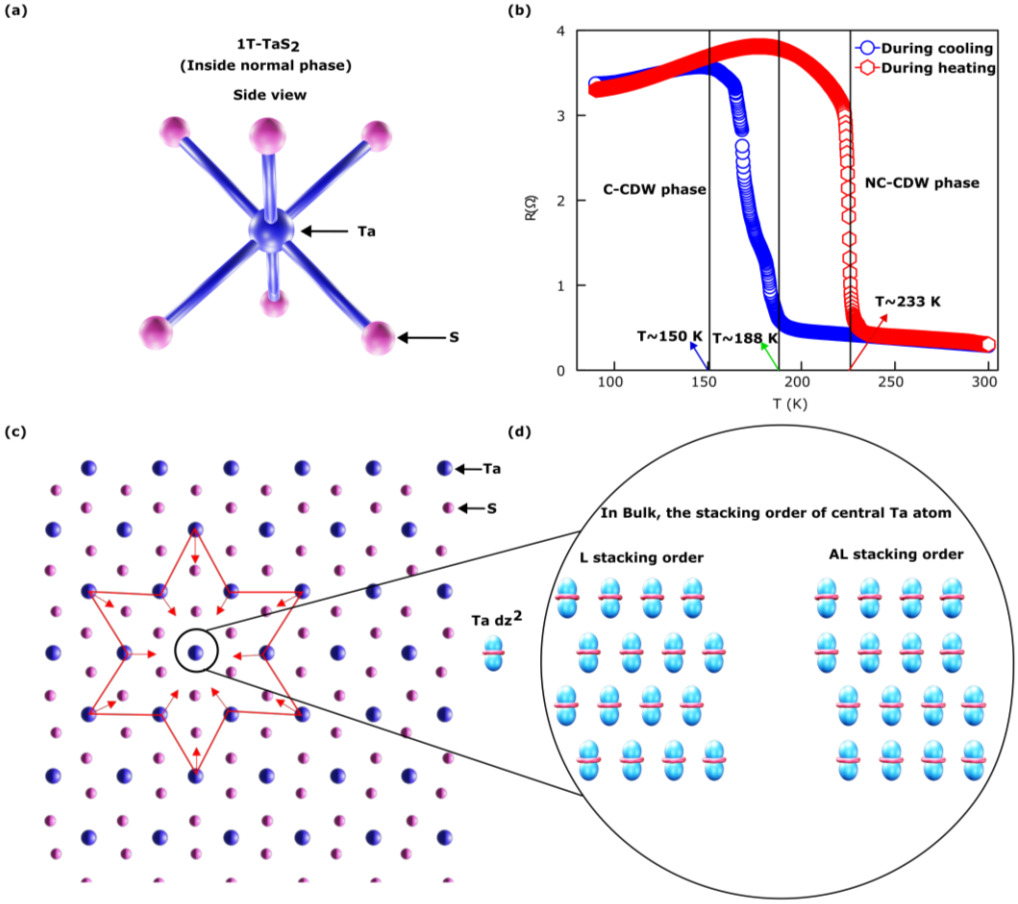

Figure. 4.1: The crystal structure and electronic transport in different phases| (a). *Top and side view of single layer of 1T-TaS_2 inside normal phase.* ***(b)****. Resistance vs temperature plot with hysteresis (red curve showing heating and blue curve showing cooling plot.).* ***(c).*** *The schematic of the star of David (SD) configuration of Ta atoms (red line) inside the C-CDW state is demonstrated.* ***(d).*** *The schematic of the stacking order of central Ta atom of SD cluster in bulk, the AL and L stacking of central Ta d_{z^2} of SD cluster inside the C-CDW phase.*

(SD) cluster is formed by the 13 Ta atoms in the C-CDW phase. In the C-CDW phase, twelve of these atoms are tightly bound to each other and form the valance band, leaving one half-filled band from the central Ta atom behind (displayed in **Figure 4.1c**). As a result, the triangular superlattice formed by the SD governs the electronic band structure in a single

layer[181]. Recent experimental and theoretical understanding suggest that in bulk form, the interlayer hopping is responsible for the mysterious electronic transport in the Commensurate CDW phase[182–184]. In bulk, taking Ta d_{z^2} which is the centre of SODs as site A, there are 13 possible ways, SOD from the second layer can sit. Among those configurations, the AL and L stacking configurations (see **Figure 4.1d**)—are highly stable, according to the computed total energies. They differ in energy by just 1.1 meV/star, but they are far more stable than the other forms[182]. The system in the C-CDW state behaves like a metal when the stacking order is L (T > 50 K), and in the AL stacked configuration (< 50 K), it exhibits insulating properties. Here, in this chapter, we uncover the effect of stacking order leading to nontrivial electronic and topological phases near the NC-CDW to C-CDW phase transition through a combination of transport experiments. [182]

4.2.2 Non-linear Hall effect:

The second-order transverse voltage (or current) in response to a longitudinal current (or

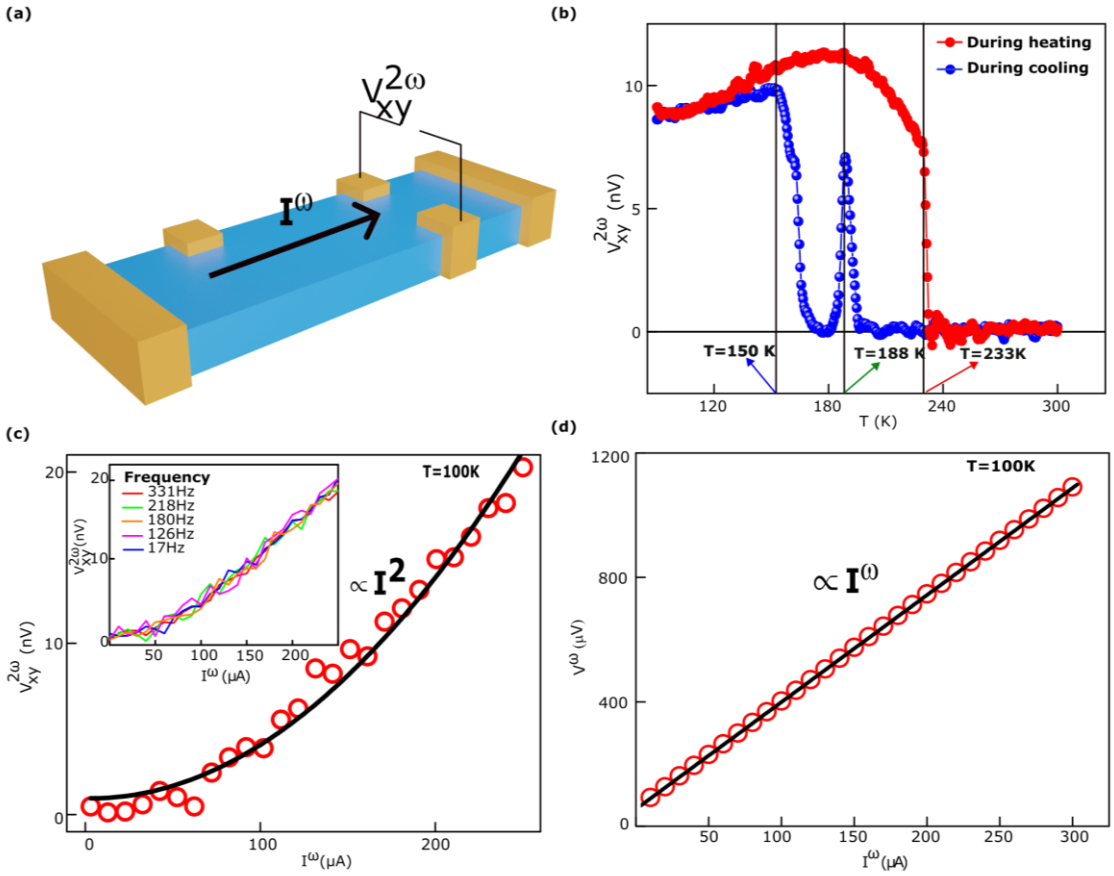

Figure 4.2 (a) *Schematically drawn configuration of NLHE measurement set up.* ***(b)*** *Temperature dependence of NLHE signal during cooling (blue color) and heating (red color). Two transitions during cooling are marked by a blue (150 K) and a green (188 K) arrow, and a red (233 K) arrow is used to mention transitions during heating.* ***(c)*** *Bias current dependence of NLHE signal at a representative temperature (T=100 K). Black line shows the fitting curve with quadratic equation(I^2) and the top left Inset shows the plot of second harmonic voltage($V^{2\omega}$) as a function of current(I^{ω}) at different drive frequency at T=100 K.* ***(d)*** *I-V characteristic of the sample at T= 100 K with the black line shows the linear fitted curve.*

electric field) is referred to as the nonlinear Hall effect (see Chapter 2 for more details). A double-frequency transverse voltage V^{2w} can be measured when a low-frequency excitation current, I^{w} is supplied, as illustrated in **Figure 4.2a.** The nonlinear Hall effect, in contrast to all other Hall effects previously recorded in the linear-response zone, needs inversion symmetry breaking rather than time-reversal symmetry breaking by an external magnetic field or magnetism. The temperature evolution of non-linear Hall voltage is carried out further to comprehend the non-trivial electronic band during the crossover of phase. The NLHE signal is

absent inside the NC-CDW phase, but it suddenly appears during the NC-CDW to CDW transition, pointing toward a topological transition. At T = 196 K, the NLHE signal begins to rise; it achieves its peak value at T = 188 K (as mentioned in **Figure 4.2b** using the green arrow), and with further cooling, it vanishes. The NLHE signal remains zero within the temperature range T=172 K-182 K. At T =172 K, the NLHE signal again rises; it achieves its maximum value at T = 150 K (as indicated by a blue arrow in**. Figure 4.2b**), Significantly large NLHE signal is present inside C-CDW state within the measurement temperature from T=90 to 150 K. During heating, the non-linear Hall signal is also observed inside C-CDW phase and vanished when the system enters to NC-CDW state (T > 233 K) with a hysteresis alike the thermal hysteresis observed in resistivity data. **Figure 4.2c** displays that the NLHE signal varies quadratically with bias current which supports the non-linear nature of the signal. The appearance of the NLHE signal only inside the C-CDW state suggests that the signal is indeed a property of the material system and associated with phase transform. $V^{2\omega}$ as a function of I^{ω} at several drive frequencies is presented in the inset of inset of **Figure 4.2c.** It is evident from the plot that the signal is insensitive to the drive frequency. This observation suggests that no capacitive source is involved in the non-linear transport in this system The ohmic contact is confirmed by observing linear IV response as depicted in **Figure 4.2d** which exclude the contact induced NLHE signal.

4.2.3 Planar Hall measurement:

In presence of a planar magnetic field, the appearance of a symmetric Hall signal in a non-magnetic material is associated with non-vanishing BC in momentum space. To provide evidence for a non-trivial electronic band of 1T-TaS_2 inside the C-CDW state, the PHE measurement is conducted in the both C-CDW and NC-CDW state. To detect the planar Hall signal, we rotated the magnetic field in such a way so that the current and magnetic field always stayed in the same plane, and we simultaneously measured the Hall resistivity at various angles (θ) between the current(I) and magnetic field (B). The schematic describing the configuration of measurement is depicted in **Figure 4.3a**. By the general theory of anisotropic resistivity caused by non-zero BC for topological material[102,143], in-plane transverse resistance (PHE) can be expressed as,

$$R_{xy}^{PHE} = -\Delta R^{PHE} \sin\theta \cos\theta \text{ , where } \Delta R^{PHE} = R_{||} - R_{\perp}. \quad \ldots 4.1$$

$R_{\perp}$ is the resistance when B ⊥ I and $R_{||}$ is the resistance when B || I. The angle dependent PHE signal at different magnetic fields is plotted in **Figure 4.3b** with the temperature fixed at 90 K. The PHE shows an angular period of 180°. In particular, the valleys and peaks of the PHE are at angles of 45°(225°) and 135° (315°), respectively. This is not like the angular dependence of

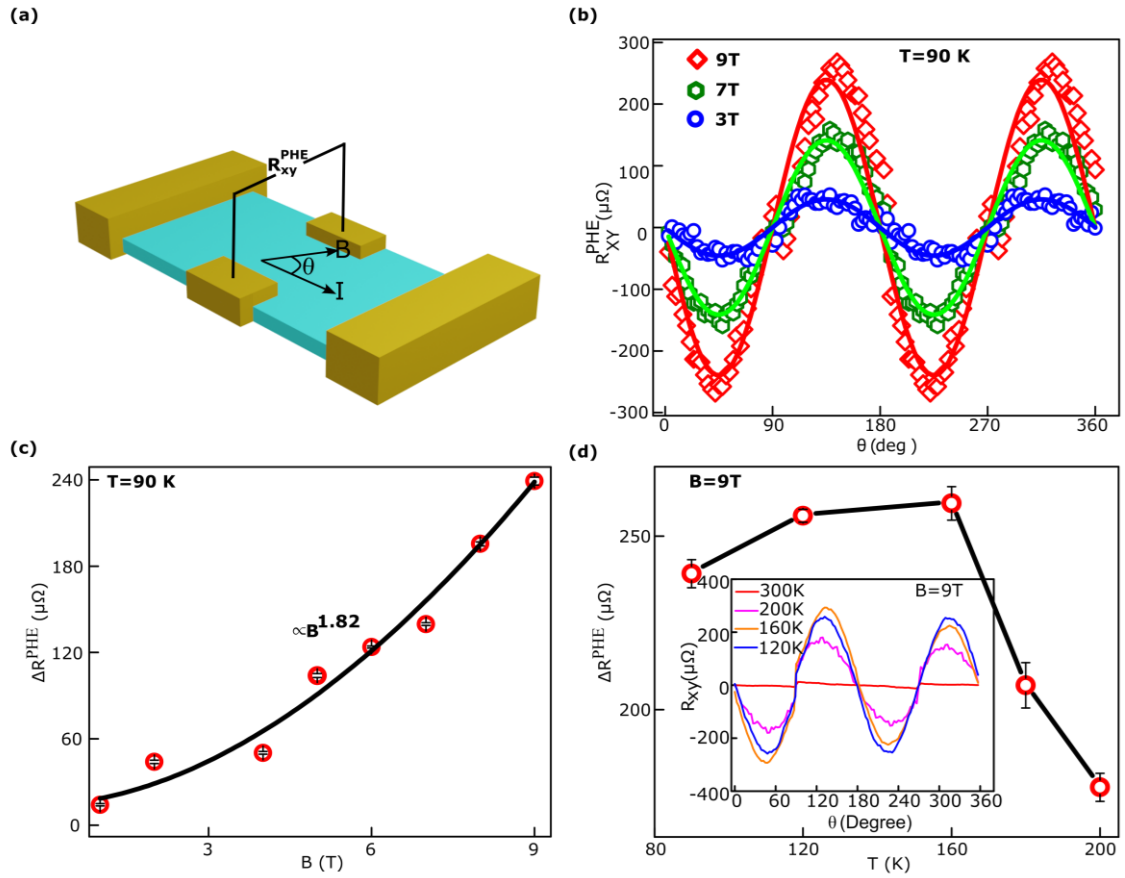

Figure 4.3 (a) *The schematic diagram of the PHE measurement configuration (**b**) Planar Hall resistance* R_{xy}^{PHE} *of 1T-*TaS_2 *as a function of angle between I and B at different magnetic fields (with T=90 K)**.(c)** Magnetic field dependence of* ΔR^{PHE} *extracted by fitting PHE signals with Eq. 1. at different magnetic fields (black solid line displays the fitting curve with power law* B^{α}*, where* α*=1.82). **(d)** Temperature dependence of* ΔR^{PHE} *extracted by fitting PHE signals with Eq. 1. of magnetic field fixed at 9 T.*

the ordinary Hall effect (OHE), which has a period of 360°. The error due to misalignments has been taken care in similar way like **Chapter 3.** The ΔR^{PHE} extracted from fitting the PHE signal by $R_{xy}^{PHE} = -\Delta R^{PHE} \sin\theta \cos\theta$. Magnetic field variation of ΔR^{PHE} is presented in **Figure 4.3c** which shows power law (B^{α}) behaviour with the magnetic field (B) with the exponent, α=1.8. Extracted ΔR^{PHE} at different temperatures is displayed in **Figure 4.3d** inside C-CDW phase. The angle-dependent PHE signal is shown in the inset of **Figure 4.3d**. The angle-dependent PHE signal is vanishingly zero inside the NC-CDW phase.

4.2.4 Ordinary Hall effect:

Furthermore, to get the information of the Fermi surface, the anti-symmetric ordinary Hall measurement is carried out. Within the NC-CDW state, the Hall resistivity is negative, indicating that electrons are the primary carriers of current in this state.

However, during the transition to the C-CDW state, the Hall resistivity undergoes a sign change from negative to positive, suggesting a shift in majority carriers from electrons to holes. An abrupt change in Hall carrier density is observed around the NC-CDW to C-CDW phase transition, before the sign change in carrier density within the C-CDW state which indicates the Fermi surface modification. Both during heating and cooling, the carrier density exhibits a

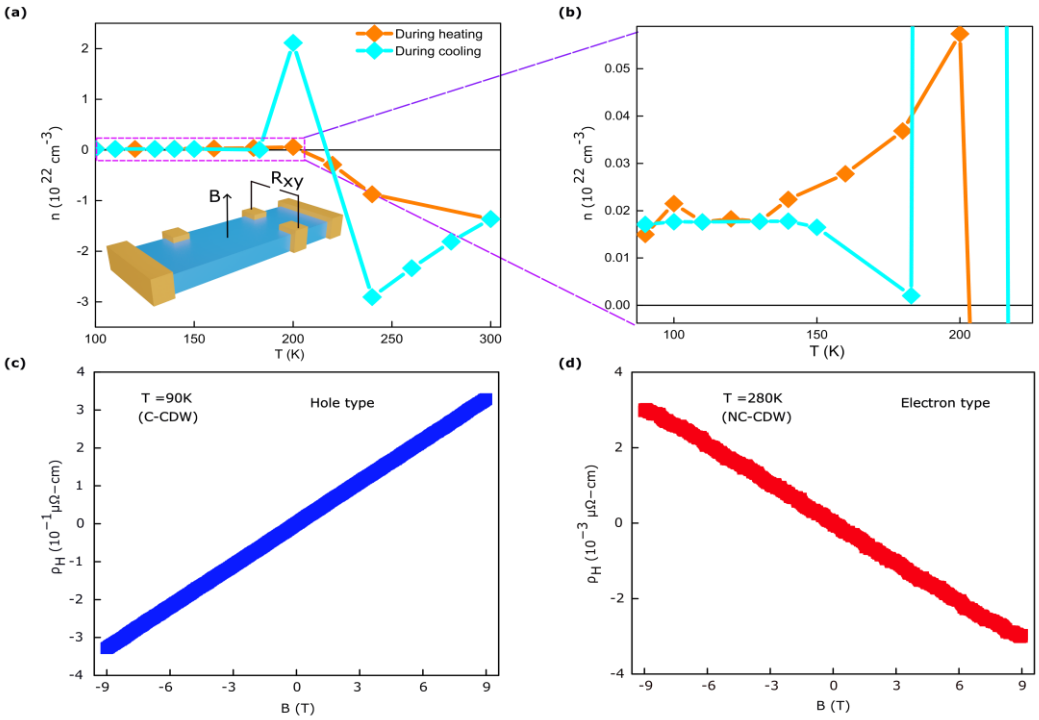

Figure 4.4 (a)*Variation of carrier density (n) with temperature (plot in orange color denote the data during heating and cyan represents the data during cooling of the system). The inset displays the schematic of the measurement set-up* ***(b)*** *Zoomed plot of the carrier density (n) vs. temperature. Magnetic field dependence of Hall resistivity at* ***(c)****T= 90 K (C-CDW).* ***(d)*** *T= 280 K (NC-CDW).*

similar diverging nature and sign reversal, suggesting that the fully commensurate CDW creates a hole pocket. The slope of the curve ρ_H vs B is used to calculate carrier density. The formula for the calculation of carrier density is mentioned below[185]:

$$\frac{\rho_H}{B} = R_H = \frac{1}{ne} \qquad \ldots.4.2$$

Inside the C-CDW phase, the material's hole carrier density is p~$1^{02^{o}}$ cm^{-3} which is like a low carrier density metal. Few nontrivial nodal lines semimetal show similar order of carrier concentration. But the carrier density increases by two orders (n~10^{22}) cm^{-3} when the system resides at NC-CDW state. In summary, our anti-symmetric ordinary Hall effect measurements indicate that the formation of the C-CDW has a significant impact on the Fermi surface and its related properties.

4.2.5 Seeback effect:

The electrochemical potential is located at a delocalized band in a conventional metal and degenerated semiconductor, where only a constant population of electrons with a Fermi energy

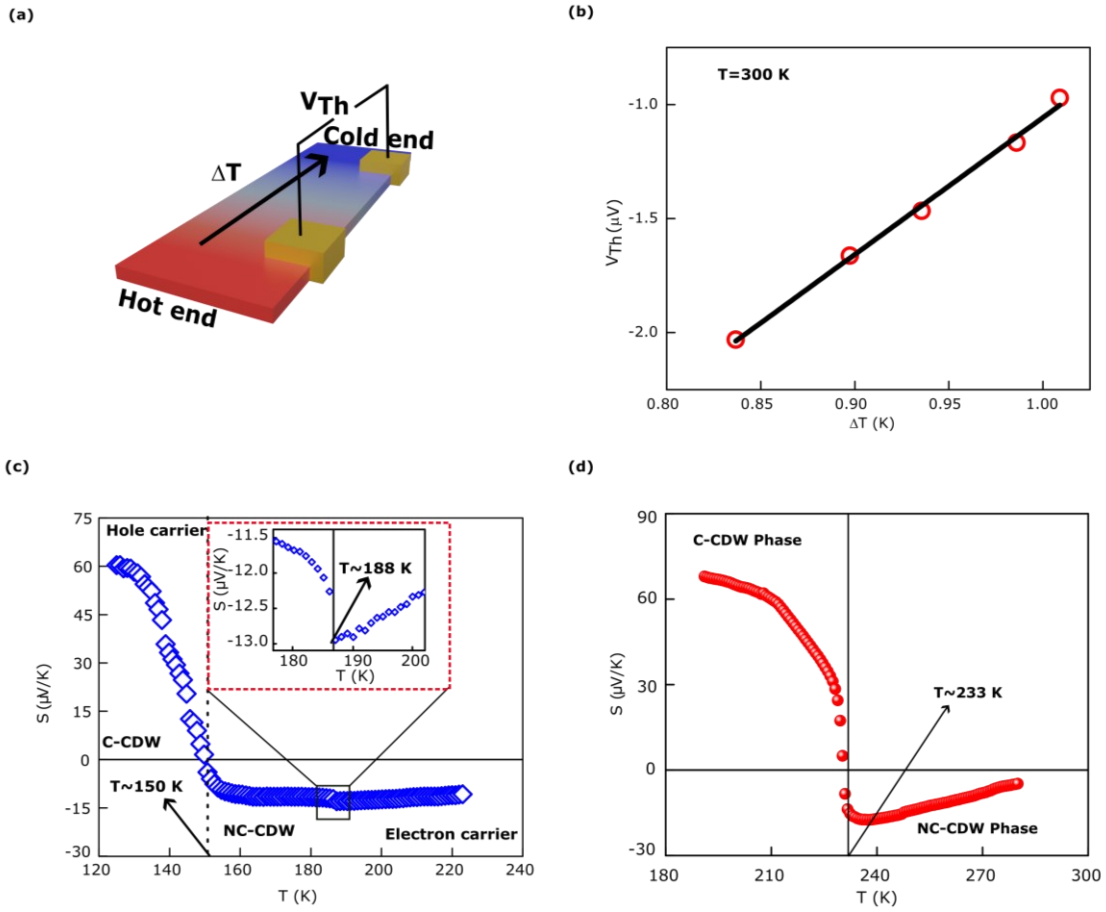

Figure 4.5. (a) *The illustration of the measurement configuration of Seeback coefficient* ***(b)*** *The thermoelectric voltage as a function of temperature difference between hot and cold end at room temperature.(* ***c****) The Seeback coefficient as a function of temperature during cooling with right inset showing Seeback coefficient vs. temperature plot in the temp range 180-200 K (****d****) The Seeback coefficient as a function of temperature during heating.*

of a few k_BT contributes to both charge and thermoelectric transport. According to Mott's formula[186], the Seeback coefficient depends on the carrier density. So, to understand the

modification of the Fermi surface with temperature, we perform thermoelectric voltage measurement as a function of temperature. The schematic is shown in **Figure 4.5a and** in **Figure 4.5b** the thermoelectric voltage as a function of temperature difference between hot and cold end at room temperature is shown, which confirm the linear dependence between them. Inside the NC-CDW phase, the Seeback coefficient increases linearly with a decrease in temperature. An effective reduction of thermoelectric voltage occurs at T~188 K (zoomed plot is shown in the inset of **Figure 4.5c**), which suggests that the contribution from the hole carrier is also taking place in thermal transport[181]. With further reduction of temperature, at T~150 K (indicated by the arrow in **Figure 4.5c**), the sign of the thermoelectric voltage changes from negative to positive.

The sign reversal signifies the appearance of a hole pocket in the Fermi surface inside the C-CDW phase. During the warming up of the sample, a similar sign change of the Seeback coefficient is also noted (see **Figure 4.5d**). Our result is well agreed with the previously reported results of this system in literature[181]. It is usual for competing electronlike and hole-like excitations, or multiband transport, to exhibit such a sign switching in the temperature dependence of S (T)[187].

4.2.6 Methods:

Single crystal of 1T-TaS_2 is bought from 2D Semiconductors. Silver paint and gold wire are used to make an electrical connection with the single crystal of the 1T TaS_2. To measure the non-linear Hall signal, Ac sinusoidal voltage with a drive frequency of 17 Hz is applied to the sample and the transverse voltage at twice the drive frequency is acquired using standard lock-in technique with SR83º (Stanford Research Systems Model) and with preamplifier SR554. PHE and LMR were measured in a commercial measurement system Quantum Design PPMS. The thermoelectric transport responses were measured in a high vacuum condition in a homebuilt cryogenic insert. A nanovoltmeter to collect signals and Pt-100 and Lakeshore 336 are used to sense temperature differences. See **Chapter 2** for more details about the thermoelectric setup.

4.3 Theoretical understanding:

To have a non-vanishing Berry curvature monopole or dipole, the system must be non-centrosymmetric or TRS broken magnetic material. The absence of magnetic order has been confirmed previously through magnetisation, muon spin relaxation (μSR) and polarized neutron diffraction measurements, nuclear quadrupole resonance (NQR)[188–190]. As long-range magnetic ordering is absent in this material system one can exclude that there is no TRS broken Berry curvature in this phase[191]. So another possible source of non-zero Berry curvature is inversion symmetry breaking. The chiral nature of the crystal is established by Yan Zhao et al.[192] and Bryan T. Fichera et al.[89] which confirm the breaking of inversion symmetry in the system. Both Yan Zhao et al. and Bryan T. Fichera et al. in their paper demonstrated that the optical second harmonic signal appears when CDW is formed.

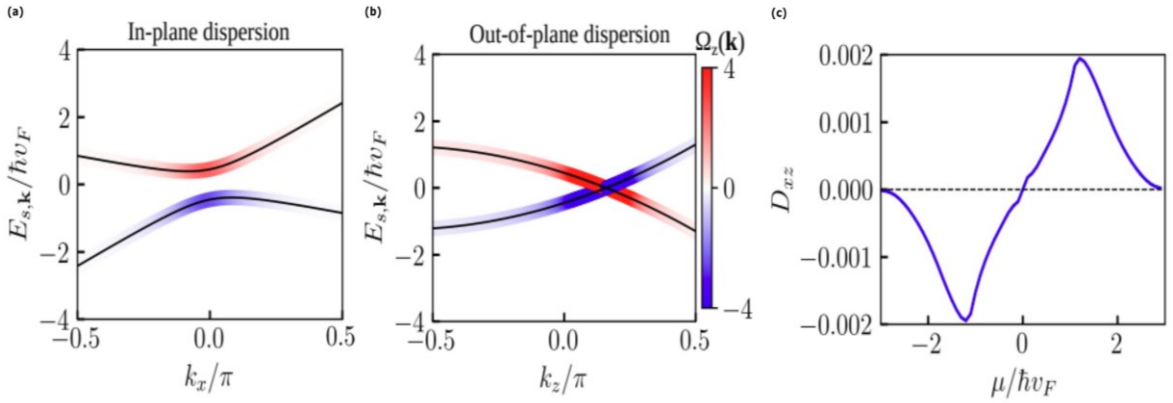

Figure 4.6. *Band dispersion of the effective low energy Hamiltonian described in Eq. (4), along* ***(a)*** *the in plane (by setting ky = kz = 0) and* ***(b)*** *out-of-plane (setting k_y = kx = 0) momentum. It qualitatively captures the electronic states of 1T-TaS_2 near the Fermi energy. We have used the following parameters: $v_t = 0.5v_F$, $k_0 = 0.5$, and $\alpha = 0.2$. The z-component of the Berry curvature - $\Omega_z(k)$ - is superimposed over the band dispersion.* ***(c)*** *The variation of the corresponding Berry curvature dipole D_{xz} with chemical potential μ. Finite D_{xz} leads to a finite nonlinear Hall current density along transverse direction for an applied electric field along the x-axis.*

We capture these essential features of the electronic states via a low-energy Hamiltonian having a (spin degenerate) band crossing at $k_z = k_0$ to describe the NLHE signal inside C-CDW state as follows[3]:

$$H(k) = \hbar v_F\left(k_x \sigma_x + k_y \sigma_y\right) + \hbar v_F (k_z - k_0)\sigma_z + \hbar v_t \sigma_0 k_x \quad \ldots\ldots 4.3$$

[3] The theoretical calculations were performed by Debasis Dutta from Prof. Amit Agarwal's group (IIT Kanpur)

The Hamiltonian described above represents a gapped system for each $k_z = k_0$ with a finite tilt velocity or anisotropy along the k_x direction. The anisotropy introduced via the v_t term in Eq. (4.3) breaks the rotational symmetry of the model by introducing a mirror plane along the x-axis in the $y - z$ plane. The presence of a mirror plane is crucial to have a finite BCD in the system which explains the observation of NLHE[172]. The sudden rise of NLHE amplitude around the phase transition might be due to the crossing of the Fermi level to the hotspot of BCD. The ordinary Hall effect shows an anomaly around the transition of NC-CDW to C-CDW which further suggests the scenario. Furthermore, the presence of non-vanishing Berry curvature due to a gapped Dirac cone is a reason for giving rise to the PHE signal inside C-CDW. But, in the nearly commensurate CDW (NCCDW) phase, there are multiple domains of David of stars clusters, which are randomly oriented in the $x - y$ plane. These random domains cancel the overall NLHE and PHE signal inside the NC-CDW phase.

4.4 Summary:

In summary, we have established a connection between CDW formation and a non-trivial electronic band of 1T-TaS_2 using BC monopole-sensitive PHE and BC dipole-sensitive NLHE measurement. Due to the formation of chiral C-CDW, inversion symmetry is broken in this system which drives the system to acquire a non-vanishing BC monopole and dipole. The Seeback and anti-symmetric out-of-plane Hall effect are used to support the CDW-driven Fermi surface modification. Our results suggest that one can use the NLHE technique to detect symmetry-breaking phases. Furthermore, the hysteresis in the NLHE signal between heating and cooling makes the system a potential candidate for topological-based memory devices. Our results show an interesting connection between Berry curvature and symmetry broken phase transition which will deepen the understanding of the topological and correlated systems.

Chapter 5

Interplay between topology and spin ordering in an antiferromagnetic system

5.1 Introduction:

In the previous two chapters we talked about how charge ordering affects the topological properties of condensed matter systems. In this chapter, we will introduce the effect of spin-ordering on non-trivial electronic bands. Material systems with the formula $RAgSb_2$, where R represents a rare earth element, are known for exhibiting a variety of intriguing and complex physical properties such as charge density waves, heavy fermionic behavior, antiferromagnetism[193–199]. While we have already discussed the intricate interplay between CDW and topology in $LaAgSb_2$, to capture the effect of spin ordering on the topological property of $RAgSb_2$ square net series, we choose Rare-earth Gaddolium (Gd) (the crystal structure is schematically shown in **Figure 5.1a**). Previous studies in this materials including powder neutron diffraction study, x-ray resonant exchange scattering measurements, and Mössbauer spectroscopy[200,201] established that the moment of Gd atoms are arranged perpendicular to the c-axis anti-ferromagnetically below 13.8 K. While extensive magnetic measurements were performed on this system, a large and non-saturated anisotropic MR is discovered in this material[193]. The mechanism behind this extraordinary transport and the coupling between the charge transport with the magnetic order are yet to be understood.

Here, we unravel the unusual electronic and topological behavior facilitated by the magnetic order in this material by performing a systematic magneto transport studies such as magnetoresistance, ordinary Hall effect and Planar Hall effect. Single crystal of $GdAgSb_2$ is grown using the self-flux method. It was then characterized through a detailed magnetic and electrical transport study. The TMR displays a quadratic large non-saturating behaviour with the increase of the magnetic field. This behaviour is associated with electron-hole compensation like topological semimetal. The low effective mass of the charge carrier indicates a linear dispersive band. Furthermore, the observation of Berry curvature-sensitive PHE signal is suggesting toward the non-trivial electronic transport. The discovery of an anomaly of PHE

signal around anti-ferromagnet ordering temperature indicates the interplay between spin ordering and topological properties.

5.2 Experimental results:

5.2.1 Characterization:

Self-flux technique is used to make single crystal $GdAgSb_2$[4]. A surplus amount of antimony is used to grow this material. With a ratio Gd:Ag: Sb = 1:2:2º, the elements are combined and placed inside a crucible made of alumina. Then the crucible is sealed with high vacuum in a quartz tube. Slow heating up to 12⁰⁰ c followed by slow cooling down to 67ºc of quartz tube is made to grow the crystal[193]. The centrifuge at high temperature is used to remove excess

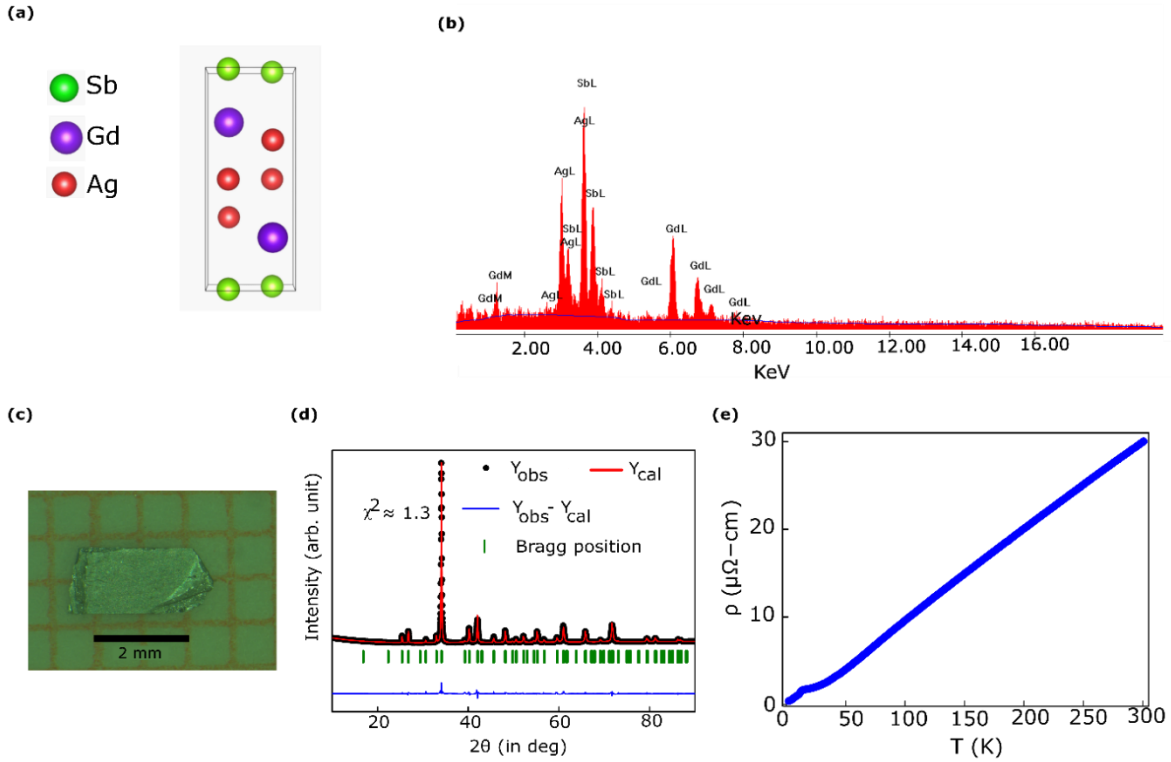

Figure 5.1 (**a**) The schematically drawn crystal structure of $GdAgSb_2$ **(b)** The EDAX/ EDX spectroscopy data on a randomly selected area of a grown single crystal of $GdAgSb_2$. **(c)** The image of single crystal with scale bar. **(d)** Powder XRD pattern on the crushed single crystals for GdAgSb2. Experimental data (Yobs) are indicated by the black circles, calculated pattern (Ycal) is denoted by the red line, whereas the difference between experimental and calculated intensities (Yobs-Ycal) is marked by the blue line and the Bragg positions are shown by magenta vertical lines. **(e)** Resistivity (ρ) vs. temperature(T)

antimony. After that, we get 1mm thick $GdAgSb_2$ with 3 to 4 mm long single crystal (see

[4] The single crystal was grown by Shubhankar Roy under the supervision of Prof. Prabhat Mandal, SINP, Kolkata.

Figure 5.1c).The energy dispersive x-ray spectroscopy (EDX) (see **Figure 5.1b**) is utilized to check the elemental stoichiometry and homogeneity of the crystal. We found an almost exact ratio and a 5% error. To characterize the single crystal, we use a high-resolution Rigaku X-ray diffractometer (TTRAX III) for X-ray diffraction (XRD) (the XRD data is plotted in **Figure 5.1d**). The crystal is crushed to make powder for powder x-ray diffraction. No impurity peak is found. Next, to characterized the system we measured resistivity as a function of temperature (see **Figure 5.1e)**. Below the critical temperature (Neel temperature), T_N, a sudden decline in resistivity is observed, attributed to the reduction of spin-disorder scattering linked with the transition from a paramagnetic to an antiferromagnetically ordered state. The exceedingly low value of ρ_{xx} (approximately $^{0}.38\ \mu\Omega$ cm) at 2 K, coupled with a notably high residual resistivity ratio (RRR=$\rho_{xx}^{300\ K}/\rho_{xx}^{2\ K}$), ~ 8^{0}, establishes the superior quality of the single crystal and its commendable metallic nature. Beyond T_N, the resistivity ρ_{xx} exhibits nearly linear behaviour with temperature, indicating the increasing dominance of electron-phonon scattering in charge transport within the paramagnetic phase.

5.2.2 Magnetization:

To comprehend the magnetic property of this system, magnetic susceptibility measurement as

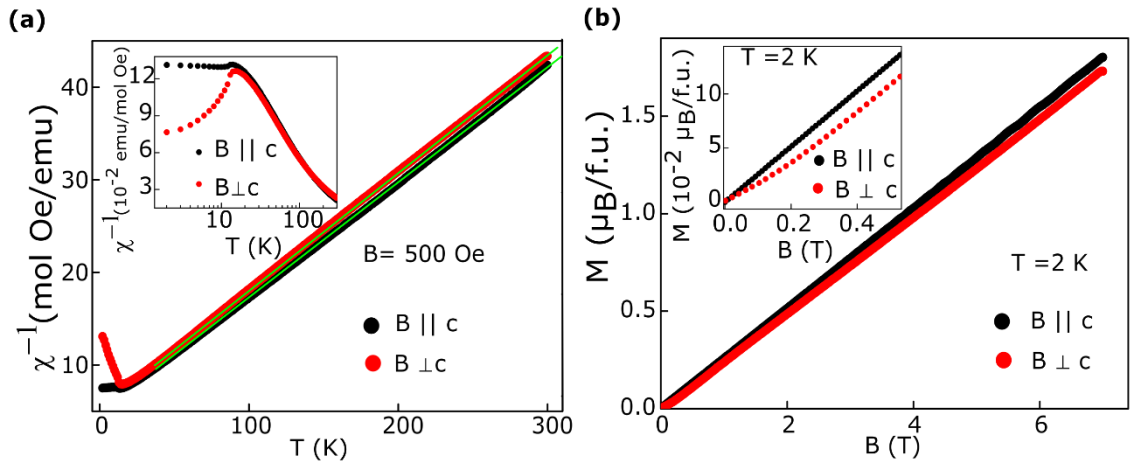

Figure 5.2 (a) Inverse susceptibility vs temperature with B (=500 Oe) || c and B⊥ c (with inset showing zoomed image near the anti-ferromagnetic phase transitions.) **(b)** The magnetization vs magnetic field at T=2 K.

a function of temperature is conducted. It was done in two configurations, one parallel and another perpendicular to the c-axis. In both arrangements, the susceptibility χ grows in amplitude with a reduction of temperature. At the anti-ferromagnetic transition, a reduction χ is observed in both configurations (displayed in **Figure 5.2a**). Above T_N, the susceptibility data taken for both configurations show similar values. Linear variation of χ^{-1} with temperature

indicates that the crystal field splitting of the Gd ion is not present. As the magnetic field a parameter, the magnetization is measured with both arrangements and the result is displayed in **Figure 5.2b.** The magnetization evolves linearly with the magnetic field. The value of M at 2 K and 9 T is 1.9 μ_B /Gd, which is about 27% of the spin-only moment of Gd^{3+}ion (7 μ_B). Nevertheless, with regards to B⊥c, an indication of a subtle ascending curvature becomes apparent within the low magnetic field region, as shown in the inset of **Figure 5.2b**. This distinct behaviour implies the presence of an extended metamagnetic-like transition within the compound $GdAgSb_2$.

5.2.3 De Haas-van Alphen oscillations:

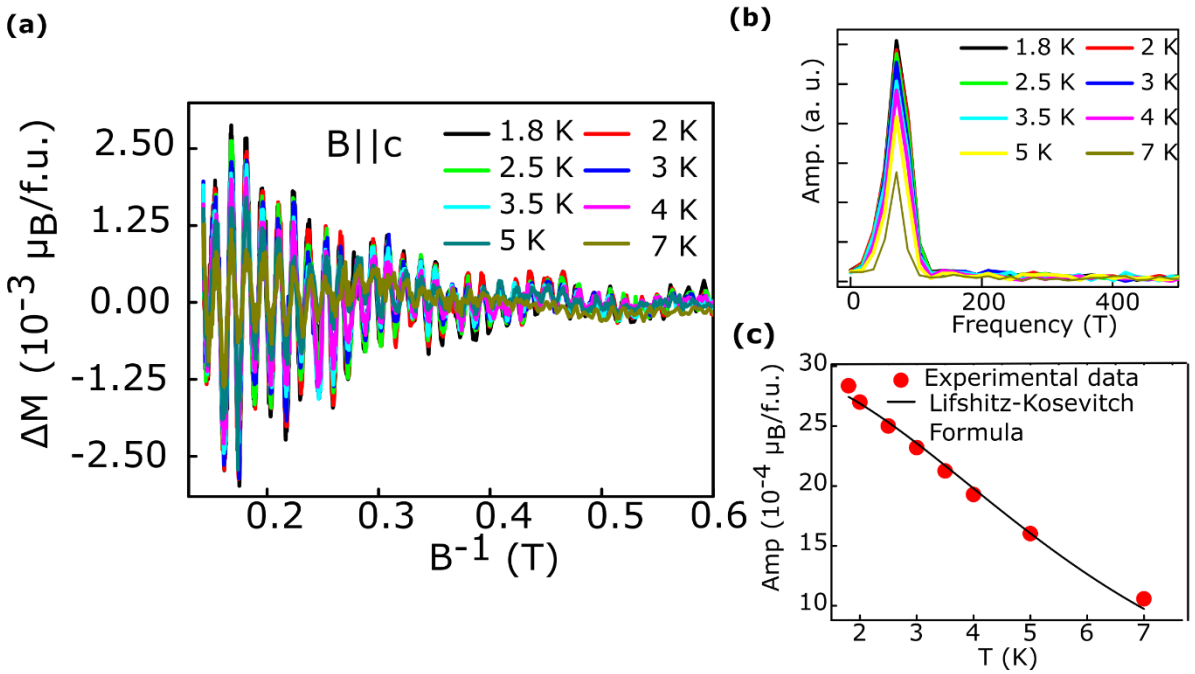

Figure 5.3: (a) Oscillating part of the magnetization, M vs 1/B (dHvA effect) for magnetic field along the c direction **(b)** Fast Fourier transform which shows Oscillation frequency at 70 T that is found from the dHvA effect. **(c)** The oscillation amplitude as a function of temperature is fitted using the thermal damping factor of Lifshitz-Kosevich formula, $R_T = \frac{2\pi^2 k_B T}{\beta} / \sinh\left(\frac{2\pi^2 k_B T}{\beta}\right)$, where $\beta = \frac{e\hbar B}{m^*}$.

Figure 5.3a illustrates a distinctive oscillatory pattern of the magnetization (denoted as ΔM) with the reciprocal of the magnetic field strength (1/B) for $GdAgSb_2$, manifested as the de Haas-van Alphen (dHvA) effect[114]. The amplitude of such quantum oscillation decreases rapidly with the increase of temperature. Fast-Fourier transform (FFT) of the oscillatory data unravels a singular frequency of approximately 70 T, as depicted in the inset of **Figure 5.3b**). Utilising the Onsager relationship, we derived further an estimate for the Fermi surface cross-section perpendicular to the applied magnetic field direction, yielding a value of 6.68×10^{-3} Å^{-}

[2]. The discernible presence of the dHvA oscillation persists up to 7 K (see **Figure 5.3a**). The temperature-dependent attenuation of the oscillation amplitude has been fitted using the Lifshitz-Kosevich equation[202](see **Figure 5.3c**) Extracting parameters from this fitting process, the cyclotron's effective mass is gauged to be approximately 0.17 times the rest mass of a free electron.

5.2.4 Electronic and magneto transport:

Furthermore, we examine the magnetoresistance and Hall effect across different temperatures under the influence of constant magnetic fields along the c-axis. As illustrated, the transverse MR demonstrates a monotonically increasing trend with the magnetic field, devoid of any discernible saturation characteristics. At a temperature of 2 K and a magnetic field strength of 9 T, the MR attains a value of approximately 1.6×10^3%, comparable to observations in various Dirac and Weyl systems. Notably, as temperature rises, the MR experiences a rapid decline. The longitudinal and transverse conductivity for two band system are shown below[42,88]:

$$\sigma_{xy}(B) = [n_e\mu_e^2 \frac{1}{1+(\mu_e B)^2} - n_h\mu_h^2 \frac{1}{1+(\mu_h B)^2}]eB \text{.....5.1}$$

$$\sigma_{xx}(B) = e\left[\frac{n_h\mu_h}{1+(\mu_h B)^2} + \frac{n_e\mu_e}{1+(\mu_e B)^2}\right] \text{.....5.2}$$

This departure, observed in the context of the semiclassical two-band model, may find attribution to intrinsic intricacies within the material system under scrutiny. Exploring the diverse aspects of charge conduction mechanisms in $GdAgSb_2$ unveils intricacies such as the involvement of multiple charge carriers characterized by subtly distinct carrier densities. Additionally, the mobility changes with temperature, adding complexity to the overall charge conduction dynamics in transverse MR (TMR). The Hall resistivity data reinforces the notion that $GdAgSb_2$ harbours at least two distinct Fermi pockets, characterized by both electron and hole types (see **Figure 5.4c, d**). Using two-band fitting of $\sigma_{xy}(B)$ at 2 K, we have obtained the density and mobility of the hole (electron)- type carriers as $\sim 1.16\times10^{19}$ cm^{-3} (1.01×10^{19} cm^{-3}) and $\sim 1.205\times10^4$ cm^2 V^{-1}s^{-1} ($\sim 1.207\times10^4$ cm^2 V^{-1}s^{-1}), respectively, which are comparable to that reported for various topological electronic materials. (see **Figure 5.4d**). For consistency, we have shown global fitting $\sigma_{xx}(B)$ and $\sigma_{xy}(B)$ with Eq. 5.1 and 5.2 in the inset of **Figure 5.4d**. Given the nearly identical carrier densities for electrons and holes, the corresponding Fermi pockets are anticipated to possess comparable cross-sectional dimensions. This similarity presents a significant challenge in differentiating between two closely positioned frequencies in dHvA effect, particularly within the confined field range of our measurements (2-7 T). Alternatively, it is plausible that one of

the Fermi pockets align orthogonally to the direction of the applied magnetic field. Within this arrangement, a current (I) is applied along one of the crystallographic axes within the ab-plane of the plate-like crystal. The magnetic field (B) undergoes rotation from the out-of-plane (B || c-axis) position to the in-plane (B⊥ c-axis) position, as depicted in the schematic of **Figure**

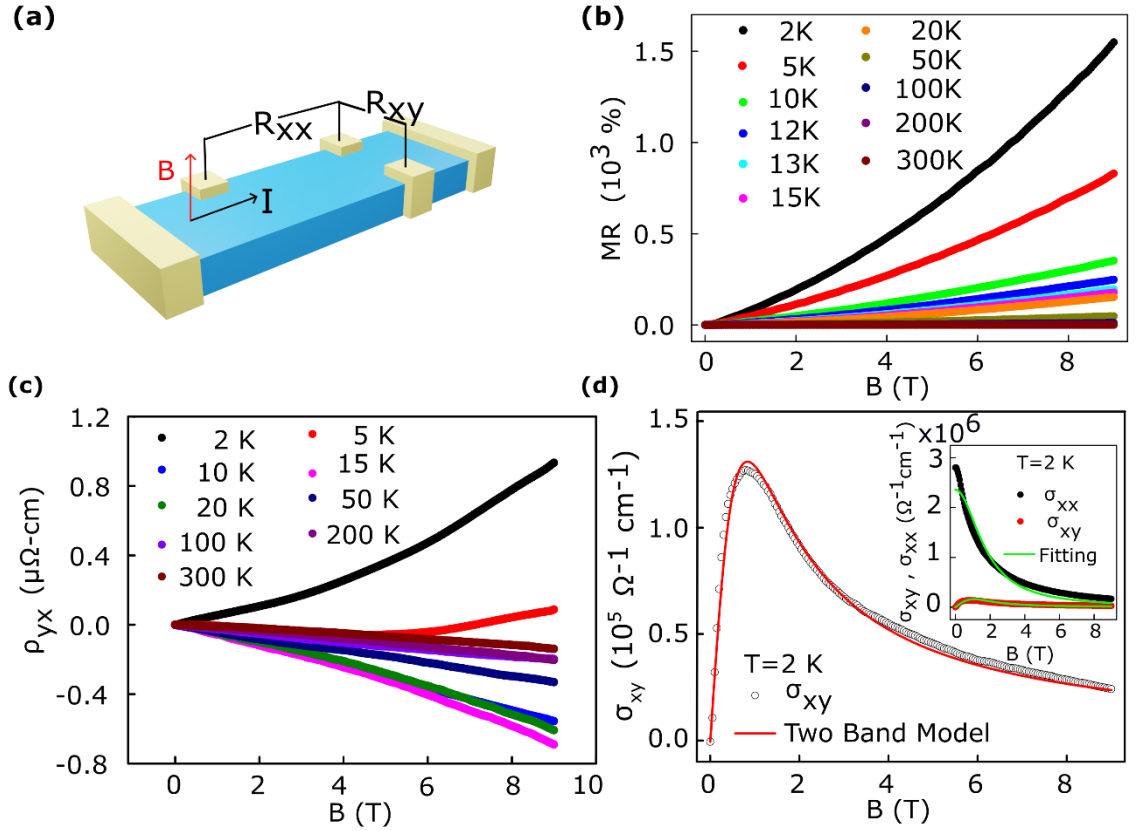

Figure 5.4 (a) The schematic diagram of the configuration of ordinary Hall and Transverse MR. **(b)** The magnetic field dependence of transverse magnetoresistance at different temperature. **(c)** The ordinary Hall resistivity vs. magnetic field at different temperature. **(d)** Two-band fitting of a representative Hall conductivity (σ_{xy}) at 2 K. Inset shows the global fitting for the electrical conductivity (σ_{xx}) and Hall conductivity (σ_{xy}) simultaneously for 2 K. two band fitting equation are Eq. 5.1 and 5.2

5.5a. The figures reveal anisotropy in the transport properties, particularly noticeable at 2 K and 9 T, where the anisotropy ratio ($\rho_{xx}^{B||c}/\rho_{xx}^{B\perp c}$) is approximately 4. The maximum MR value is observed when the magnetic field direction aligns almost parallel to the c-axis, decreasing to a minimum when the field is in the in-plane direction (θ =9º). Understanding that the charge carriers' mobility (μ) significantly influences TMR, while the scattering time (τ) and effective mass of the charge carriers (m_{eff}) collectively define mobility, it becomes evident that both μ and m_{eff} are directly linked to the Fermi surface. The first term has a direct relationship with the cross-sectional area of the Fermi surface, while the later term is associated with the curvature of the electronic band. In essence, the Fermi surface topology exerts a profound

influence on determining the angle dependence of TMR. Consequently, the anisotropy in the Fermi surface of $GdAgSb_2$ elucidates the observed anisotropy in the MR. The angle dependence of the transverse MR reveals additional peaks at 14° (194°), 50° (230°), 130° (310°), and 166°(346°). Nevertheless, as the magnetic field strength decreases and temperature increases, the height of these peaks diminishes. This peculiar behaviour may be ascribed to the geometric effects associated with the quasi-two-dimensional nature of the Fermi surface[203,204].

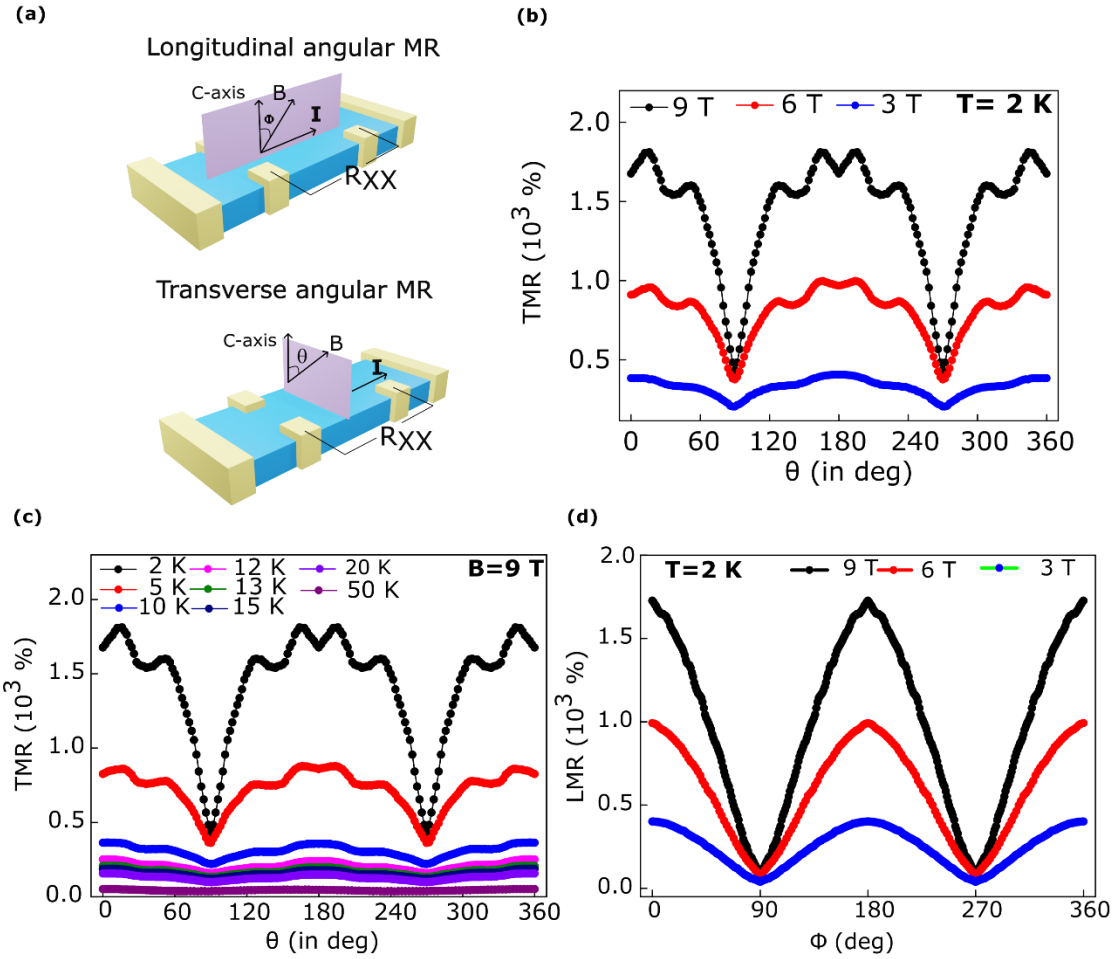

Figure 5.5: (a) The schematic diagram of measurement configuration for transverse magnetoresistance (TMR) and longitudinal magnetoresistance (LMR). **(b)** The magnetic field dependence of angular TMR at temperature T=2 K**. (c)** The temperature evolution of angular TMR with magnetic field fixed at B=9 T. (d) Angular LMR at different magnetic field at T=2 K.

Typically, at specific angles known as Yamaji angles, cyclotron orbits on the corrugated Fermi surface of high-purity layered metallic systems attain equal cross-sectional areas[204]. Consequently, the group velocity of the electrons perpendicular to the layers becomes zero, resulting in MR exhibiting a peak at those characteristic angles. Furthermore, we conducted

MR measurements in the longitudinal configuration, with the current in the ab-plane and the magnetic field rotated from parallel ($\varphi = 90°$) to perpendicular ($\varphi = 0°$) to the current direction. The schematic in **Figure 5.5a** illustrates the experimental configuration for LMR and TMR. The angle dependence of the TMR and LMR at 2 K for different magnetic field was also explored and temperature dependence of LMR and TMR(B= 9T) are also checked. At lower temperatures, ρ_{xx} (T) noticeably increases when a magnetic field is applied perpendicular to the current flow. This magnetic field-induced change, where the material shifts from metal-like to semiconductor-like behavior, is common in various topological semimetals. At lower temperatures, the MR profiles follow the Kohler scaling[205,206] ,as clearly presented in **Figure 5.6b,c** However, a subtle deviation from this scaling behaviour becomes apparent at elevated temperatures, gaining prominence beyond 100 K. The Kohler scaling, rooted in the semiclassical two-band model, asserts that MR is proportional to $(B/\rho_{xx})^m$, where m equals 2 for a perfectly compensated metal. For $GdAgSb_2$, the exponent is determined to be approximately 1.6, indicative of a system approaching compensation. Nevertheless, a noticeable departure from the scaling behaviour is evident at higher temperatures.

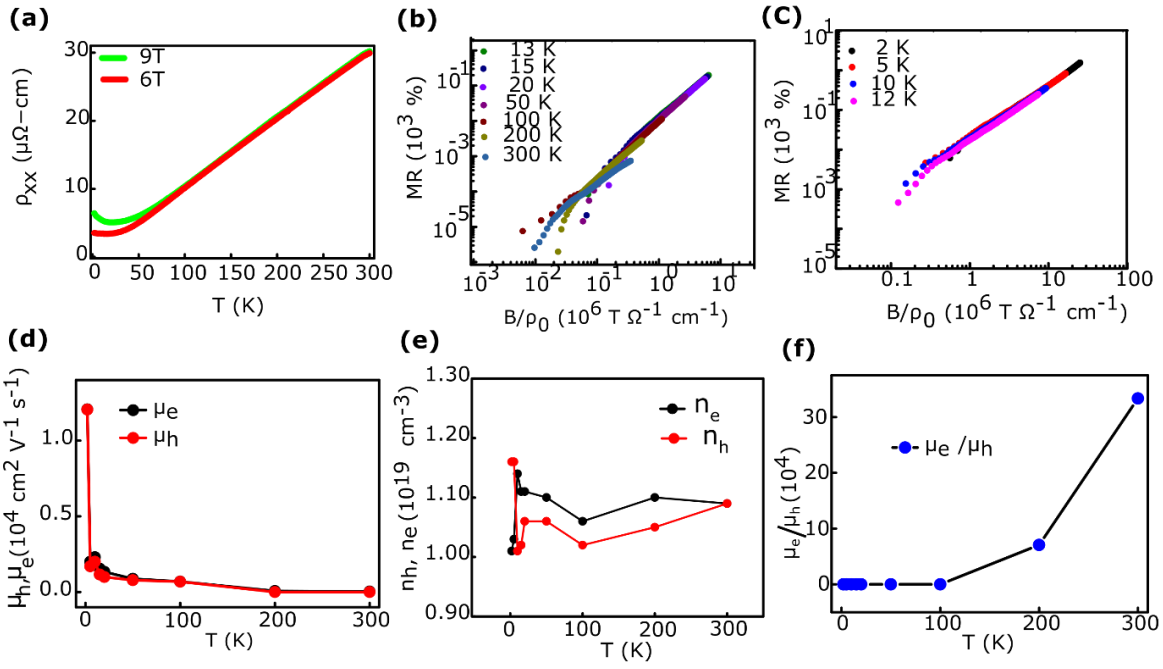

Figure 5.6: (a) The resistivity vs. temperature at different magnetic field. **(b)** The Kohler's plot for MR up to 12 K in log-log scale**. (c)** The Kohler's plot for MR at 13 K. **(d)** The temperature dependence of the mobility of electron and hole. **(e)** The temperature dependence of the carrier density of electron and hole. **(f)** The temperature dependence of μ_e/μ_h.

5.2.5 Planar Hall effect:

To identify the unique features of a potentially non-trivial electronic band, we performed a Planar Hall Effect (PHE) measurement. The angular variation of PHE and in-plane resistance follows the below mentioned equations[102,103]:

$$\rho_{xx} = \rho_{\perp} - \Delta\rho^{chiral} \cos^2\theta \quad \text{.....5.3}$$

$$\rho_{xy}^{PHE} = -\Delta\rho^{chiral} \sin\theta \cos\theta \quad \text{.....5.4}$$

Where, $\Delta\rho^{chiral} = \rho_{\perp} - \rho_{||}$

This method serves as an indirect indicator, revealing the existence of a non-vanishing Berry

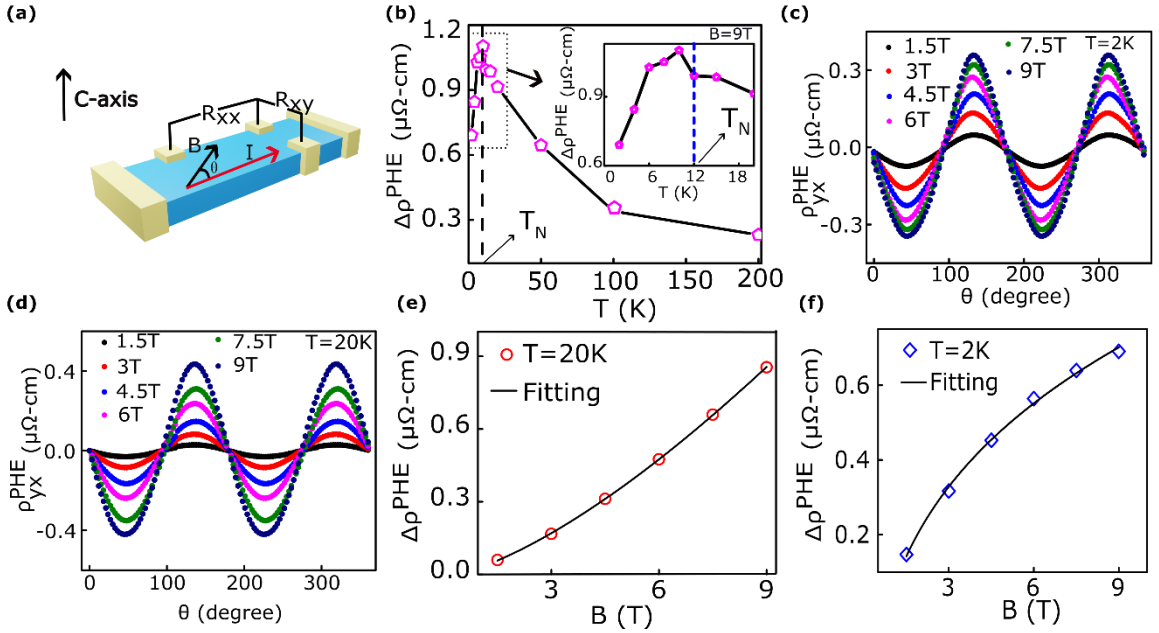

Figure 5.7: (a) The schematic of the PHE set-up **(b)** $\Delta\rho^{PHE}$ vs. temperature(T) with fixing magnetic field B=9 T. Inset showing zoomed image of the PHE amplitude around antiferromagnetic phase transition. The angular dependence of the PHE signal at different magnetic field at **(c)** T=2 K **(d)** T=20 K.

curvature inherent in topological materials. **Figure 5.7a** presents the configuration for planar Hall and planar resistivity measurement scheme. Illustrated in **Figure 5.7c** the peaks (occurring at 135° and 315°) as well as the valleys (located at 45° and 225°) of the PHE aligns harmoniously with the anticipated (PHE) manifestations expected for materials characterized by topological properties[102].

To detect the influence of magnetic ordering on PHE signal, the temperature evolution of the signal is carried out. The amplitude expansion of the at a magnetic field strength of 9 Tesla steadily increases until reaching the Neel temperature. Subsequently, there is a notable decline in magnitude as temperature decreases. Next, we checked the magnetic field dependence of PHE signal inside antiferromagnetic phase and paramagnetic phase. Inside the antiferromagnetic phase (T=2 K), $\Delta\rho_{chiral} \propto B^{1.5}$ and above, $\Delta\rho_{chiral} \propto B^{0.25}$(see **Figure 5.7 e and f**). We have shown in **Figure 5.8a** the fitting of angular ρ_{yx}^{PHE} and ρ_{xx}^{Planer} with equation 5.3 and 5.4. The $\Delta\rho_{chiral}$ is extracted using **equation 5.3 and 5.4.** The temperature dependence of $\rho_{\perp}$ also demonstrate anomaly at around the anti-ferromagnetic phase transition (see **Figure 5.8b**).The magnetic field dependence of the angular in plane resistivity is shown in **Figure 5.8c** And the in-plane AMR (**B=9 T**) as a function of temperature are shown in **Figure 5.8d**.

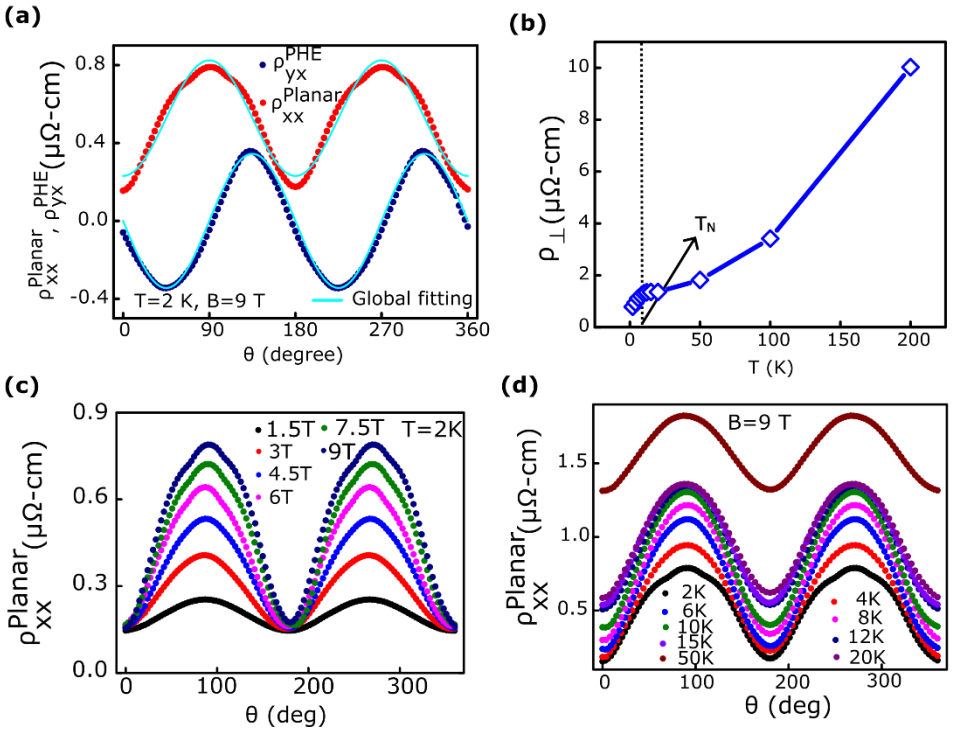

Figure 5.8: (a) Global _fittings of representative data for **(a)** ρ_{yx}^{PHE} and ρ_{xx}^{Planer} at 2 K and 9 T for $GdAgSb_2$ using Eqs. 5.3 and5.4, respectively. **(b)** The extracted $\rho_{\perp}$ vs. T plot. **(c)** The planar resistivity (ρ_{xx}^{Planer}) for $GdAgSb_2$ as a function of angle at 2 K for several magnetic fields. **(d)** The ρ_{xx}^{Planer} as a function of angle at 9 T for different temperatures.

5.3 Summary:

In summary, we successfully created single crystalline $GdAgSb_2$ and conducted comprehensive magnetic and electronic transport analyses. Noteworthy findings include a

substantial non-saturating transverse magnetoresistance and a significant anisotropy ratio in the magnetoresistance, indicating pronounced anisotropy in the Fermi surface. Additionally, distinctive peaks in the angle dependence of magnetoresistance at specific angles suggest the quasi-two-dimensional nature of the Fermi surface. Hall measurements unveiled high mobility and nearly identical densities of both electron- and hole-type carriers in $GdAgSb_2$. At low temperatures, the strong correlation with Kohler scaling implies a nearly compensated system. The dHvA oscillation showcased a small effective mass for the charge carriers. Furthermore, the planar Hall effect persisted at elevated temperatures (approximately 200 K), endorsing the potential nontrivial nature of the electronic band structure in this material. In addition to that, an anomaly in PHE signal occurs at the antiferromagnetic ordering temperature (T_N) with the PHE vs magnetic field plot shows a distinct nature below and above T_N. Our experimental findings suggest that the spin arrangement exerts an impact on the signal linked to non-trivial electronic bands.

Chapter 6

Concluding Remarks:

6.1 Conclusion:

Over the past twenty years, there has been significant progress in the realization and exploration of a novel category of materials known as topological materials. These materials are distinguished solely by their electronic band structures and underlying symmetries, giving rise to a range of universal physical phenomena regardless of specific material properties. For instance, topological insulators exhibit a bulk energy gap while maintaining a protected surface states in presence of time-reversal symmetry. This protection against back-scattering facilitates the flow of dissipation-less currents along their edges in two dimensions, while in three dimensions, they manifest topological magneto-electric effects with a quantized response. Another category, the Dirac or Weyl semi-metals, feature gapless bulk states capable of hosting relativistic chiral fermions. Identification of various topological materials has been achieved through electronic structure calculations, primarily employing effective single-particle methods. However, the inclusion of electron–electron interactions is expected to unveil more exotic phenomena. For instance, attractive electron–electron interactions might drive a Weyl semi-metal into a topological superconductor, whereas repulsive interactions could lead to incommensurate charge density waves, often accompanied by unusual axion electrodynamics.

To explore the impact of the charge or spin ordering mediated by the electronic correlation on topological transport properties in condensed matter systems, we choose two CDW systems and an antiferromagnetic system. In the chapter 1, the history and basic concept of topology, CDW and magnetism are introduced. In addition, we briefly discussed about the coexistence and competition between topology and correlation. In the chapter 2, we gave a brief overview of the measurement tools which are used to probe the transport properties. In the chapter 3, we discussed about single crystals of $LaAgSb_2$ with weak CDW modulation with possible nontrivial electronic bands. The crystal is grown using Sb flux method and characterized through EDAX elemental mapping exhibiting a good crystal quality. Furthermore, we verified the CDW formation through temperature dependent resistivity measurements. We carried out ab-initio calculation and Planar Hall effect measurement to investigate the topological properties in the system. We found that the system is trivial semimetal inside the normal phase

but the inversion symmetry is broken by the chiral CDW formation and turns the system into a tilted Weyl semi metallic phase. Planar Hall effect (PHE) measurements also reflect the CDW driven topological transition. The sign of the PHE signal changes from negative to positive when the system enters CDW phase. The PHE, TMR, LMR all show unsaturated linear evolution with magnetic field inside CDW state which are possibly Berry curvature driven effects. The indication of the Fermi surface modification is also detected through ordinary Hall effect measurement. An anomaly in the Hall resistivity is observed near the CDW transition temperature. Overall, we have demonstrated that, the chiral CDW turns a system into a topologically non-trivial system through details investigation of $LaAgSb_2$.

To dig dipper in the search of the connection between charge ordering and Berry curvature driven effects, we next choose a strong CDW system from TMDC family, 1T-TaS_2. Initially we verified the system properties through resistivity vs. temperature studies. We employed NLHE and PHE technique to detect non-vanishing Berry curvature poles. We observed that the NLHE is finite inside C-CDW state and vanishes when system enters NC-CDW state. Furthermore, we also investigate the topological nature of the different phase through the PHE measurement technique. The angular and magnetic field dependence of PHE signal inside C-CDW state exhibit usual characteristic like the topological materials. Additionally, we explored the system through Seeback effect measurement and Hall effect measurement, which reveal the modulation of the Fermi surface due to CDW. Both measurements show a change of sign due to formation of CDW. From the Hall and thermoelectric studies, we found that inside C-CDW state the majority carrier is hole while inside the NC-CDW state, the charge carrier is electron. Theoretical calculations in the C-CDW phase further indicate the presence of finite Berry curvature, justifying the observation of PHE and NLHE.

So far, we have described that charge ordering by the formation CDW, have a huge impact on nontrivial phases of the matter. To explore the effect of spin ordering on the topological behavior, we have studied the antiferromagnetic system $GdAgSb_2$, sharing similar square net crystal structure like $LaAgSb_2$. After examining the successful growth of the crystal through XRD, EDAX elemental mapping, the anti-ferromagnetic transition is confirmed through temperature dependent magnetization and resistivity measurements. The system exhibits a large and unsaturated magnetoresistance, which is a common feature of a topological semimetal. The semi-metallic nature is further verified by ordinary Hall effect measurement. De Haas–Van Alphen effect measurements exhibit a low effective mass of the carrier similar

to the topological Dirac or Weyl semimetal. Furthermore, we obtained the angular planar Hall effect like a topological material. Interestingly, we observe a different nature of the PHE amplitude vs. magnetic field dependence above and below the Neel temperature (T_N), along with an anomaly in the PHE signal near the T_N. Our findings suggest that $GdAgSb_2$ is a possible magnetic topological material where antiferromagnetic spin ordering might affect the topological properties.

6.2 Future scope of work:

The results of the thesis offer a way to probe the possible connection between correlation and topology in three different condensed matter systems. This section outlines several potential directions for extending the work.

6.2.1 Exploring the topology and correlation in semimetals

The interest in square-net materials as TSMs began with the discovery of anisotropic Dirac fermions in $SrMnBi_2$. In this layered tetragonal material ($CaSmP_2$-type, space group I4/mmm), Mn and Bi each form square nets with relatively small atomic spacing. These densely packed square nets are commonly referred to as the 4^4 -net in the crystallography literature. Materials with square-net lattice also offer an excellent opportunity to explore complex electronic states, as superconductivity, charge density waves, heavy fermion, and magnetism, which often coexist within a single material. In chapter 3, we have demonstrated a coexistence and interplay of CDW and topology in one of the square-net system $LaAgSb_2$. However, at very low temperature (T~ 3^{00} mK), $LaAgSb_2$ exhibits a superconducting transition. Investigating the coexistence of superconductivity, topology, and CDWs is another aspect to explore in this system. Furthermore, the chiral nature of the CDW in the system can be probed through second harmonic generation and non-linear Hall effect studies. The out of plane magneto transport (applied current along c-axis) in $LaAgSb_2$ is another aspect to investigate as there is a linear tilted band present in the system along k_z axis.

Moreover, there are several other systems with similar structure exhibiting correlated states like charge density waves and superconductivity. Layered CDW systems like RTe_3 (*R*=La, Sm, Gd, Tb, Dy, Ho, Er, Tm) and *Ln*SbTe (Ln=La, Ce, Sm, Gd) have shown great potential for exploring many body physics. One can explore the origin of CDW formation and its connection

to topology by using a combination of volume optimization and transport methods sensitive to the Berry curvature in those square net systems.

6.2.2 Topology and correlation in low temperature Phases of 1T-TaS_2

In Chapter 4, we demonstrate the impact of the formation of the commensurate - CDW of the bulk TMDC 1T-TaS_2. In experiments, C-CDW phase of 1T-TaS_2 demonstrates a star-of-David pattern with a $\sqrt{13} \times \sqrt{13}$ periodicity in the single layer of this system. Within each unit cell, 12 out of 13 Ta ions gather, resulting in a CDW band gap. But, in the bulk of this system, there are two stable layer stacking orders with metallic and insulating properties. Here, we focused on the metallic or semi-metallic AL stacking order within the C-CDW state ($T > 9^{o}$ K), which exhibits nontrivial phases. However, the low-temperature L stacking also hosts complex phases, such as Mott insulator and quantum spin liquid, featuring a single s=1/2 orphan spin from a Ta atom. Despite the use of various experimental techniques such as magnetization, muon spin relaxation (μSR), polarized neutron diffraction measurements, and nuclear quadrupole resonance (NQR), the behavior of this low-temperature state remains elusive. A possible future research direction could be to explore the effect of the orphan spin at very low temperatures using magneto-transport and Berry curvature-sensitive methods. A single layer of 1T-TaS_2 is believed to be a Mott insulator below 5^{o} K. In bulk, out-of-plane hopping of charge carriers causes the Mott insulating phase to disappear. The system's properties below 5^{o} K are highly sensitive to the number of layers, making 1T-TaS_2 particularly interesting for studying layer-dependent topological properties.

6.2.3 Effect of spin order and topology

In chapter 5, we have discussed how the PHE and magnetization measurement technique can be used to detect the effect of topological band of an antiferromagnetic system $GdAgSb_2$. Our results suggest a possible connection between spin ordering and topological properties. Various types of magnetic ordering, such as ferromagnetism, antiferromagnetism, frustrated magnetism, spin liquids, and spin ices, can be explored to investigate the interplay between these magnetic orderings and topological features. Especially, the system with highly degenerate spin configuration shows a huge potential for studying topological properties. Similar to the frustrated magnets, competing interactions that prevent a simple spin alignment, often lead to a highly degenerate ground state. The frustration can enhance quantum fluctuations, potentially giving rise to topological magnetic states with novel quasiparticles. Spin liquids can harbor fractionalized excitations and anyons, which are deeply tied to the topological nature of the spin liquid state. Along with the effective magnetic monopoles

emerging in spin ices can interact with topological properties, offering a playground for studying emergent topological phenomena.

References:

1. Klitzing, K. V, Dorda, G. & Pepper, M. New Method for High-Accuracy Determination of the Fine-Structure Constant Based on Quantized Hall Resistance. *Phys Rev Lett* **45**, (1980).
2. Fu, L. & Kane, C. L. Topological insulators with inversion symmetry. *Phys Rev B Condens Matter Mater Phys* **76**, 1–17 (2007).
3. Kane, C. L. & Mele, E. J. Quantum Spin hall effect in graphene. *Phys Rev Lett* **95**, 1–4 (2005).
4. Hasan, M. Z. & Kane, C. L. Colloquium: Topological insulators. *Rev Mod Phys* **82**, 3045–3067 (2010).
5. Fu, L., Kane, C. L. & Mele, E. J. Topological insulators in three dimensions. *Phys Rev Lett* **98**, 1–4 (2007).
6. Avron, J. E., Osadchy, D. & Seiler, R. A Topological Look at the Quantum Hall Effect. *Phys Today* **56**, 38–42 (2003).
7. Shen, S.-Q. *Topological Insulators*. vol. 174 (Springer, 2012).
8. Landau, L. D. On the theory of phase transitions. *Zh. eksp. teor. Fiz* **7**, 926 (1937).
9. Falk, F. Landau theory and martensitic phase transitions. *Le Journal de Physique Colloques* **43**, C4-3 (1982).
10. Von Klitzing, K. *The Quantized Hall Effect»*.
11. Mikitik, G. P. & Sharlai, Y. V. Manifestation of berry's phase in metal physics. *Phys Rev Lett* **82**, 2147–2150 (1999).
12. Liu, B. & Zhang, W. Research Progress of Topological Quantum Materials: From First-Order to Higher-Order. *Symmetry* vol. 15 Preprint at https://doi.org/10.3390/sym15091651 (2023).
13. Ryu, S. & Hatsugai, Y. Entanglement entropy and the Berry phase in the solid state. *Phys Rev B Condens Matter Mater Phys* **73**, 1–10 (2006).
14. Hasan, M. Z. & Kane, C. L. Colloquium: Topological insulators. *Rev Mod Phys* **82**, 3045–3067 (2010).
15. König, M. *et al. Quantum Spin Hall Insulator State in HgTe Quantum Wells*. *Semicond. Sci. Technol* vol. 45 https://www.science.org (1980).
16. Chang, C.-Z. *et al. Experimental Observation of the Quantum Anomalous Hall Effect in a Magnetic Topological Insulator*. vol. 340 https://www.science.org (2013).
17. Hsieh, D. *et al.* A topological Dirac insulator in a quantum spin Hall phase. *Nature* **452**, 970–974 (2008).
18. Chen, Y. L. *et al. Experimental Realization of a Three-Dimensional Topological Insulator, Bi 2 Te 3*. https://www.science.org.
19. Zhang, H. *et al.* Topological insulators in Bi 2 Se 3, Bi 2 Te 3 and Sb 2 Te 3 with a single Dirac cone on the surface. *Nat Phys* **5**, 438–442 (2009).
20. Topological, T. *et al.* Experimental Realization of a Three-Dimensional Topological Insulator, Bi2Te3. **178**, 1–4 (2009).
21. Novoselov, K. S. *et al. Electric Field Effect in Atomically Thin Carbon Films*. *Phys. Rev. Lett* vol. 404 www.arXiv.org/quant-ph/ (2000).
22. Xia, Y. *et al.* Observation of a large-gap topological-insulator class with a single Dirac cone on the surface. *Nat Phys* **5**, 398–402 (2009).
23. Chen, G. *et al.* Signatures of tunable superconductivity in a trilayer graphene moiré superlattice. *Nature* **572**, 215–219 (2019).
24. Park, J. M., Cao, Y., Watanabe, K., Taniguchi, T. & Jarillo-Herrero, P. Tunable strongly coupled superconductivity in magic-angle twisted trilayer graphene. *Nature* **590**, 249–255 (2021).
25. Wang, Z. *et al.* Dirac semimetal and topological phase transitions in A 3Bi (A=Na, K, Rb). *Phys Rev B Condens Matter Mater Phys* **85**, (2012).

26. Liu, Z. K. *et al. Discovery of a Three-Dimensional Dirac Semimetal, Na3Bi. 21 FEBRUARY* vol. 343 www.sciencemag.org (2014).
27. Xu, C. *et al.* Evidence for the chiral anomaly in the Dirac semimetal Na3Bi. *Nat Mater* **14**, 1135–1141 (2015).
28. Liu, Z. K. *et al.* A stable three-dimensional topological Dirac semimetal Cd3 As2. *Nat Mater* **13**, 677–681 (2014).
29. Li, H. *et al.* Negative magnetoresistance in Dirac semimetal Cd3As2. *Nat Commun* **7**, (2016).
30. Pan, H. *et al.* Quantum oscillation and nontrivial transport in the Dirac semimetal Cd3As2 nanodevice. *Appl Phys Lett* **108**, (2016).
31. Dirac, P. A. M. The Quantum Theory of the Electron. *Proceedings of the Royal Society of London. Series A, Containing Papers of a Mathematical and Physical Character* **117**, 610–624 (1928).
32. H. Weyl. PHYSICS: H. WEYL"Electron and gravitation," Z. Phys. 56, 330–352 1929 Surv. High Energy Phys. English translation 5, 261–267 1986 . *PRoc. N. A. S.* **56**, 330–352 (1929).
33. Zak. *Berry's Phase for Energy Bands in Solids*. vol. 62 (1989).
34. Wan, X., Turner, A. M., Vishwanath, A. & Savrasov, S. Y. Topological semimetal and Fermi-arc surface states in the electronic structure of pyrochlore iridates. *Phys Rev B Condens Matter Mater Phys* **83**, (2011).
35. Silaev, M. A. & Volovik, G. E. Topological Fermi arcs in superfluid 3He. *Phys Rev B Condens Matter Mater Phys* **86**, (2012).
36. Nielsen, H. B. *THE ADLER-BELL-JACKIW ANOMALY AND WEYL FERMIONS IN A CRYSTAL. PHYSICS LETTERS* vol. 130 (1983).
37. Tamai, A. *et al.* Fermi arcs and their topological character in the candidate type-II Weyl semimetal MoTe2. *Phys Rev X* **6**, (2016).
38. Soluyanov, A. A. *et al.* Type-II Weyl semimetals. *Nature* **527**, 495–498 (2015).
39. Lv, B. Q. *et al.* Experimental discovery of weyl semimetal TaAs. *Phys Rev X* **5**, (2015).
40. Huang, S. M. *et al.* A Weyl Fermion semimetal with surface Fermi arcs in the transition metal monopnictide TaAs class. *Nat Commun* **6**, (2015).
41. Ma, D., Jiang, H., Liu, H. & Xie, X. C. Planar Hall effect in tilted Weyl semimetals. *Phys Rev B* **99**, (2019).
42. Ashcroft, N. W. & Mermin, N. D. *Solid State Physics*. (Holt, Rinehart and Winston, 1976).
43. Kim, H. J. *et al.* Dirac versus weyl fermions in topological insulators: Adler-Bell-Jackiw anomaly in transport phenomena. *Phys Rev Lett* **111**, (2013).
44. Huang, X. *et al.* Observation of the chiral-anomaly-induced negative magnetoresistance: In 3D Weyl semimetal TaAs. *Phys Rev X* **5**, (2015).
45. Li, H., Wang, H. W., He, H., Wang, J. & Shen, S. Q. Giant anisotropic magnetoresistance and planar Hall effect in the Dirac semimetal Cd3As2. *Phys Rev B* **97**, (2018).
46. Li, P. *et al.* Evidence for topological type-II Weyl semimetal WTe2. *Nat Commun* **8**, (2017).
47. Soluyanov, A. A. *et al.* Type-II Weyl semimetals. *Nature* **527**, 495–498 (2015).
48. Jiang, J. *et al.* Signature of type-II Weyl semimetal phase in MoTe 2. *Nat Commun* **8**, (2017).
49. Jiang, Q. *et al.* Revealing Fermi surface evolution and Berry curvature in an ideal type-II Weyl semimetal. *Nat Commun* **15**, (2024).
50. Wang, H. & Qian, X. Ferroelectric nonlinear anomalous Hall effect in few-layer WTe2. *NPJ Comput Mater* **5**, (2019).
51. Du, Z. Z., Wang, C. M., Lu, H. Z. & Xie, X. C. Band Signatures for Strong Nonlinear Hall Effect in Bilayer WTe2. *Phys Rev Lett* **121**, 1–6 (2018).
52. Kang, K., Li, T., Sohn, E., Shan, J. & Mak, K. F. Nonlinear anomalous Hall effect in few-layer WTe 2. *Nature Materials* vol. 18 324–328 Preprint at https://doi.org/10.1038/s41563-019-0294-7 (2019).
53. Zhang, Y., Sun, Y. & Yan, B. Berry curvature dipole in Weyl semimetal materials: An ab initio study. *Phys Rev B* **97**, (2018).
54. Jiang, B. *et al.* Antisymmetric Seebeck Effect in a Tilted Weyl Semimetal. *Phys Rev Lett* **129**, (2022).
55. Ma, D., Jiang, H., Liu, H. & Xie, X. C. Planar Hall effect in tilted Weyl semimetals. *Phys Rev B* **99**, 1–7 (2019).

56. Das, K. & Agarwal, A. Linear magnetochiral transport in tilted type-I and type-II Weyl semimetals. *Phys Rev B* **99**, (2019).
57. Fulde, P., Thalmeier, P. & Zwicknagl, G. Strongly correlated electrons. in *Solid State Physics - Advances in Research and Applications* vol. 60 1–180 (Academic Press Inc., 2006).
58. Grüner, G. The dynamics of charge-density waves. *Rev Mod Phys* **60**, 1129–1181 (1988).
59. Grüner, G. The dynamics of spin-density waves. *Synth Met* **43**, 3767–3773 (1991).
60. Rossnagel, K. On the origin of charge-density waves in select layered transition-metal dichalcogenides. *Journal of Physics Condensed Matter* **23**, (2011).
61. Zhu, X., Guo, J., Zhang, J. & Plummer, E. W. Misconceptions associated with the origin of charge density waves. *Advances in Physics: X* vol. 2 622–640 Preprint at https://doi.org/10.1080/23746149.2017.1343098 (2017).
62. Chen, C. W., Choe, J. & Morosan, E. Charge density waves in strongly correlated electron systems. *Reports on Progress in Physics* **79**, 84505 (2016).
63. Arguello, C. J. *et al.* Visualizing the charge density wave transition in 2H - NbSe2 in real space. *Phys Rev B Condens Matter Mater Phys* **89**, (2014).
64. Soumyanarayanan, A. *et al.* Quantum phase transition from triangular to stripe charge order in NbSe2. *Proc Natl Acad Sci U S A* **110**, 1623–1627 (2013).
65. Zhu, X., Cao, Y., Zhang, J., Plummer, E. W. & Guo, J. Classification of charge density waves based on their nature. *Proc Natl Acad Sci U S A* **112**, 2367–2371 (2015).
66. Weber, F. *et al.* Extended phonon collapse and the origin of the charge-density wave in 2H-NbSe2. *Phys Rev Lett* **107**, (2011).
67. Johannes, M. D. & Mazin, I. I. Fermi surface nesting and the origin of charge density waves in metals. *Phys Rev B Condens Matter Mater Phys* **77**, (2008).
68. Johannes, M. D. & Mazin, I. I. Fermi surface nesting and the origin of charge density waves in metals. *Phys Rev B Condens Matter Mater Phys* **77**, (2008).
69. Calandra, M., Mazin, I. I. & Mauri, F. Effect of dimensionality on the charge-density wave in few-layer 2 H-NbSe2. *Phys Rev B Condens Matter Mater Phys* **80**, (2009).
70. *PHYSICAL REVIEW LETTERS*.
71. Du, C.-H. *et al. X-Ray Scattering Studies of 2H-NbSe 2 , a Superconductor and Charge Density Wave Material, under High External Magnetic Fields*. *J. Phys.: Condens. Matter* vol. 12 (2000).
72. Jerome, D., Rice, T. M. & Kohn, W. *Excitonic Insulator*. PHYSICAL REVIEW* vol. 158.
73. Tudy, C. O. A. B. I. S. & Naudé, F. Stability of polyatomic molecules in degenerate electronic states - I—Orbital degeneracy. *Proc. R. Soc. London* **161**, 220–235 (1937).
74. Mattis, D. C. *The Theory of Magnetism I: Statics and Dynamics*. (Springer Berlin Heidelberg, 2012).
75. Gooth, J. *et al.* Axionic charge-density wave in the Weyl semimetal (TaSe4)2I. *Nature* **575**, 315–319 (2019).
76. Song, T. *et al.* Unconventional superconducting quantum criticality in monolayer WTe2. *Nat Phys* **20**, 269–274 (2024).
77. Qi, Y. *et al.* Superconductivity in Weyl semimetal candidate MoTe2. *Nat Commun* **7**, (2016).
78. Jiang, Y. X. *et al.* Unconventional chiral charge order in kagome superconductor KV3Sb5. *Nat Mater* **20**, 1353–1357 (2021).
79. Tan, H., Liu, Y., Wang, Z. & Yan, B. Charge Density Waves and Electronic Properties of Superconducting Kagome Metals. *Phys Rev Lett* **127**, 46401 (2021).
80. Zhou, L. *et al.* Surface-induced positive planar Hall effect in topological Kondo insulator SmB6 microribbons. *Phys Rev B* **99**, (2019).
81. Xiang, Z. *et al.* Hall Anomaly, Quantum Oscillations and Possible Lifshitz Transitions in Kondo Insulator YbB12: Evidence for Unconventional Charge Transport. *Phys Rev X* **12**, (2022).
82. Designed The Research; S, S. P. D. Giant spontaneous Hall effect in a nonmagnetic Weyl-Kondo semimetal. (2021) doi:10.1073/pnas.2013386118/-/DCSupplemental.y.
83. Guo, C. Y. *et al.* Evidence for Weyl fermions in a canonical heavy-fermion semimetal YbPtBi. *Nat Commun* **9**, (2018).
84. Mitsuishi, N. *et al.* Switching of band inversion and topological surface states by charge density wave. *Nat Commun* **11**, (2020).

85. Liu, E. *et al.* Giant anomalous Hall effect in a ferromagnetic kagome-lattice semimetal. *Nat Phys* **14**, 1125–1131 (2018).
86. Shang, T. *et al.* Anomalous Hall resistivity and possible topological Hall effect in the EuAl4 antiferromagnet. *Phys Rev B* **103**, (2021).
87. Shi, X. *et al.* Observation of Dirac-like band dispersion in LaAgSb2. *Phys Rev B* **93**, 1–5 (2016).
88. Wang, K. & Petrovic, C. Multiband effects and possible Dirac states in LaAgSb 2. *Phys Rev B Condens Matter Mater Phys* **86**, 1–7 (2012).
89. Fichera, B. T. *et al.* Second harmonic generation as a probe of broken mirror symmetry. *Phys Rev B* **101**, (2020).
90. Zhao, Y. *et al.* Spectroscopic visualization and phase manipulation of chiral charge density waves in 1T-TaS2. *Nat Commun* **14**, 1–9 (2023).
91. Nagaosa, N., Sinova, J., Onoda, S., MacDonald, A. H. & Ong, N. P. Anomalous Hall effect. *Rev Mod Phys* **82**, 1539–1592 (2010).
92. Hall, E. H. *On a New Action of the Magnet on Electric Currents*. *Source: American Journal of Mathematics* vol. 2 https://www.jstor.org/stable/2369245 (1879).
93. Zhang, Y. *et al.* Strong anisotropic anomalous Hall effect and spin Hall effect in the chiral antiferromagnetic compounds Mn3X (X=Ge, Sn, Ga, Ir, Rh, and Pt). *Phys Rev B* **95**, (2017).
94. Zuniga-Cespedes, B. E. *et al.* Observation of an anomalous Hall effect in single-crystal Mn3Pt. *New J Phys* **25**, (2023).
95. Hayashi, H. *et al.* Large anomalous Hall effect observed in the cubic-lattice antiferromagnet Mn3Sb with kagome lattice. *Phys Rev B* **108**, (2023).
96. Pan, Y. *et al.* Giant anomalous Nernst signal in the antiferromagnet YbMnBi2. *Nat Mater* **21**, 203–209 (2022).
97. Ren, Z. *et al.* Plethora of tunable Weyl fermions in kagome magnet Fe3Sn2 thin films. *NPJ Quantum Mater* **7**, (2022).
98. Ma, J. *et al. P H Y S I C S Spin Fluctuation Induced Weyl Semimetal State in the Paramagnetic Phase of EuCd 2 As 2*. https://www.science.org (2019).
99. Lv, X., Chen, X., Zhang, B., Jiang, P. & Zhong, Z. Thickness-Dependent Magnetism and Topological Properties of EuSn2As2. *ACS Applied Electronic Materials* vol. 4 3212–3219 Preprint at https://doi.org/10.1021/acsaelm.2c00414 (2022).
100. Riberolles, S. X. M. *et al.* Magnetic crystalline-symmetry-protected axion electrodynamics and field-tunable unpinned Dirac cones in EuIn2As2. *Nat Commun* **12**, (2021).
101. Sharma, V., Nepal, R. & Budhani, R. C. Planar Hall effect and anisotropic magnetoresistance in thin films of the chiral antiferromagnet Mn3Sn. *Phys Rev B* **108**, 1–10 (2023).
102. Burkov, A. A. Giant planar Hall effect in topological metals. *Phys Rev B* **96**, (2017).
103. Nandy, S., Sharma, G., Taraphder, A. & Tewari, S. Chiral Anomaly as the Origin of the Planar Hall Effect in Weyl Semimetals. *Phys Rev Lett* **119**, (2017).
104. Wang, L. *et al.* Tuning magnetotransport in a compensated semimetal at the atomic scale. *Nat Commun* **6**, 8892 (2015).
105. Pippard, A. B. *Magnetoresistance in Metals*. (Cambridge University Press, 1989).
106. Bulgadaev, S. A. & Kusmartsev, F. V. Large linear magnetoresistivity in strongly inhomogeneous planar and layered systems. *Physics Letters, Section A: General, Atomic and Solid State Physics* **342**, 188–195 (2005).
107. Abrikosov, A. Quantum magnetoresistance. *Phys Rev B Condens Matter Mater Phys* **58**, 2788–2794 (1998).
108. Singha, R., Roy, S., Pariari, A., Satpati, B. & Mandal, P. Planar Hall effect in the type-II Dirac semimetal VAl3. *Phys Rev B* **98**, 1–6 (2018).
109. Li, L. *et al.* Higher-order oscillatory planar Hall effect in topological kagome metal. *NPJ Quantum Mater* **8**, 1–7 (2023).
110. Li, P., Zhang, C. H., Zhang, J. W., Wen, Y. & Zhang, X. X. Giant planar Hall effect in the Dirac semimetal ZrT e 5− δ. *Phys Rev B* **98**, 121108 (2018).
111. Wang, Y. *et al.* Observation of nonlinear planar Hall effect in magnetic-insulator-topological-insulator heterostructures. *Phys Rev B* **106**, (2022).
112. Liu, Q. *et al.* Nontopological origin of the planar Hall effect in the type-II Dirac semimetal NiTe2. *Phys Rev B* **99**, 1–7 (2019).

113. Meissner, W. & Ochsenfeld, R. Ein neuer effekt bei eintritt der supraleitfähigkeit. *Naturwissenschaften* **21**, 787–788 (1933).
114. J De Haas, B. W. & Van Alphen, P. M. The dependence of the susceptibility of diamagnetic metals upon the field. **33**, 1106–1118 (1930).
115. Lifshits, E. M. & Kosevich, A. M. Theory of the Shubnikov-de Haas effect. *Journal of Physics and Chemistry of Solids* **4**, 1–10 (1958).
116. T.J.Seeebeck. *Magnetische Polarisation Der Metalle Und Erze Durch Temperaturdifferenz*. (W. Engelmann, Leipzig, 1895).
117. Nyquist, H. Thermal Agitation of Electric Charge in Conductors. *Physical Review* **32**, 110–113 (1928).
118. Ocio, M., Bouchiat, H. & Monod, P. OBSERVATION OF 1/f MAGNETIC FLUCTUATIONS IN A SPIN GLASS. *Journal de physique. Lettres* **46**, 647–652 (1985).
119. Singh, A., Mukhopadhyay, S. & Ghosh, A. Tracking random walk of individual domain walls in cylindrical nanomagnets with resistance noise. *Phys Rev Lett* **105**, (2010).
120. Bid, A., Guha, A. & Raychaudhuri, A. K. Low-frequency random telegraphic noise and 1/f noise in the rare-earth manganite Pr0.63Ca0.37MnO3 near the charge-ordering transition. *Phys Rev B Condens Matter Mater Phys* **67**, 1–10 (2003).
121. Biswas, S. *et al.* Resistance fluctuation spectroscopy of thin films of 3D topological insulator BiSbTeSe1.6. *Appl Phys Lett* **115**, (2019).
122. Bora, A. & Raychaudhuri, A. K. Study of conductance fluctuations (1/f alpha noise) in metal film with electromigration stressing. *Fluctuations and Noise in Materials* **5469**, 353 (2004).
123. Raychaudhuri, A. K., Ghosh, A. & Swastik, K. A. R. Flicker noise in degenerately doped Si single crystals near the metal-insulator transition. *Pramana - Journal of Physics* **58**, 343–359 (2002).
124. Ghosh, A., Raychaudhuri, A. K., Sreekala, R., Rajeswari, M. & Venkatesan, T. Dependence of the conductivity noise of metallic oxide interconnects on the oxygen stoichiometry: A study of LaNiO3-δ. *J Phys D Appl Phys* **30**, 1–6 (1997).
125. Kar, S., Raychaudhuri, A. K., Ghosh, A., Löhneysen, H. v. & Weiss, G. Observation of non-gaussian conductance fluctuations at low temperatures in si:p(b) at the metal-insulator transition. *Phys Rev Lett* **91**, (2003).
126. Pal, A. N. *et al.* Microscopic mechanism of 1/f noise in graphene: Role of energy band dispersion. *ACS Nano* **5**, 2075–2081 (2011).
127. Scofield, J. H. ac method for measuring low-frequency resistance fluctuation spectra. *Review of Scientific Instruments* **58**, 985–993 (1987).
128. Welch, P. D. *The Use of Fast Fourier Transform for the Estimation of Power Spectra: A Method Based on Time Aver. Aging Over Short, Modified Periodograms Ik(Fn) =-I A h (%) [a k*. vol. 15 (1967).
129. Wilczek, F. Two applications of axion electrodynamics. *Phys Rev Lett* **58**, 1799 (1987).
130. Regnault, N. & Andrei Bernevig, B. Fractional Chern Insulator. *Phys Rev X* **1**, 1–14 (2011).
131. Wang, Y. *et al.* Axial Higgs mode detected by quantum pathway interference in RTe3. *Nature* **606**, 896–901 (2022).
132. Klemenz, S., Lei, S. & Schoop, L. M. Topological Semimetals in Square-Net Materials. *Annu Rev Mater Res* **49**, 185–206 (2019).
133. Singha, R., Pariari, A. K., Satpati, B. & Mandal, P. Large nonsaturating magnetoresistance and signature of nondegenerate Dirac nodes in ZrSiS. *Proc Natl Acad Sci U S A* **114**, 2468–2473 (2017).
134. Song, C. *et al.* Charge-density-wave orderings in LaAgSb2: An x-ray scattering study. *Phys Rev B Condens Matter Mater Phys* **68**, 1–6 (2003).
135. Chen, R. Y., Zhang, S. J., Zhang, M. Y., Dong, T. & Wang, N. L. Revealing Extremely Low Energy Amplitude Modes in the Charge-Density-Wave Compound LaAgSb2. *Phys Rev Lett* **118**, 1–5 (2017).
136. Singha, R. *et al.* Lattice dynamics of the topological Dirac semimetal LaAgSb2 with charge density wave ordering. *Phys Rev B* **102**, 1–12 (2020).
137. Weber, F. *et al.* Extended phonon collapse and the origin of the charge-density wave in 2H-NbSe2. *Phys Rev Lett* **107**, (2011).

138. Baek, S. H., Bud'ko, S. L., Canfield, P. C., Borsa, F. & Suh, B. J. NMR evidence for a Peierls transition in the layered square-net compound LaAgSb2. *Phys Rev B* **106**, 1–5 (2022).
139. Akiba, K., Umeshita, N. & Kobayashi, T. C. Observation of superconductivity and its enhancement at the charge density wave critical point in LaAgSb2. *Phys Rev B* **106**, 1–6 (2022).
140. Cho, K. *et al.* Using controlled disorder to probe the interplay between charge order and superconductivity in NbSe2. *Nat Commun* **9**, 1–9 (2018).
141. Baek, S. H., Sur, Y., Kim, K. H., Vojta, M. & Büchner, B. Interplay of charge density waves, disorder, and superconductivity in 2H-TaSe2elucidated by NMR. *New J Phys* **24**, 2–9 (2022).
142. Xiao, D., Chang, M. C. & Niu, Q. Berry phase effects on electronic properties. *Rev Mod Phys* **82**, 1959–2007 (2010).
143. Burkov, A. A. Giant planar Hall effect in topological metals. *Phys Rev B* **96**, 1–5 (2017).
144. Nandy, S., Taraphder, A. & Tewari, S. Berry phase theory of planar Hall effect in topological insulators. *Sci Rep* **8**, (2018).
145. Nandy, S., Sharma, G., Taraphder, A. & Tewari, S. Chiral Anomaly as the Origin of the Planar Hall Effect in Weyl Semimetals. *Phys Rev Lett* **119**, 1–6 (2017).
146. Li, P., Zhang, C. H., Zhang, J. W., Wen, Y. & Zhang, X. X. Giant planar Hall effect in the Dirac semimetal ZrT e5-δ. *Phys Rev B* **98**, (2018).
147. Kumar, N., Guin, S. N., Felser, C. & Shekhar, C. Planar Hall effect in the Weyl semimetal GdPtBi. *Phys Rev B* **98**, (2018).
148. Singha, R., Roy, S., Pariari, A., Satpati, B. & Mandal, P. Planar Hall effect in the type-II Dirac semimetal VAl3. *Phys Rev B* **98**, (2018).
149. Roy, S., Singha, R., Ghosh, A. & Mandal, P. Signature of topological nontrivial band structure in Ta3SiTe6. *Phys Rev Mater* **5**, 3–9 (2021).
150. Zheng, S. H. *et al.* Origin of planar Hall effect on the surface of topological insulators: Tilt of Dirac cone by an in-plane magnetic field. *Phys Rev B* **101**, 1–6 (2020).
151. Zhou, L. *et al.* Surface-induced positive planar Hall effect in topological Kondo insulator SmB6 microribbons. *Phys Rev B* **99**, 1–5 (2019).
152. Michel, K. H. & Verberck, B. Rigid-plane phonons in layered crystals. *Phys Status Solidi B Basic Res* **249**, 2604–2607 (2012).
153. Das, K. & Agarwal, A. Linear magnetochiral transport in tilted type-I and type-II Weyl semimetals. *Phys Rev B* **99**, 1–18 (2019).
154. Jiang, B. *et al.* Antisymmetric Seebeck Effect in a Tilted Weyl Semimetal. *Phys Rev Lett* **129**, 56601 (2022).
155. Butler, C. J., Yoshida, M., Hanaguri, T. & Iwasa, Y. Mottness versus unit-cell doubling as the driver of the insulating state in 1T-TaS2. *Nat Commun* **11**, 7–12 (2020).
156. Kratochvilova, M. *et al.* The low-temperature highly correlated quantum phase in the charge-density-wave 1T-TaS2 compound. *NPJ Quantum Mater* **2**, 1–7 (2017).
157. Darancet, P., Millis, A. J. & Marianetti, C. A. Three-dimensional metallic and two-dimensional insulating behavior in octahedral tantalum dichalcogenides. *Phys Rev B Condens Matter Mater Phys* **90**, 2–6 (2014).
158. Ngankeu, A. S. *et al.* Quasi-one-dimensional metallic band dispersion in the commensurate charge density wave of 1T-TaS2. *Phys Rev B* **96**, 1–5 (2017).
159. Gaal, R. *et al.* Interplane coupling in the quasi-two-dimensional (formula presented). *Phys Rev B Condens Matter Mater Phys* **67**, 5 (2003).
160. Ligges, M. *et al.* Ultrafast Doublon Dynamics in Photoexcited 1T - TaS2. *Phys Rev Lett* **120**, 1–5 (2018).
161. Murayama, H. *et al.* Effect of quenched disorder on the quantum spin liquid state of the triangular-lattice antiferromagnet 1T-TaS2. *Phys Rev Res* **2**, 13099 (2020).
162. Sipos, B. *et al.* From Mott state to superconductivity in-1T-TaS2. *Nat Mater* **7**, 960–965 (2008).
163. Xu, P. *et al.* Superconducting phase in the layered dichalcogenide 1T-TaS 2 upon inhibition of the metal-insulator transition. *Phys Rev B Condens Matter Mater Phys* **81**, 1–4 (2010).
164. Klanjšek, M. *et al.* A high-temperature quantum spin liquid with polaron spins. *Nat Phys* **13**, 1130–1134 (2017).
165. Law, K. T. & Lee, P. A. 1T-TaS2 as a quantum spin liquid. *Proc Natl Acad Sci U S A* **114**, 6996–7000 (2017).

166. Jiang, Y. X. *et al.* Unconventional chiral charge order in kagome superconductor KV3Sb5. *Nat Mater* **20**, 1353–1357 (2021).
167. Xiao, D., Yao, Y., Fang, Z. & Niu, Q. Berry-phase effect in anomalous thermoelectric transport. *Phys Rev Lett* **97**, (2006).
168. Nagaosa, N., Sinova, J., Onoda, S., MacDonald, A. H. & Ong, N. P. Anomalous Hall effect. *Rev Mod Phys* **82**, 1539–1592 (2010).
169. Jungwirth, T., Niu, Q. & MacDonald, A. H. Anomalous Hall Effect in Ferromagnetic Semiconductors. *Phys Rev Lett* **88**, 4 (2002).
170. Datta, B. *et al.* Nontrivial quantum oscillation geometric phase shift in a trivial band. *Sci Adv* **5**, 1–8 (2019).
171. Alexandradinata, A., Wang, C., Duan, W. & Glazman, L. Revealing the Topology of Fermi-Surface Wave Functions from Magnetic Quantum Oscillations. *Phys Rev X* **8**, (2018).
172. Sodemann, I. & Fu, L. Quantum Nonlinear Hall Effect Induced by Berry Curvature Dipole in Time-Reversal Invariant Materials. *Phys Rev Lett* **115**, (2015).
173. Franken, P. A., Hill, A. E., Peters, C. W. & Weinreich, G. Generation of optical harmonics. *Phys Rev Lett* **7**, 118–119 (1961).
174. Zhang, Y., Van Den Brink, J., Felser, C. & Yan, B. Electrically tuneable nonlinear anomalous Hall effect in two-dimensional transition-metal dichalcogenides WTe2 and MoTe2. *2d Mater* **5**, (2018).
175. Kumar, D. *et al.* Room-temperature nonlinear Hall effect and wireless radiofrequency rectification in Weyl semimetal TaIrTe4. *Nat Nanotechnol* **16**, 421–425 (2021).
176. You, J. S., Fang, S., Xu, S. Y., Kaxiras, E. & Low, T. Berry curvature dipole current in the transition metal dichalcogenides family. *Phys Rev B* **98**, (2018).
177. Hu, J. X., Zhang, C. P., Xie, Y. M. & Law, K. T. Nonlinear Hall effects in strained twisted bilayer WSe2. *Commun Phys* **5**, 1–6 (2022).
178. Ho, S. C. *et al.* Hall effects in artificially corrugated bilayer graphene without breaking time-reversal symmetry. *Nat Electron* **4**, (2021).
179. Adv Quantum Tech - 2021 - Ortix - Nonlinear Hall Effect with Time-Reversal Symmetry Theory and Material Realizations.pdf.
180. Facio, J. I. *et al.* Strongly Enhanced Berry Dipole at Topological Phase Transitions in BiTeI. *Phys Rev Lett* **121**, (2018).
181. Fazekas, P. & Tosatti, E. Electrical, structural and magnetic properties of pure and doped 1T-TaS2. *Philosophical Magazine B: Physics of Condensed Matter; Statistical Mechanics, Electronic, Optical and Magnetic Properties* **39**, 229–244 (1979).
182. Lee, S. H., Goh, J. S. & Cho, D. Origin of the Insulating Phase and First-Order Metal-Insulator Transition in 1T-TaS2. *Phys Rev Lett* **122**, (2019).
183. Butler, C. J., Yoshida, M., Hanaguri, T. & Iwasa, Y. Mottness versus unit-cell doubling as the driver of the insulating state in 1T-TaS2. *Nat Commun* **11**, (2020).
184. Wang, Y. D. *et al.* Band insulator to Mott insulator transition in 1T-TaS2. *Nat Commun* **11**, 1–7 (2020).
185. Ramsden, E. *Hall-Effect Sensors: Theory and Application*. (Elsevier Science, 2011).
186. Jonson~, M. & Mahan, D. *Mott's Formula for the Thermopower and the Wiedemann-Franz Law*. *PHYSICAL REVIEW B* vol. 21.
187. Mi, X. *et al.* Multiband effects in thermoelectric and electrical transport properties of kagome superconductors AV3Sb5 (A = K, Rb, Cs). *New J Phys* **24**, (2022).
188. Disalvo, F. J. & Waszczak, J. V. *Paramagnetic Moments and Localization in 1T-TaS2*. *PHYSICAL REVIEW B* vol. 22 (1980).
189. Kratochvilova, M. *et al.* The low-temperature highly correlated quantum phase in the charge-density-wave 1T-TaS2 compound. *NPJ Quantum Mater* **2**, (2017).
190. Ribak, A. *et al.* Gapless excitations in the ground state of 1T-TaS2. *Phys Rev B* **96**, (2017).
191. Superconductivity, A. & Ihm, J. *Berry's Phase Originated from the Broken Time-Reversal Symmetry: Theory and Application To*. vol. 67 (1991).
192. Zhao, Y. *et al.* Spectroscopic visualization and phase manipulation of chiral charge density waves in 1T-TaS2. *Nat Commun* **14**, (2023).

193. Myers, K. D. *et al. Systematic Study of Anisotropic Transport and Magnetic Properties of RAgSb (R"Y, La}Nd, Sm, Gd}Tm)*. *Journal of Magnetism and Magnetic Materials* vol. 205 (1999).
194. Andreh, G., Boureh, F., Kolenda, M., Olesh, A. & Szytu, A. *Szytu"a)*. *Physica B* vol. 292 (2000).
195. Arakane, T. *et al.* Electronic structure of LaAgSb2 and CeAgSb2 studied by high-resolution angle-resolved photoemission spectroscopy. *J Magn Magn Mater* **310**, 396–398 (2007).
196. Jobiliong, E., Brooks, J. S., Choi, E. S., Lee, H. & Fisk, Z. Magnetization and electrical-transport investigation of the dense Kondo system CeAgSb2. *Phys Rev B Condens Matter Mater Phys* **72**, (2005).
197. Myers, K. D. *et al. De Haas-van Alphen and Shubnikov-de Haas Oscillations in RAgSb 2 "RY, La-Nd, Sm….*
198. Myers, K. D., Canfield, P. C., Kalatsky, V. A. & Pokrovsky, V. L. *Angular Dependence of Metamagnetic Transitions in DyAgSb 2*.
199. Myers, K. D. *et al.* Systematic study of anisotropic transport and magnetic properties of RAgSb (R " Y , La } Nd , Sm , Gd } Tm). **205**, 27–52 (1999).
200. Ryan, D. H., Lee-Hone, N. R., Cadogan, J. M., Canfield, P. C. & Bud'ko, S. L. Magnetic ordering in GdAgSb2. *Journal of Physics Condensed Matter* **23**, (2011).
201. Song, C. *et al.* Magnetic structure of (formula presented) determined by x-ray resonant exchange scattering. *Phys Rev B Condens Matter Mater Phys* **65**, 1–4 (2002).
202. Lifshitz, I. M. & Kosevich, A. M. Theory of magnetic susceptibility in metals at low temperatures. *Sov. Phys. JETP* **2**, 636–645 (1956).
203. Mckenzie, R. H. & Moses, P. *Incoherent Interlayer Transport and Angular-Dependent Magnetoresistance Oscillations in Layered Metals*. (1998).
204. Kunihiko Yamaji. On the Angle Dependence of the Magnetoresistance in Quasi-Two Dimensional Organic Semiconductors. *J Physical Soc Japan* **58**, 1520–1523 (1989).
205. Kohler, M. Zur magnetischen Widerstandsänderung reiner Metalle. *Ann Phys* **424**, 211–218 (1938).
206. Forr, L., Biljaković, K., Cooper, J. R. & Bechgaard, K. Magnetoresistance of the organic superconductor bis- tetramethyltetraselenafulvalenium perchlorate [(TMTSF)2ClO4]: Kohler's rule. *Phys Rev B* **29**, 2839–2842 (1984).

Appendix

Flicker Noise in an Electrolyte Gated Large Area Gr-FET

Introduction:

Electronic noise is unavoidable in any electronic device, limiting its performance. Graphene, being the first 2D crystal, is known for its unique band structure and superior electronic, optical and mechanical properties. In particular, after the growth of large area graphene using chemical vapor deposition (CVD), it is possible to create wafer scale graphene device. Electrical transport and noise have been studied extensively graphene based field effect devices [1]. It is more or less understood that noise mainly originate due to the charge exchange between graphene and the interfacial traps in the graphene/SiO_2 interface [2]. Electrolyte gating is an efficient technique to induce high carrier density in a field effect configuration as the capacitance can be enormously high due to the presence of nanometer thick Debye layer at the gate-channel interface. Electronic transport and noise measurements were carried in electrolyte gated exfoliated graphene field effect transistor, however, studies on CVD based large area graphene is limited. It is important to understand whether the intrinsic defects or grain boundaries affect the noise performance in these devices.

Here, we present transport and noise characteristics of an electrolyte gated large area (~1.1×1^{04} μm^2) graphene field effect transistor. To get a noise signal from the sample, unwanted noise from measurement electronics or, other extraneous sources must be removed. This is indeed a challenging task. It is essential to choose right electronic components and a proper grounding is required to avoid any possible ground loops to reduce the extraneous noise. We have developed a lock in amplifier-based ac technique[3] to measure noise signal with proper electrical grounding. Using a lock in amplifier (MFLI, Zurich instrument), consisting of an in-built data acquisition tool we have been able to reduce the background noise to the thermal noise limit. By fabricating a graphene field effect transistor, we studied the resistance fluctuations by changing the gate voltage. The density dependence of noise indicates that the charge exchange noise from the interfacial traps, as proposed in Ref [4], is dominating in our case.

Experimental details

As discussed earlier, to optimize the noise measurement set up, noise from extraneous sources was eliminated using both hardware and software modification. The capacitive or inductive coupling from high current source was reduced by doing the measurement ins-ide a Faraday cage. The data from the Lock-in amplifier was transferred using wireless router to the computer, to further avoid any possible ground loop arising due to GPIB or USB connectors. To obtain voltage noise using ac technique [3], in-phase (X) and out-of-phase (Y) component of lock-in amplifier (LIA) is recorded over time. From the time series data, the power spectral density is calculated using digital signal processing. The in-phase compo-nent of LIA contains the noise power corresponding to the background noise as well as the noise power from the sample, and the out phase only contains the back-ground noise power, subtracting the out of phase from in phase component, the noise power spectral density of the sample is calculated, following Ref [2].

To make graphene device, commercially bought CVD graphene on a p+ doped Si/SiO_2 (3^{00} nm) (Graphenea, USA) was initially etched using standard optical lithography and oxygen plasma [3]. Electrical contact of Ti/Au (5nm/5^{0}nm) was made using optical lithography and standard electron beam deposition technique. To create ionic liquid top gate, polymer polyethylene oxide (PEO) solution, and an electrolyte, lithium-perchlorate ($LiClO_4$) was mixed with a ratio (1:8) and drop casted on graphene [5]. Fig. 1a shows the schematic of the device structure.

Results and Discussions

Fig. 1b shows the Resistance vs. Gate Voltage (V_{tg}) characteristics of the device at room temperature, measured with an ac bias current of 1μA. As shown in Fig.1b the resistance of graphene increases with gate voltage and reached maximum, when the fermi level of graphene is at the Dirac point (V_{tg} =-1.5v) and again decreases with further increase of gate voltage. The Observed hysteretic phenomena are common in GrFET which arises from charge transfer between neighbouring adsorbates (such as a water molecule) or charge injection into the trap states at the interface.

To carry out noise measurement at different carrier density, we measured noise at different

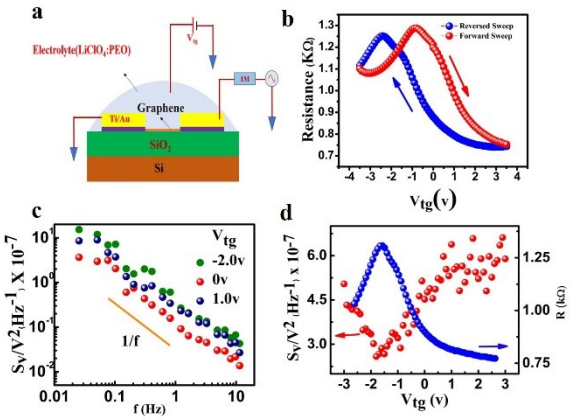

Figure 1. ***(a)*** *Top-gate measurement configuration using polymer electrolyte of GrFET.* ***(b)*** *Gate voltage characteristic of top gated GrFET.* ***(c)*** *Normalized power spectral density vs frequency of GrFET at few different gate voltages.* ***(d)*** *Normalized noise amplitude(left) and resistance(right) vs gate voltage.*

gate voltage by sweeping voltage using a Source meter (Keithley 245º). As the ionic movement is slow, we had to wait for 5 second at a particular gate voltage to measure noise at that gate voltage. Figure 2b shows the power spectral density at different V_{tg}. Throughout the measurement ranges of gate voltages, it follows $1/f^{\alpha}$, character with α varies in between º.8 to 1.1. To plot the noise magnitude with carrier density we have integrated the power spectral density over the measured frequency range and plotted as a function of V_{tg}. We observed that noise is minimum near the Dirac point and increases with density. This behavior is unusual in for a single layer graphene device [2]. This behavior also cannot be explained by the empirical Hooge's model, according to which, the noise should inversely be proportional to carrier numbers in the channel. The observed behaviour is similar to exfoliated graphene field effect device with electrolyte top gate, where an augmented charge noise model was proposed to explain the data [5]. Two mechanisms of noise were proposed for Gr-FET in Ref [2]: Charge exchange noise and charge configuration noise. According to first mechanism, noise originates from the correlated number and mobility fluctuations due to the trapping and de-trapping processes between graphene and the Noise in these systems mainly originate from the graphene and interfacial traps. Whereas, charge configuration noise arises due to the charge exchange process between the traps, without changing any carrier density in graphene. For exfoliated sample on a substrate, it was found that configuration noise dominates, while for suspended graphene device, a dip near the CNP was observed and it was concluded that charge exchange noise dominates. In our case, we believe that charge exchange between graphene and the

interfacial traps also dominates. At high carrier density, short range impurity scattering may dominate as it can screen the underlying coulomb scattering due to trapped impurities at the interface. There, the noise may occur due to the mobile defects inside CVD graphene, which do not change by the application of the gate voltage [1].

Summary

In conclusion, a setup is developed to probe the low frequency noise. We have studied the electronic transport and noise in an electrolyte-gated large area graphene field effect transistor. Density dependence of noise shows a minimum near the charge neutrality point, which is possibly originating due to the charge exchange between the graphene and interfacial traps.

References

1. A. N. Pal, *APL***97**, 1335º4 (2º1º)
2. A. N. Pal, *ACS Nano***3**, 2º75–2º81 (2º11).
3. J. H. Scofield, *Rev. Sci. Instrum.***58**, 985 (1987)
4. I. Heller, *Nano Lett.***1º**,1563–1567(2º1º)
5. Hua-Min Li, *J.Phys.Chem*. C**121**, 16996−17ºº4 (2º17)